UNIVERSITY OF OKLAHOMA

GRADUATE COLLEGE

BREAK UP OF A ROUND LIQUID JET IN A LOW WEBER NUMBER CROSS FLOW

A DISSERTATION

SUBMITTED TO THE GRADUATE FACULTY

in partial fulfillment of the requirements for the

degree of

Doctor of Philosophy

By

OZGUR ALI PULAT
Norman, Oklahoma
2007

Downloaded from SHAREOK. Persistent Handle URL: https://hdl.handle.net/11244/1146

UMI Number: 3243871



UMI Microform 3243871

Copyright 2007 by ProQuest Information and Learning Company.
All rights reserved. This microform edition is protected against
unauthorized copying under Title 17, United States Code.

ProQuest Information and Learning Company
300 North Zeeb Road
P.O. Box 1346
Ann Arbor, MI 48106-1346

©Copyright by OZGUR ALI PULAT 2007
All Rights Reserved.

BREAK UP OF A ROUND LIQUID JET IN
A LOW WEBER NUMBER CROSS FLOW

A DISSERTATION APPROVED FOR THE
SCHOOL OF AEROSPACE AND MECANICAL ENGINEERING

BY

_____
R.N. Parthasarathy (chair)

_____
M.Cengiz Altan

_____
S.R. Gollahalli

_____
Subhash N. Shah

_____
Dimitrios V. Papavassiliou

ACKNOWLEDGEMENTS

I would like to take this opportunity to express my sincerest gratitude to my advisor, Dr. R.N. Parthasarathy for his patience, guidance, and insight throughout this journey. Your assistance throughout this entire process will forever be engrained in my memory. For this reason I will forever be in debt to him. I would also like to thank the GAANN Fellowship, funded by the Department of Education, for the financial support provided.

I would also like to take this opportunity to thank Billy Mays and Greg Williams and everyone else in the AME machine shop that provided so much knowledge and assistance in the fabrication of the testing setup. I would also like to thank Dan Trooline from TSI for his assistance and advice when using the Particle Image Velocimetry system.

Thanks are also in order to the faculty and staff of the University of Oklahoma Aerospace and Mechanical Engineering office. Over these 4 years you have aided me in purchasing of materials, and provided guidance along the way.

Lastly, I would like to express my deepest most heartfelt gratitude to my family and friends for their patience and guidance. My parents, Dr. Simin and Mustafa Pulat, have set the academic bar high in my life and everything I am, I owe to them. I would also like to thank my wife Lindsey Pulat for her patience, love, and compassion over these 4 years. You have guided me through the highs and lows, and I will forever remember it. This dissertation is dedicated to all of you.

TABLE OF CONTENTS

LIST OF TABLES VIII

LIST OF FIGURES IX

LIST OF FIGURES IX

ABSTRACT XII

CHAPTER 1 1
INTRODUCTION 1

1.1 Scope 1

1.2 Background 2

1.2.1 Structure of JICF 2

1.3 Literature Review 5

1.3.1 Nozzle Geometry 5

1.3.2 Single Phase JICF 8

1.3.2 Two Phase JICF 19

1.3.3 Flow Visualization 29

1.3.4 Objectives 33

CHAPTER 2 35
METHODS AND PROCEDURES 35

2.1 Methods 35

2.1.1 Experimental Setup 35

2.1.2 Flow meter 39

2.1.3 Submersible Pump 40

2.1.4 Injector Design 40

2.1.5 Flow System Hardware 41

2.1.6 Particle Image Velocimetry System 42

2.1.7 PIV Background 44

2.1.8 Two Phase JICF Methodology 51

CHAPTER 3 56
COMPUTATIONAL RESULTS 56

3.1 Computational Results 56

CHAPTER 4 65
EXPERIMENTAL RESULTS 65

4.1 Experimental Results 65

4.1.1 Liquid Jet Analysis 65

4.1.2 Stability Analysis 66

4.1.3 Spray Characteristics 77

4.1.4 PIV Cross Sectional Velocity Map 83

4.1.5 Axial PIV Results for JICF 85

4.1.6 Spanwise JICF Results 97

CHAPTER 5 108
CONCLUSIONS AND RECOMMENDATIONS 108

5.1 Conclusions 108

5.2 Recommendations 109

REFERENCES 111

APPENDIX A 117

APPENDIX B 154

NOMENCLATURE 156

LIST OF TABLES

Table 2. 1 Flow system components.....42

Table 2. 2 Select Experimental parameters for two phase JICF.....52

Table 3. 1 Break up locations with varying momentum ratios. 62

Table 4. 2 Adjusted momentum ratio's for re-calibrated free stream velocities. 98

LIST OF FIGURES

Figure 1.1 Single phase JICF structures 3
(courtesty of Blanchard et al. 1999).....3

Figure 2.1 Open circuit wind tunnel 36

Figure 2.2 Water delivery setup.....36

Figure 2.3 Experimental Setup at North Campus 37

Figure 2.4 Wind Tunnel Calibration of test section velocity (m/s) 38

Figure 2.5 Water jet injector design.....41

Figure 2.6 TSI Particle Image Velocimetry setup 43

Figure 2.7 Illustration of a typical PIV arrangement in a wind tunnel 44
(Courtesy of Grant 1997). 44

Figure 2.8 Illustration of the "interrogation" cell for source (a), and image density
(b)45(Courtesy of Grant 1997). 45

Figure 2.9 Double pulsed particle image (courtesy of Dantec Dynamics.com) 46

Figure 2.10 Schematic of the image capture process.....47
(Courtesy of Grant 1997). 47

Figure 2.11 Vector and vorticity contours from PIV measurements 48
(courtesy of Dantec Dynamics.com).....48

Figure 2.12 Transmission spectra for optical filter 55
(courtesy of TSI.com) 55

Figure 3.1. Computational domain for free jet 58

Figure 3.2. Computational domain for 2-d JICF.....58

Figure 3.3. Break up locations of a free jet for various grid sizes. 59

Figure 3.4. Convergence of equivalent diameter with grid size for a 2-d JICF.....60

Figure 3.5. Volume of fluid solution for q=20. 61

Figure 3.6. Volume of fluid solution for q=81.3 63

Figure 4.1 Images of 2mm water jet exit 65

Figure 4.2 Instability frequency as a function of Weber number. 28

Figure 4.3 Illustration of the break up process of a two phase JICF 67
(courtesy of Fuller et al. 1997).....67

Figure 4.4 Visualization of the break up process of a water jet in cross flow: a) q = 172, We = 1.72, Column break up; b) q = 69.25, We = 4.3, Column break up; c) q = 40.7, We = 7.32, Bag break up; d) q = 18.8, We = 15.85, Multimode break up.68

Figure 4.5 Break up process for q = 10, We = 29.29, Multimode break up. 69

Figure 4.6 View of disturbances in the body of the jet in the x-y plane at: a) q = 40.7, We = 7.32, multimode break up; b) q = 18.8, We = 15.85, shear break up; c) q = 10, We = 29.29, shear break up. 75

Figure 4.7 Transient nature of the break off point for q = 40.7 76

Figure 4.8 View of the jet spray for q = 10, We = 29.29. 78

Figure 4.9 View of the jet spray for q = 18.8, We = 15.85. 78

Figure 4.10 View of the jet spray for q = 40.7, We = 7.32. 79

Figure 4.11 Non-dimensional spray width at various downstream locations. 80

Figure 4.12 Display of change in the cross section of the jet at various downstream locations. 82

Figure 4.13 Wind tunnel velocity validation using PIV. 83

Figure 4.14 Wind tunnel velocity in the cross section of the.....84
wind tunnel using PIV. 84

Figure 4.15 PIV measurement plane for all axial locations. 85

Figure 4.16 PIV vector field for q=172 at Y/d=0. 87

Figure 4.17 PIV vector field for q=172 at Y/d=2. 88

Figure 4.18 PIV vector field for q=172 at Y/d=4. 89

Figure 4.19 PIV vector field for q=69 at Y/d=0. 90

Figure 4.20 PIV vector field for q=69 at Y/d=2. 91

Figure 4.21 PIV vector field for q=40 at Y/d=0. 92

Figure 4.22 PIV vector field for q=40 at Y/d=2. 92

Figure 4.23 PIV vector field for q=18.8 at Y/d=0. 93

Figure 4.24 PIV vector field for q=18.8 at Y/d=2. 94

Figure 4.25 PIV vector field for q=10 at Y/d=0. 95

Figure 4.26 PIV vector field for q=10 at Y/d=2. 96

Figure 4.27 PIV vector field for q=77.89 at Z/d=10. 100

Figure 4.28 PIV vector field for q=43.81 at Z/d=10. 102

Figure 4.29 Near field velocity profiles at Z/d=10. 103

Figure 4.30 Proximal velocity profiles at Z/d=10. 105

ABSTRACT

The break up of a liquid jet in cross flow has applications in fuel atomization processes. The break up of a water jet in a high speed cross flow was studied with momentum ratios ranging between 10 and 172. High-speed camera images showed break up characteristics ranging from bag break up (break up due to large ligaments or "bags" of fluid sheared off the liquid jet) to multimode break up (break up in which large ligaments and small drops are present), with large disturbances developing on the jet boundary. The disturbance wavelengths and break up locations were measured and compared, and the agreement was very good. It was also observed that as the cross flow velocity increased, the jet boundary spread linearly outward in the spanwise direction. Particle Image Velocimetry (PIV) results showed that the cross flow did not follow the jet boundary, but passed around the jet, similar to the flow around a bluff body. This implies that the Rayleigh-Taylor instability cannot be a dominant mechanism for the jet break-up. Spanwise PIV results indicate the presence of a high shear region along the sides of the jet, which might serve as the primary cause of jet break-up.

CHAPTER 1
INTRODUCTION

1.1 Scope

The study of Jets in cross flows (JICF) has many different applications. Some of these applications are, but not limited to, liquid rocket engines, diesel engines, air breathing propulsion systems, and agricultural sprays. In some combustion applications, premixed fuel and air is injected upstream of the combustion chamber into a cross flow of air atomizing the mixture. In air breathing propulsion systems such as ramjets and scramjets, the study of a two phase JICF has many applications. For example, a scramjet turbine uses a fuel injected perpendicular to a high speed cross flow to atomize the column of fuel for proper ignition to create thrust. The importance in understanding this interaction lies in efficiently delivering the fuel in its properly "atomized" state for the combustion process.

The most challenging aspect of this research is in the validity of the experimental methods used. The complexity of the two interacting flows: 1) Boundary layer flow (due to no slip along a solid wall), and 2) Free jets makes this topic very difficult to study. When the jet and cross flows are of the same phase, the methodology is somewhat simplified and several options for flow tracking are applicable. However, when the jet and cross flow are in two different phases, the

flow is not easily amenable to conventional methods of measurement. Also, the computation of such flows is cumbersome. The computational time and effort required to model such a complex flow system is far reaching. As a result, few CFD studies of JICF have been undertaken. In addition to the complexities described above very little knowledge exists of the actual process that goes into the atomization of a liquid column by a high speed cross flow. Ideas abound, however little factual evidence has been documented, resulting in an overall "accepted" idea of the reasons behind this break up process.

1.2 Background

1.2.1 Structure of JICF

The study of a JICF is complex due to the interaction of a couple complex fluid phenomena, namely, boundary layer flow and free jets. The cross flow of fluid is usually bounded resulting in a complex boundary layer along the wall which interacts with the jet. Usually wind or water tunnels are used to provide this cross flow and a flush mounted, or elevated circular orifice is used to inject the jet perpendicular to the flowing stream of fluid. Several different arrangements for nozzle geometries have been studied and will be discussed later in this chapter. The inertial force of the cross flow results in a momentum transfer, which bends the jet in the direction of the flowing stream. The depth and penetration of the jet has been

linked to several design factors, such as exit momentum of either fluid, as well as injector designs, which will be described later as well.

A JICF can be single-phase or multiphase. In the single phase JICF, several large-scale structures result in the interaction between the cross flow and the jet. These structures include: Counter-rotating Vortex Pairs (CVP) which originate as an effect of the bending of the jet itself and the shear layer between the cross flow and jet boundary, Horse Shoe Vortices (HSV) which are formed upstream of the jet and close to the wall which act as a carrier of fluid from the upstream side of the jet into the wake of the jet, Wall Vortices (WV) which develop downstream of the jet and near the wall, Upright Vortices (UV) which are formed from the interaction between the wall boundary layer and the jet flow, and are typically unsteady for low jet Reynolds Numbers (figure 1.1).

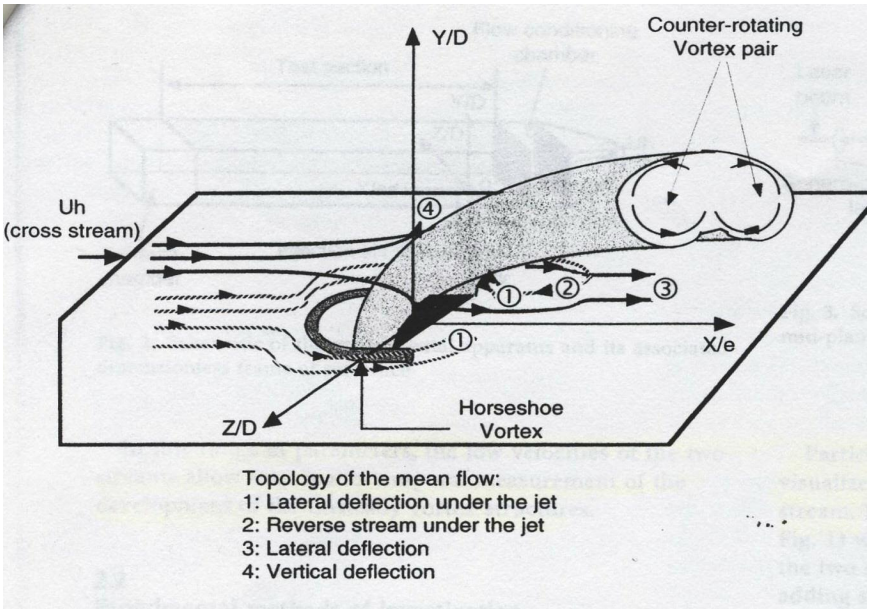


Figure 1.1 Single phase JICF structures
(courtesty of Blanchard et al. 1999)

Also, Ring Like Vortices (RLV) are formed from the jet shear layer; their shape and spatial evolution are influenced by the cross flow. These structures act as the driving force for the mass and momentum transfer.

In the case of the two-phase JICF, the structures that are formed are somewhat different. Less is known of the wake structures for a two phase JICF but several general structures have been observed (Figure 1.2).

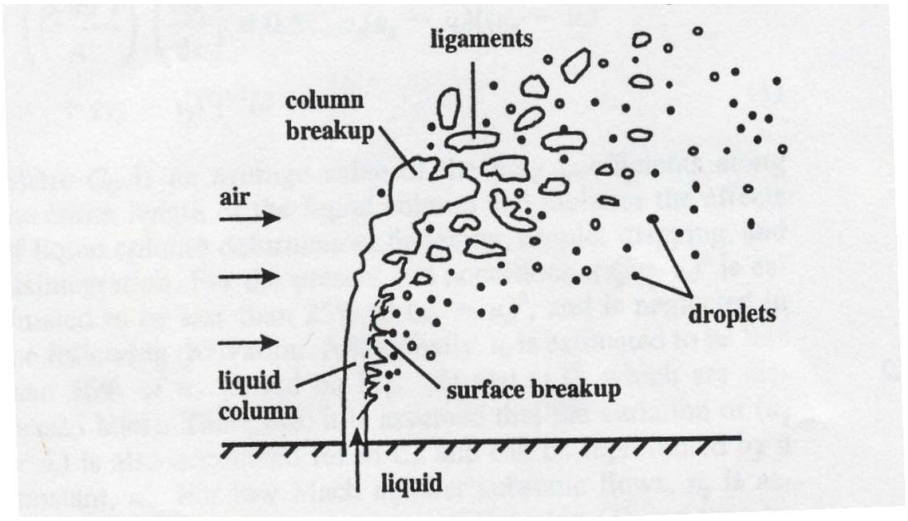


Figure 1.2 Illustration of the break up process of a two phase JICF (courtesy of Fuller et al. 1997)

Initially near the wall, the column of liquid exits much like a cylinder of diameter equal to that of the jet. On the windward side of the jet (upstream), the jet stays fairly steady along its boundary until the presence of waves along the trajectory of the jet is observed, resulting in column break up. There are three main break up types for a two phase JICF, bag break up, multimode break up, and shear break up. For the shear break up regime on the leeward side of the jet (downstream), close to

the wall, surface break up is seen resulting in small droplets spreading and bending in the cross flow direction. For the bag break up regime, at the peak of a single wave on the windward side of the jet, large "ligaments" of liquid break off and form ligaments. These ligaments undergo a secondary break up mechanism due to aerodynamic forces resulting in smaller and smaller droplets. Multimode break up is described by any combination of both shear break up and bag break up characteristics. Very little is known about the wake of the two-phase JICF and how it contributes to the break up of the liquid jet, which is the main focus of this research topic.

1.3 Literature Review

1.3.1 Nozzle Geometry

The main purpose of a two-phase JICF is to aid in the atomization. Various nozzle geometries have been proposed for this purpose. One of these nozzles is an airblast nozzle. Airblast nozzles are typically used for fuel injection processes because of better atomization properties. This type of injector uses a stream of air inside the injector to more efficiently break up the column of liquid surrounding it by cones of air. Carvalho et al. (1998) studied this very arrangement. The air-blast nozzle consisted of a conical shaped nozzle with an annular portion for liquid, surrounded by two air ports. Carvalho et al. (1998) used the influence of the surrounding air shear forces as a means for atomization of the liquid column. The images were processed using shadowgraphy, and a high speed CCD camera with spot lights. The liquid mass flow rate was varied at values of 5.8, 10.8, and 13.9 g/s, with

air Reynolds numbers ranging from 66,000-93,000. In addition, the inner airflow velocities, and swirl level of the outer air was also varied from 40-200 m/s, and swirl rates ≤ 2.5, respectively.

The results showed that as the inner air velocity was increased, the level of atomization was increased, and the break-up length decreased. The authors proposed an inner air threshold of 40 m/s for the proper atomization of the liquid jet. The primary result of interest was that as the swirl level of the jet was increased, the spreading rate of the atomized jet was increased. This paper showed conclusively that shear forces from the surrounding air blast positively affect the atomization of the liquid jet breaking it up into smaller droplets further upstream of the injector. These aerodynamic shear forces act in a very similar manner to secondary drop break up downstream, further accelerating the break up process.

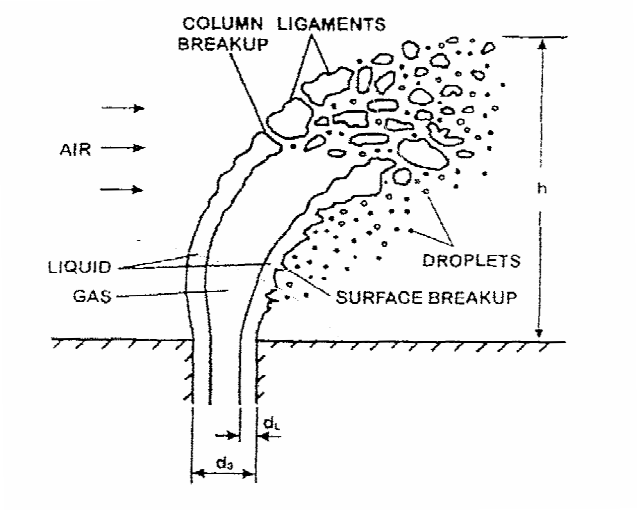


Figure 1.3 Illustration of the break up process of an airblast atomizer (courtesy of Aalburg et al. 2004)

A circular jet exit geometry has been used in most studies. However, some authors have studied other shapes as well as different injection angles, Padhye and Schetz (1977). These influences will be discussed in section 1.3.3. The influence of injection angles is beyond the scope of this study and is discussed in other research papers. Pourdeyhimi and Tafreshi (2003) studied the effect of a conical jet in different positions on a JICF. Results were compared to Ohnesorge classification of high Reynolds number liquid jets, which atomize quickly after discharge. The experiment consisted of a high pressure pump, digital camera, and CCD high speed camera. The flow passed through a cone style nozzle with a capillary section 0.127 mm in diameter and conical section 0.34 mm in diameter. The nozzle configuration was changed by flipping the nozzle for a cone down configuration (water discharges from conical taper), and a cone up configuration (water discharges from straight capillary section). The results showed that the cone up nozzle followed Ohnesorge classification, while the cone down configuration did not. At a Reynolds number of 18,600, a first wind-induced break up mode was observed, while according to Ohnesorge theory this should not occur at Reynolds numbers above 8,600. Pourdeyhimi and Tafreshi (2003) stated that due to the cone down geometrical configuration the flow separated from the nozzle wall and resulted in a recirculation zone, which resulted in the elimination of wall friction vortices inside the injector that would normally influence the break up mechanism of the jet. It was concluded that a constricted (cone down) water jet did not follow the classifications of Ohnesorge. This paper showed that the geometry of the nozzle has an affect on the break up of

the liquid jet, and should be taken into consideration when studying the break up of a liquid jet in a cross flow.

1.3.2 Single Phase JICF

The study of single phase JICF has many environmental applications, such as pollution control of smoke stacks into atmospheric cross flows, or injection of pollutants into flowing streams. The early studies of single-phase JICF centered around the penetration and mixing properties of the interaction between an air jet, and an air cross flow. One such study was Baines and Keffer (1962). Using an air jet, and air cross flow, the penetration at velocity ratios ($R=U_j/U_\infty$) of 2-10 was studied. The cross flow of air was generated by a low speed wind tunnel with a 4 ft x 8 ft cross section. The air jet issued perpendicular to the cross flow from a 3/8" diameter orifice. Hot wire anemometers were used at various locations to map out the velocity profiles in the jet. The results showed that the penetration of the jet into the cross flow decreased as the velocity ratio decreased. The entrainment into the jet was shown to increase as the velocity ratio decreased.

Hester et al. (1971) studied the presence of shed vortices in the wake of a single phase JICF. Hester et al. (1971) utilized a subsonic wind tunnel with a constant freestream velocity of 50 ft/s. Velocity ratios of 8 and 12 were studied, by varying the exit velocity of an air jet through a 2" diameter pipe. Flow visualization was achieved by placing a tuft screen in the wake of the jet. The tuft screen consisted of a wire mesh with bits of thread taped to the screen. The effect of the flow on the

tufts was recorded using a high-speed movie camera (240 frames/sec). The results indicated the presence of periodic eddies in the wake of the jet. The high-speed camera images allowed the determination of the vortex-shedding frequency, which was quantified using the Strouhal number (St):

$$St = \frac{fd}{U_\infty} \qquad \text{(eq 1)}$$

Where, f is the frequency, d is the diameter of the column of liquid, and U_∞ is the cross flow velocity. The measurements indicated that the Strouhal number was less than one-half of the Strouhal number associated with the shedding of vortices behind a solid cylinder of comparable dimension. The authors also stated that the vortices in the wake of the jet appeared to travel in the downstream direction along the plate, surrounding the jet, instead of along the axis of the jet. This study was important in showing the connection between the shedding vortices from a solid cylinder, and shed vortices in a single phase JICF, which is generally only present in a range of Reynolds numbers, $250 < Re < 2x10^5$.

Chassaing et al. (1974) continued the work of Baines and Keffer (1962) by focusing on the trajectory of the jet, and defining planes of symmetry within the body of the jet. Using experimental measurements with pitot probes and hot wire anemometers, Chassing et al. (1974) were able to develop a new method for evaluating the axis of the jet. Fearn and Weston (1974) shifted the focus of the study of a single phase JICF from trajectory to the influence of the Counter-rotating Vortex

Pair (CVP). The experimental investigation utilized a V/STOL wind tunnel with cross flow velocities ranging from 100-175 ft/s, and a 4" diameter air jet with velocity ratios ranging from 3-10. Velocity measurements were made using a rake of ¼" pitot static probes attached to an airfoil at 2-45 jet diameters downstream. The results indicated that the CVP was generated very close to the exit of the jet with strength directly proportional to the speed of the jet at the orifice as well as the diameter of the jet. The vorticity strength of the CVP was also shown to weaken as the vortex pair traveled downstream, because of the diffusion of vorticity.

Eskinazi et al. (1976) set out to experimentally document the exit conditions of the flow at the jet exit and to prove the three-dimensional nature of the interaction between an air jet and an air cross flow. The motivation behind the study was to use the results to provide some insight into the validity of the computational studies of a single phase JICF, which were just beginning at the time. Eskinazi et al. (1976) utilized a 2.39 cm jet in a wind tunnel providing a 29.6 m/s cross flow, with a jet Reynolds number of 4.4×10^4. The velocity was measured using a constant-temperature anemometer at 1,000 separate points, 1 diameter upstream and downstream of the jet center. Both skirted and unskirted pipes were used to study the differences between a "hole in a wall" JICF (skirted) and a "pipe exit" JICF (unskirted). The results indicated that the shedding frequency of vortices from a single pipe with no skirting at $R < 5.5$ was very close to that of a solid cylinder, where "R" is the ratio of the cross flow velocity to the jet velocity. The researchers were one of the first to show experimentally that a single pipe in cross flow was

influenced by the vortices shed off the pipe itself, which was shown to be quite different from the structure of a skirted JICF. The results further highlighted the strong connection between the vorticity generated within the pipe and the CVP vorticity in the jet body. Eskinazi et al. (1976) also mapped out a new way of defining the jet boundary as a function of not only the paths of the center of the jet, but also the locations of maximum vorticity in the CVP.

Andreopoulos (1985) conducted another early study of a single-phase JICF with the intention of studying the interaction of a boundary layer channel flow and the boundary-layer pipe flow. The experimental setup consisted of a 50mm pipe, 12 diameters in length. The cross flow developed a boundary layer 4 diameters upstream of the jet at a free stream velocity of 13.9 m/s. Mean and fluctuating velocity measurements were made with a DISA X-wire probe. The flow was visualized using a fog of paraffin oil droplets, and the images were captured by a NIKON camera. A conditioning technique was used to track the jet and cross flow separately by heating one and using a thermal anemometer to discern between the two flows. For this experiment, the jet was heated using heating elements along the pipe length. For R values greater than 3, and jet Reynolds numbers less than $5x10^3$, ring vortices were formed at the top of the jet. These ring vortices were of opposite vorticity to that of the cross flow, but similar to that of the pipe flow. The ring vortices underwent bending and stretching, as they are convected downstream and were finally broken down to turbulence. As the value of R was decreased, the ring vortices were visually less organized and more randomly generated in their occurrence. At higher Reynolds

numbers, the generation of these large-scale structures from the jet decreased and the size began to fluctuate.

Up to this point, much of the research on a single phase JICF had been focused on the large-scale structures in the flow. It had always been assumed that as the free stream passed around the body of the jet, the flow behaved similar to the flow passing over a solid cylinder. Fric and Roshko (1994) were the first to question this assumption. Fric and Roshko (1994) studied the near-wake of the JICF and set out to prove that the wake that formed due to the interaction of a boundary layer flow and a jet was not similar to the wake which forms due to the flow around a cylinder. It had been assumed that the vortices seen in the wake of the JICF were due to vortex-shedding from the jet, similar to the flow around a solid cylinder.

The air jet velocity was varied from 3 to 45 m/s and the value of R value was varied between 2 and 10. The flow visualization was achieved using a smoke-wire arrangement in different planes and at different locations. By placing the smoke wires at different distances from the wall, the boundary layer flow as well as the flow outside of the boundary layer was visualized. For velocity measurements, a single hot wire probe was used with a XYZ traversing mechanism for placement.

Cross-sectional slices of the flow around a JICF at different locations in the Z direction were documented. Most notable was the formation of the horseshoe-vortex at the upstream exit of the jet, which acted to carry fluid from the upstream side of the jet into the wake of the jet. At the rear of the jet, various wake structures were observed. The most noticeable and organized structures are seen at a momentum

ratio of 4. Contrary to the flow around a solid cylinder which experiences a very "open" separation at the rear of the cylinder, the wake around the jet was closed. The separation region is defined as the location where the streamlines separate from the boundary along the sides and the immediate rear section of the boundary resulting in a "dead zone" of fluid which typically consists of a pair of bound vortices. The separation of flow around a solid cylinder was shown to result in a very large separation region, whereas the separation region for the JICF was much smaller in size adhering more closely to the boundary of the liquid jet. A comparison of the two flows showed noticeable differences in their geometry. Through the use of smoke injection within the jet, it was also observed that the wake vortices were not shed from the jet body. By injecting smoke into the boundary layer, it was seen that the wake vortices were entrained upward into the jet itself. Initially, the wake folded up under itself at a "separation event" due to the adverse pressure gradient imposed by the flow outside of the boundary layer (external flow). This folding resulted in vortices primarily in the Y direction. The wake vortices were then tilted and bent upward into the bottom side of the jet. For lower R values (R = 4), the formation of these wake vortices was well defined and the side views showed the presence of large tornado-like vortices. For other values of R, the tornado vortices were less defined. This research showed that the wake vortices did contribute to the mixing and entrainment of the cross stream into the body of the jet. The wake entrainment drew surrounding fluid into the CVP, resulting in the mixing of the two streams.

The stability of the CVP was studied by Kelso et. al (1996). In this paper, a study of a round jet in cross-flow was analyzed at Reynolds numbers ranging from 440 to 6200, and velocity ratios ranging from 2.0 to 6.0. The study was conducted in a water channel with liquid-liquid cross-flow jet interaction. Flow visualization was achieved with the introduction of a dye upstream of the jet exit as well as from circumferential slits around the sides of the jet as well as on the downstream side. Further experimentation was done for a gas in gas cross-flow along with the measurement of pressure gradients and smoke streams to validate any assumptions made by the liquid in liquid case.

The main results indicated that the jet contained many complex vortical systems. Dye injection showed that on the upstream side of the jet, some of the cross-flow was actually entrained into the jet due to adverse pressure gradients formed within the jet pipe. The CVP was observed at various Reynolds numbers and was attributed partially to the separation pattern within the upstream side of the pipe. Ring vortices were also observed due to Kelvin-Helmholtz instabilities. These rings in the jet shear layer were tilted and appeared to fold and contribute to the CVP. On the back side of the jet, wall vortices appeared due to the wake from the jet. At low Reynolds numbers (440), these wall vortices were less apparent, but still entrained fluid from the wall into the CVP. At higher Reynolds numbers (2700), a von-Karman vortex street was readily observed. At these high Reynolds number values, the wall vortices were advected upward into the jet causing upright vortices contributing to the

CVP; the non-dimensionalized phase-averaged vorticity contours showed a peak vorticity in the wake of the jet with a value of 11.26 ($\omega_{nd}=\omega D/U_{\infty}$).

Blanchard et al. (1999) also studied the influence of the CVP on the stability of a jet in cross flow. The generation of the CVP was said to be due to the interaction of the cross flow moving around the body of the jet folding the jet in upon itself. Other large-scale structures observed were the street of transverse vortices (ring vortices) as well as vertical wake vortices (wall vortices). All three of these structures were unsteady in nature. The experimental setup consisted of a square test section water channel with a water slot jet (2cm * 0.2 cm) under hydrodynamic isothermal conditions. The values of R were varied from 1.5-6.5, also, the Reynolds numbers ranged from 100-600. The main objective of this study was to measure the spatial and temporal characteristics and the development of the unsteady vortex structures for a JICF at low velocities. This was achieved by the use of two methods of measurement, Laser Induced Fluorescence Tomography (LIFT), and Particle Streak Velocimetry (PSV). For the LIFT technique, a fluoresceine salt was dissolved in the water and excited by a laser light sheet from an argon ion laser. The reflected green light was used to resolve only the jet fluid flow.

PSV was used in this study to visualize the surrounding stream due to the cross flow of water. PSV uses small solid particles in the flow and records their paths in different cross sectional planes of light provided by an argon-ion laser centered on wavelengths of 488 and 514 nm. Using optics similar to that of the LIFT method, the motion of the fluid particles was tracked. This method was used to formulate

topological data (size of the CVP). The results using LIFT showed the entrainment of the cross-flow fluid into the body of the CVP. The authors indicated that this proved that the CVP served as the primary mixing structure in the JICF. Using PSV methods, the evolution of the CVP was tracked. The authors showed that the CVP grew in both the Y and Z directions, where Y is the distance from the injector, and Z is the spanwise distance or "width" from the injector. The CVP grew until the size was nearly equal to the breadth of the entire channel, whereby they finally became stable in size. Throughout the growth of the CVP, the authors indicated that there was no significant difference in size between the left and right vortices. At the region of stability (X/e =20) the size of the CVP in the y direction and the z direction were dissimilar, where "e" is the thickness of the injection slit. Using this data, the authors indicated that the CVP was most nearly elliptical in shape.

Next the location of the instability was studied. A jet with a Re = 300 and R = 3 was steady and stable in its structure. At a value of Re = 500 and R = 4.5, the jet became unsteady and the ring vortices were formed due to the unsteadiness. The authors went on to show that the common belief that these vortices were a result of Kelvin-Helmholtz instabilities was incorrect. Through the use of a histogram and calculation of the min and max wavelengths, it was shown that the instability was not characteristic of "Kelvin-Helmholtz" instabilities, but characterized generally by the Landman and Saffman theory of instability. Kelvin-Helmholtz instability arises when a mixing layer is present between two fluids. Amplifications of small local disturbances in this shear flow lead to the unstable nature of the flow. Landman and

Saffman theory of instability focuses on the highly unstable nature of the elliptical shape of the CVP. Comparisons between the Landman and Saffman theoretical rate of thickening and experimental measurements showed good agreement, leading the authors to characterize the instability of the CVP as Landman and Saffman instability. These findings were later validated by Ferre et al. (2001), and Camussi et al. (2002).

Ferziger et al. (1999) used Large Eddy Simulation (LES) to study a single phase JICF. The program used the incompressible, unsteady Navier-Stokes equations to model the complex flow. Simulations were performed for values of R of 2 and 3.3, and Reynolds numbers of 1050 and 2100. A total of 1.34×10^6 control volumes were used in a domain that spanned 13.7d x 8.0d x 9.0d. The simulations were compared with experimental results and the two sets of results were found to be very similar. Any differences were attributed to the difference in jet inflow conditions, as well as Reynolds number discrepancies resulting in differing boundary layer configurations at the lower wall. Four main structures were observed in the near wake of the jet: hanging vortices, ring vortices, wall vortices, and CVP. The hanging vortices were observed to originate at the lateral side of the jet, and are seen as an extension of the horseshoe vortex. These hanging vortices transported flow to the rear of the jet originating from the near wall of the pipe and the upstream cross-flow boundary layer. Breakdown of these vortices occurred due to adverse pressure gradients experienced as the flow passes around the jet (similar to flow around a bluff body) and compressive stresses due to upsweeping motion of the cross flow fluid into the jet body.

Span-wise rollers were formed due to K-H instabilities on the upstream and downstream side of the jet. The span-wise rollers were found to carry high amounts of velocity fluctuation in the near field of the jet resulting in high turbulent kinetic energy (TKE). In the wake of the jet stream-wise vortices were observed as well as vertical or upright vortices. The formation of the upright vortices was shown to be due to the reorientation of the stream-wise vortices due to the strain field behind the jet. The phase-averaged vorticity contours in the wake showed a peak value of 0.4 ($\omega_{nd}=\omega D/U_{\infty}$). All three structures were shown to contribute to the evolution of the CVP.

A number of studies have involved reacting jets in cross flows. Chang and Huang (1994) studied the stability of an elevated combusting jet in cross flow. Using a high-speed wind tunnel and a propane jet, the structures in the wake of an elevated jet in cross flow were studied. Images were compiled using a Schlieren technique in the wake of the jet. The results showed the presence of organized vortices in the wake of the elevated jet. The vortices were shown to directly affect the stability of the flame in cross flow resulting in a "flickering" flame.

In a similar paper by Huang and Yang (1996), the temperature profiles and concentration in the wake of a combusting jet were measured. The results also showed the dependence of concentration profiles in the wake of the jet on the mixing structures in the wake of the jet. Gollahalli and Pardiwalla (2002) studied the characteristics of a turbulent reacting jet in cross flow. Using a wind tunnel with a thermocouple and gas sampler, the temperature and concentration of products in the

wake of the jet were studied. Results showed the dependence of the flame configuration on the presence of bound vortices in the wake of the jet. Similar to the findings of Chang and Huang (1994), the two-zone structure was shown to "flicker" due to the presence of vortices in the wake of the jet. Most importantly, results showed that larger wakes downstream of the jet resulted in increased soot production in the wake of the jet.

1.3.2 Two Phase JICF

Much of the study of two phase jets in cross flows focuses on the break up process of the jet itself. One of the first studies to analyze jet penetration and break up in a subsonic cross flow along with different nozzle geometries was by Padhye and Schetz (1977). A 9" by 9" blow down wind tunnel was used with a flat plate and flush mounted water injector. Injectors of different sizes were used along with different orientations to the free stream. Photographs were taken using a long-exposure camera, and a short-exposure camera, both cases used a back light to view the image. Measurements were made downstream at an x/d location of 6.25 from the center of the injector. A non-dimensional momentum ratio "q" was used to relate the exit momentum of the jet (j) to the cross flow momentum (∞)

$$q = \frac{\rho_j U_j^2}{\rho_\infty U_\infty^2} \qquad \text{(eq. 2)}$$

The results showed that penetration (axial distance into the cross flow) decreased with an increase in the cross stream Mach number. This was said to be due to the increased drag coefficient due to the flow over the bluff body. Droplet size was shown to decrease with increased free stream Mach number. The orientation of the rectangular injector aligned with the free stream resulted in a reduced mean droplet diameter, while the transverse orientation resulted in an increase in the mean droplet diameter. The study also showed that an increase in the flux q resulted in an increase in the axial distance to the jet fracture, and a decrease in the amplitude and wavelength of the surface waves. The axial distance to gross fracture was greatest for the aligned rectangular slot jet.

Along with this study, Less and Schetz (1986) studied that transient behavior of the JICF. The objectives of the study were to "quantitatively characterize the time dependent behavior of a liquid jet in gas cross flow." The authors described the interaction of the liquid jet with the gaseous cross flow as an initial formation of a liquid column, followed by axial waves that developed along the surface of the jet, and propagated till the jet fractured at the trough of a high-amplitude wave. The experimental apparatus consisted of a high velocity wind tunnel with a flush mounted jet, 0.91mm in diameter. A high-speed camera with a CCD detector was used to measure the diffraction patterns of the light column passing through the spray plume. The designed system allowed for droplet measurements ranging from 7 to 100 micrometers in diameter.

The results indicated that at every location, the droplet size varied greatly as a function of time. The measured frequency of the axial waves was 60 kHz, with a fracture point frequency of 15 kHz. The authors also indicated that initially the waves propagated at velocities equal to that of the jet, then were accelerated further downstream at velocities nearing that of the free stream. The frequency of instability was expressed in the form of the Strouhal number, which turned out to be constant at 0.4.

The authors made a comparison between this Strouhal number and that for the flow around a solid cylinder, 0.2, noting that there was a distinct similarity between the two flows. The authors also stated that there was a strong interaction between the mechanics of the gas flow, shed vortices, and the instability in the column of the liquid jet. This was the first study of its time to question the role of the wake and its influence on the break up of the liquid column.

Following this study, Fuller et al. (1997) studied the near-field of the two-phase JICF, along with the influence of differing fluid types. Much of the experimental setup was similar to the previous study. The four fluids used were water, ethyl alcohol, 30% alcohol/water, and 40% glycerol/water. The results showed that the primary break up of a liquid jet was a result of aerodynamic factors. The liquid column was initially deformed, then flattened and broken up by the cross flow. The interaction between the two flows was shown to be a variable of the Weber number (We).

$$We = \frac{\rho_\infty d u_\infty^2}{\sigma} \qquad \text{(eq 3)}$$

Where ρ_∞ is the density of the cross flow (1.21 kg/m^3), u_∞ is the cross flow velocity, and σ is the surface tension of the jet fluid. The study found that at lower Weber numbers the liquid column exhibited "bag break up", whereas at higher Weber numbers the primary break up was due to waves in the column due to shearing forces. For higher viscosity fluids the waves were more prominent, along the upstream side of the jet. When the momentum flux ratio was large, the jet underwent a surface break up mechanism, in which the rear side of the jet broke into smaller droplets. Using an aerodynamic analysis on a single droplet, several equations were derived to predict column trajectories, and break up locations for a liquid jet in cross flow. The theoretical results were in good agreement with the experimental measurements, thus indicating that the primary break up mode of a liquid jet was due to the aerodynamic forces on the liquid column. The analysis also showed that the drag coefficient for a liquid jet in cross flow was similar to that of a cylinder of comparable size, and increased for higher viscosity fluids, contrary to the findings of Fric and Roshko (1994) for a single phase JICF. The y-location of break up indicated a high dependence on the momentum flux, while the x-location was constant for all momentum flux values.

Fuller et al. (1998) went on to study the primary structures in a two-phase JICF. The experiment consisted of a water jet injected through a 0.5 mm hole at velocities ranging from 12.8 to 42.5 m/s. The cross flow of air at Mach 0.3, 0.4, and

0.5 was delivered in a high-speed wind tunnel. Through a clear side panel, Phase Doppler Particle Analyzer (PDPA) measurements with a 10-mW helium-neon laser were made at X/d = 300, 400, and 500. The results showed that as the momentum flux increased, the maximum volume flux of water passing through the measurement plane decreased. Also, the Sauter Mean Diameter (SMD) decreased, as the cross flow velocity increased, due to increased secondary droplet break up downstream of the jet. The authors showed that large droplets were distributed towards the top of the spray plume when q was large, but for small q the large droplets were found in the central portion of the spray plume. The difference was said to be due to the intense momentum exchange between the two fluids resulting in obvious wake regions for most cases. The importance of the presence of a wake may shed light into the fact that wake structures could play a part in the atomization of the liquid column. The wake was most evident at an X/d value of 200 for 0.3 Mach air flow. Also, at X/d of 300, U_j =12.8 m/s, and q = 9.5 a relatively strong wake presence was noted. The structure of the wake was evident through the high velocity of the droplets at the sides of the spray plume. Fuller et al. (1998) stated that this was most likely due to the shearing action of the cross flow resulting in a high momentum exchange thereby accelerating the droplets in the cross flow direction.

A study by Azzopardi et al. (2003) later contradicted the bag break up findings of Fuller et al. (1998). The authors found that at higher cross flow Weber numbers the bag break-up mode was dominant while at lower Weber numbers column break-up prevailed. A comparison with lower viscosity fluids showed little to

no difference in the break-up modes for each flow regime. The authors stated that this implied that the fluid viscosity did not influence the break-up mode of a liquid jet in cross flow, contrary to the findings of Fuller et al. (1998). However, at liquid viscosities higher than water, the penetration in the transverse and stream direction was influenced by both the viscosity and the momentum flux ratio. At lower liquid viscosities, this trend was not observed.

Madabhushi (2003) used a computational algorithm to analyze a two-phase JICF and validate many of the findings of Fuller et al. (1998) for the presence of a wake. The results were validated by comparison of measurements made by a PDPA system. The cross flow was simulated by using the Reynolds averaged Navier-stokes equations, with pressure correction and a standard, k-ε turbulence model. The droplet motion was modeled using a Lagrangian approach. The test conditions consisted of a 0.5 mm injector with water injection velocities of 12.8 to 42.5 m/s. The cross flow velocities were varied at values of 68.7, 103, and 137 m/s. These values resulted in momentum flux ratios ranging from 9.5 to 48.8. All measurements experimentally and computationally were made 300 diameters downstream. The results showed a generally good comparison between the CFD results and the PDPA measurements. Near-wall values of droplet velocity and size from the CFD results were higher than measured values. This was said to be due to the presence of a wake, which was not modeled in the CFD. The study of the SMD showed the presence of smaller sized droplets near the wall, said to be due to the "stripping" of droplets from the jet surface due to the wake. At q = 9.5, this occurred at a height of Y/d=20. Stream-wise

velocity contours showed a high velocity region at the outer portion of the jet due to the flow wrapping around the jet body and accelerating the stream-wise flow. These measurements agreed with the findings of Fuller et al. (1997), showing the presence of a wake.

Aalburg et al. (2004) also studied experimentally and computationally a two-phase JICF. This study computationally assumed that initially the jet column acted as an upright cylinder. The validity of the assumption remains to be seen; however, the results showed that eddy shedding in the wake of the cylinder was onset at a Reynolds number of 40. Plotting the eddy shedding frequency in a graph of Strouhal number versus the Reynolds number yielded very good agreement between the computational results and experimental results. The JICF experimental results showed that the liquid/gas density ratio had a small effect on the deformation and break up of the jet at density ratios less than 30 and small Oh numbers. The Reynolds number was also found to have a small effect on the deformation of the jet. For Reynolds numbers approaching Stokes flow, the jet deformation was relatively small due to increased drag coefficients. Conversely, the authors stated that this drag could also contribute to increased jet break up.

As an extension of the previous study Aalburg et al. (2004) went on to show, experimentally, that the transition points for the break up of a liquid jet under, bag, multimode, and shear break up were onset at critical Weber numbers of 4, 30, and 110, respectively. The authors stated that the primary mechanism leading to the break up of a round nonturbulent liquid jet, were classical Raleigh Taylor instabilities

resulting from the acceleration of a fluid of greater density toward a fluid of lesser density. Deformations of the liquid column were also attributed to pressure imbalances due to the accelerated cross flow fluid moving around the body of the jet.

Aalburg et al. (2005) performed a study detailing the properties of surface waves seen in a two phase JICF using computational methods. The study used FLUENT's VOF model with jet diameters ranging from 0.5-2 mm and momentum ratios of 3-8,000. The primary findings showed that the computational results were in good agreement with experimental measurements of measured disturbance wavelengths and break up locations. Aalburg et al. (2005) also formulated a relationship between the Weber number (We), jet diameter, and disturbance of the wavelength along the upstream side of the jet (λ_s).

$$\frac{\lambda_s}{d} = 3.4 \cdot We^{-.045}, \qquad \text{We} > 4 \qquad \text{(eq 4)}$$

Where d is the exit diameter of the liquid column, and the Weber number (We) is the ratio of inertial forces to surface tension forces (eq. 3). The research also showed that as the Weber number increased, the wavelength and amplitude decreased, similar to the observations of Less and Schetz (1986).

The wavelengths and frequencies of the disturbances on the upwind side of the jet have been well documented by researchers such as Less and Schetz (1986), and Aalburg et al. (2004 & 2005). Both research groups showed that as the momentum ratio, q, increased, these wavelengths decreased in size. Aalburg et al.

(2004 &2005) formulated a correlation between the wavelengths and the Weber number (eq. 4), while Less and Schetz (1986) used the Strouhal number to relate the frequency of instability to the cross flow velocity and column diameter (eq 1). In order to specify the frequency of the disturbances measured by Aalburg et al. (2004 &2005), the wavelength velocity must be known. For comparison purposes, the wavelengths of Aalburg et al. were used with the findings that the waves propagate at a velocity equal to that of the jet. Much like the fluid velocity, the wave velocity near the injector should travel very close to the exit velocity of the liquid, and as aerodynamic forces due to the cross flow build, the fluid is accelerated in the downstream direction.

Taking into account these two assumptions, two frequencies of instability were calculated. Comparing these results to the Von Karman frequency of shedding from a solid cylinder, a relationship was formulated between the frequency of instability and the Weber number.

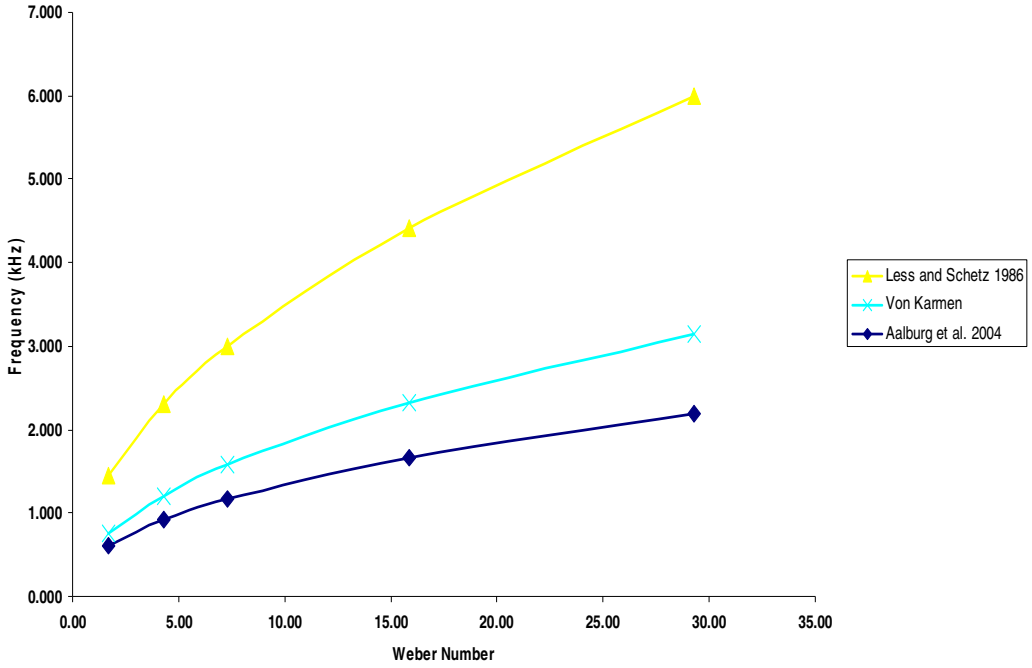


Figure 1.4 Instability frequency as a function of Weber number.

Figure 1.4 shows that the relationship of Less and Schetz (1986) is closely correlated to the vortex-shedding frequency, while the relationship of Aalburg et al. (2004) is closer. The importance of these findings shows that there is some correlation between the instability measured in the jet, and the instability from a pair of shedding vortices off a circular cylinder in cross flow. Much is still not known about the break up mechanisms of a two phase JICF, but many theories were proposed. Less and Schetz (1986) showed that there was a distinct connection between the shedding of vortices from a solid cylinder and the frequency of the waves on the upstream side of the jet. Taking this into consideration they felt that the break

up mechanism was very closely related to any disturbances in the wake. Aalburg et al. (2004) proposed that, similar to secondary droplet break up, the break up mechanism of a two phase JICF was more than likely related to a Rayleigh-Taylor break up mechanism, where the shearing of two differing density fluids generates the surface waves on the upstream side of the jet. The break up mechanism for a two phase JICF is still a matter of much debate as it stands currently.

1.3.3 Flow Visualization

The current study will focus mainly on the influence of the wake, for a two phase JICF, on the break up of the liquid column. Previous studies by Fuller et al. (1997) and Madabhushi (2003) have shown the presence of a wake for this arrangement. Outside of the findings of Fric and Roshko (1994) for a single phase JICF, no visualization of any wake structures has been made for a two-phase JICF. The study of these wake structures is important because of their influence on the instability of the JICF as mentioned by Less and Schetz (1986). The complexity in visualizing the wake structures lies in the tracking of the two phases.

Bartelheimer et al. (2000) studied the velocity field of a two-phase flow without any particle seeding at all. For this experiment, the authors used a Bosch automobile spray nozzle to inject water into ambient air. Seeding particles were replaced by NO (Nitric Oxide) gas which was used as a tracer injected through a valve very close to atmospheric pressure preventing any influence in the flow field. Using the same lasers and CCD camera, two images were recorded with a 150 μs

delay. The small delay was said to be necessary to prevent any molecular diffusion of the gaseous tracer. With a very small delay time, the tracer accurately followed the flow field. The ICV method was used to post process the signals. An optical filter was used to remove any Mie-scattered images from the water spray. It was noted by the authors that for more dense sprays, the filter should be improved. The authors used signal suppression for LIF signals less than 15% of the average LIF signal. This suppression helped to reduce the shot noise in the measurements. To validate the results, the second image of each pair was simulated numerically and compared to the actual second image. The results showed a very good comparison with an average error in the velocity of 3.1%. Other validation tests indicated that the accuracy was dependent upon the spatial resolution. Further tests showed that if the spatial resolution was improved then the error in the measurements increased. Smoothing techniques were also shown to have little effect on the accuracy of the measurements. The molecular diffusion error was also studied and showed little significance in the present study. Further errors were said to be due to out of plane motion by the NO tracer.

Bartelheimer et al. (2000) wrote a similar paper where they studied the velocity field measurements in a two phase water aerosol embedded vortex generator. The specific objective was to compare and contrast PIV and gas phase velocimetry (based on LIF). The PIV system for this experiment uses a double pulsed Nd:YAG laser with a CCD camera. The seeded particles were distributed using an aerosol generator and water. For the gas phase velocimetry technique, the flow was seeded

with NO to act as the tracer gas. Two KrF excimer lasers were used with a CCD camera to track the flow. Both measurements system were pulsed at different intervals to eliminate any interference between the two lasers. The delay of each pulsed laser was .1 ms, thereby making each measurement relatively instantaneous. For the PIV system, a common cross-correlation technique was used to resolve the data. For the gas phase velocimetry technique, the Instantaneous Correlation Velocimetry (ICV) method was used. By dividing the interrogation volume into "spots" and using a mapping function, based on the intensity of scattered light, the velocity and direction of each particle was determined. The flow field studied was very two-dimensional, so any movement out of the interrogation field was neglected.

The results showed that some differences did exist in the two methods for instantaneous measurements. Primarily, the use of water droplets for PIV yielded a "lag" in the data due to the inertia of each droplet. This "lag" was prevalent in areas where a steep change in velocity direction occurred. The deviation due to this 'lag" was at most 3.6%. However, the authors determined that the total average error between the liquid and gas phase was 8% indicating the presence of another error. The authors attributed the other source of error to primarily "shot noise."

Boedec and Simoens (2001) also made velocity field measurements for two-phase spray flows. The main focus was on the development of an experimental method for the measurement of both the gas and fluid phase velocities of a high-pressure spray. One of the main issues with simultaneous measurement devices is the discrimination between the signals from water droplets in the jet and the signals from

particles in the seeded gas. Post-processing techniques, such as autocorrelation, have been known to cause problems for simultaneous measurement systems such as this. To remedy this, the velocity fields of both phases were processed using a cross-correlation technique. The experimental setup consisted of a high pressure spray issuing into an open air vessel with four clear windows at 0, 90, 180, and 270 degrees. Two Nd:YAG lasers were used to illuminate a fluorescent dye for the liquid phase, and smoke particles for the gas phase. Incense particles were used because they avoid any coalescence with the atomized liquid phase. The images were recorded using two CCD cameras. One camera was fitted with a band-pass filter to read only the water droplets of the liquid phase. The other camera was used to image both Mie-scattered diffusion, and LIF light (droplets and solid particles). After digital image processing, binary operations, the images were able to discern between both gas and liquid phases. The results showed that liquid-phase comparisons with LDV measurements showed a very good comparison with a global error of 5% for mean values, and a global RMS error near 30%. The importance of this paper is in the development of the methodology for simultaneous measurement of liquid and gas phase velocities. Cessou et al. (2005) used fluoresceine particles and the proper optical filters to simultaneously measure the velocity field of both the gas and liquid phase of an axial co-flow. Using a Nd-YAG laser at wavelengths of 532, and 355 nm, two CCD cameras fitted with optical filters, each phase was tracked independently of the other. Initially a spectral study was conducted to pair the proper fluoresceine powder with optical filter for each emitted wavelength of light. At 532

nm, the authors chose Rhodamine 610 for the gas phase and LD88 for the liquid phase with the appropriate band pass optical filters. At 355 nm, Stilbene 420 was chosen for the gas phase and Coumarin 450 for the liquid phase. The authors chose to use the 355nm wavelength because of the larger spectral range, but both wavelengths showed to be accurate. The use of fluoresceine particles for flow tagging and optical filters allowed the authors to probe both phase velocities simultaneously and opens many doors in making measurements in multiphase flows.

1.3.4 Objectives

Previous research in two-phase JICF indicates the presence of disturbances on the upstream side of the liquid jet leading to jet break up. The origin of these disturbances remains a point of debate. Some researchers have argued that the instability was a classic case of Rayleigh-Taylor instabilities (Aalburg et al. 2004), while others allude to the influence of shedding vortices in the wake, which contribute to the unsteady nature of the jet (Less and Schetz 1986). It is the aim of this study to shed some light on the validity of these two theories. The specific objectives of this research topic for a two phase JICF are to: i) Develop a methodology to track the gas cross flow and observe how it interacts with the liquid jet ii) Document and measure the characteristics of the instabilities in the jet column iii) Provide new insight on the source of the instabilities and the break up mechanism of a two phase jet in cross flow.

In this chapter, a detailed background was provided along with a structural understanding of a JICF. In chapter 2, a detailed summary of the methods and procedures used to successfully achieve the objectives are stated. In chapter 3, the computational results of the experiment will be covered in full detail with explanation of all findings. In chapter 4, the experimental results of the experiment will be discussed. In chapter 5, a summary of the entire study will be given with conclusions and recommendations.

CHAPTER 2
METHODS AND PROCEDURES

2.1 Methods

In this section, a full description of the methods used to fulfill the objectives stated will be given. Detailed schematics of the experimental setup and experimental components will also be included. Due to the complexity of visualizing the wake in a two phase JICF, a detailed explanation of physics behind the method, Particle Image Velocimetry (PIV), will also be included.

2.1.1 Experimental Setup

In order to visualize the wake created through the interaction of a water jet issuing perpendicularly to gaseous cross flow, a setup had to be constructed to deliver a high- speed cross flow along with a column of liquid. The primary provider for the cross flow of air was a high-speed open circuit wind tunnel (University of Oklahoma, North Campus). A variable speed controller was used along with the wind tunnel to vary the velocity of the air in the test section. A water flow system was also constructed to deliver the water as the jet issued perpendicular to the cross flow in the test section. A detailed schematic diagram of the open circuit wind tunnel, schematic

of the water delivery setup, along with a picture of the setup are found in figures 2.1, 2.2, and 2.3, respectively.

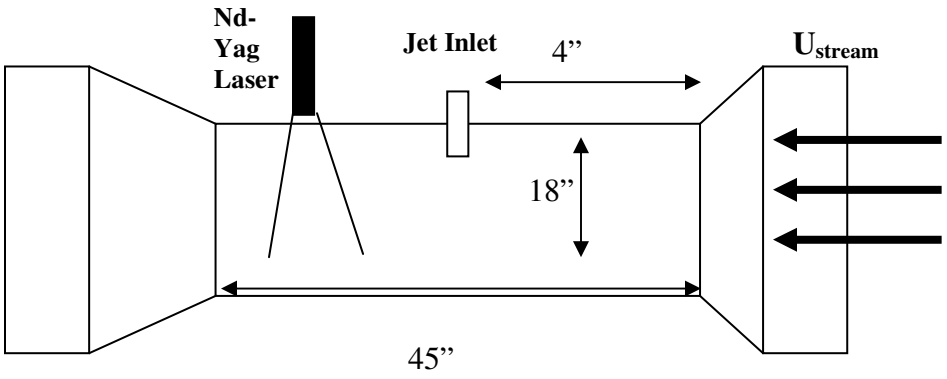


Figure 2.1 Open circuit wind tunnel

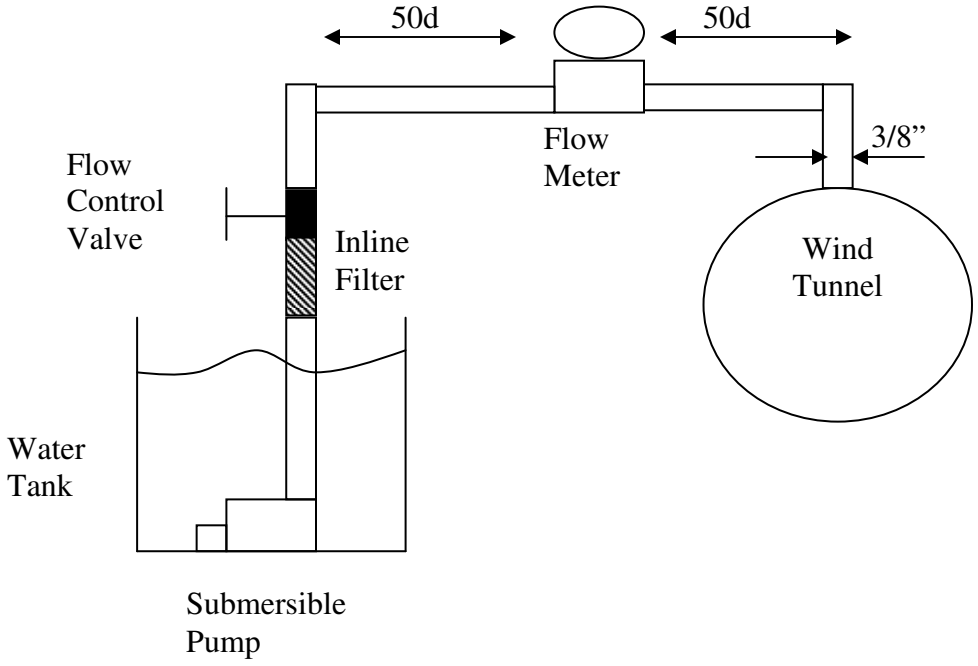


Figure 2.2 Water delivery setup

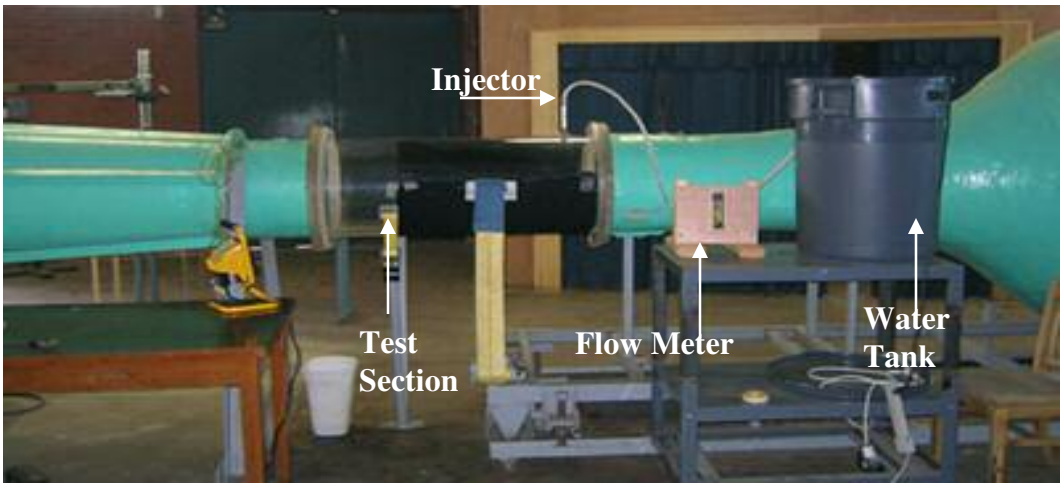


Figure 2.3 Experimental Setup at North Campus

The wind tunnel is a suction type open circuit wind tunnel that is open to the atmosphere at the discharge, with a 5 foot inlet, and 18" diameter circular clear plexi-glass test section that is 45" long. The inlet of the wind tunnel has a turbulence screen and honeycomb to damp out any inlet turbulence that may be carried to the test section. The liquid injector is placed 4 diameters from the start of the test section, and injects the liquid downward into the cross flow of air. A submersible pump at the bottom of the fluid reservoir pushes the fluid through the flexible tubing, rotameter flow meter, and into the injector. The electric motor, which drives the wind tunnel fan, is attached to a Cuttler-Hammer frequency controller (SVX9000). Using the motor controller and a ¼" pitot static probe with a pressure transducer a calibration was completed to relate the frequency output with the measured air velocity in the test

section from the pitot probe (figure 2.4). The pitot probe was placed in the test section at various heights. An average of all the measured velocities at various locations in the test section was taken with an uncertainty in the values of 5%. The estimated thickness of the boundary layer along the wall was no more than 12 jet diameters from the wall. The mean velocity in the test section was used to formulate the calibration curve. Using this calibration, a desired cross flow velocity may be set as a function of the output frequency of the motor controller.

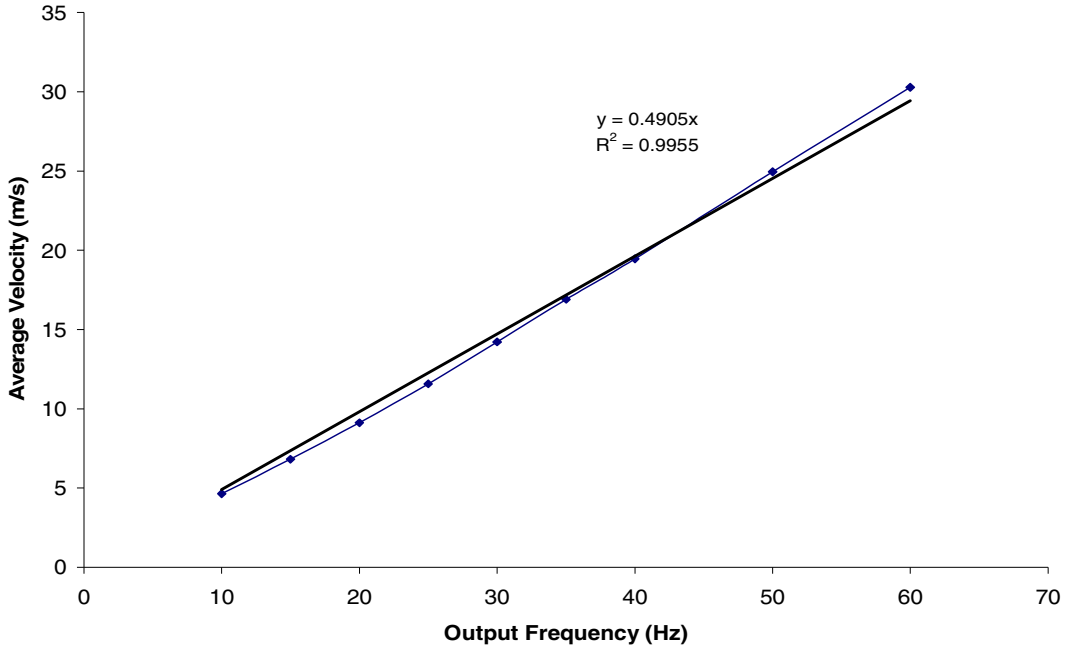


Figure 2.4 Wind Tunnel Calibration of test section velocity (m/s)

The calibration shows a linear trend with a very good correlation coefficient ($R^2 \approx 1$) between the equation and the actual data. This linear calibration equation was

used to set the wind tunnel cross section velocity to vary the momentum value, q, for the remainder of this study.

2.1.2 Flow meter

The flow meter used in the setup was an OMEGA 65 mm FLD series direct read rotameter flow meter. The flow meter came standard with a flow adjustable needle and a flow range of 0.2-1.2 lpm. The position of the float is linearly proportional to the flow passing around it. The float is read at the center of the ball, with a measured accuracy of ± 5% of full scale with a repeatability of ± .25%.

To ensure that the flow readout is entirely accurate, a validation procedure was used to compare the indicated flow reading to the actual flow rate measured. Testing showed that the flow meter had an average of 3.5% error, when compared to the actual flow rate. The actual flow rate was determined by filling a bucket to a 1 gallon level. The time to fill the bucket was recorded and used to calculate the actual flow rate. This was compared to the indicated flow rate, and plotted against one another. The data showed a linear relationship between the two flow rates, whereby a linear fit was used to determine a calibration equation for future flow rate settings (figure B1, Appendix B). The validation procedure showed a very good agreement between the indicated flow rate and the measured flow rate with an average error of 3.5%, which is well within acceptable range for this study.

2.1.3 Submersible Pump

The primary fluid mover of the experiment was a Little GIANT compact submersible centrifugal pump. The pump has a screened inlet to filter out large particles with a ½ inch Male NPT outlet. The pump has a flow range of 13.5-.8 gpm at 1 and 24 feet of head, respectively. Since pump is centrifugal, the flow rate is greatly sensitive to the downstream head loss. This meant that accurate flow control can be achieved using a needle style flow control valve, which can greatly increase or reduce downstream head. The submersible pump was fitted to the flow setup taking into account all major and minor losses in the system to assure that proper flow was deliverable.

2.1.4 Injector Design

The water jet was designed to provide a steady flow. Standard tap water was used as the injected fluid. The fluid properties were as follows: a density of 998 kg/m^3, a kinematic viscosity of 1.13E-6 m^2/s, and a surface tension of 0.07073 N/m. A Cannon-Fenske Capillary tube viscometer was used to measure the fluid viscosity, while a CAHN flat plate surface tensiometer (Courtesy of OU Chemical Engineering) was used to measure the surface tension. The flat plate tensiometer works by measuring the force on a plate, which is pulled through the surface of the test liquid. With knowledge of the perimeter of the plate, the surface tension is found. The tap water was found to have a 3.5% difference in surface tension than pure distilled water, which was also measured for comparison purposes.

A 2 mm inner diameter injector made of stainless steel was selected with a 2" exit length, and made from aluminum. Designing the jet with an exit length of 25 jet diameters, ensures that the flow is fully developed when exiting the nozzle. To limit the presence of vortices in the flow, a gradual reduction with a 45° taper was designed taking the cavity from a ¼" diameter to 2mm diameter smooth exit. A schematic diagram of the injector is presented in figure 2.5.

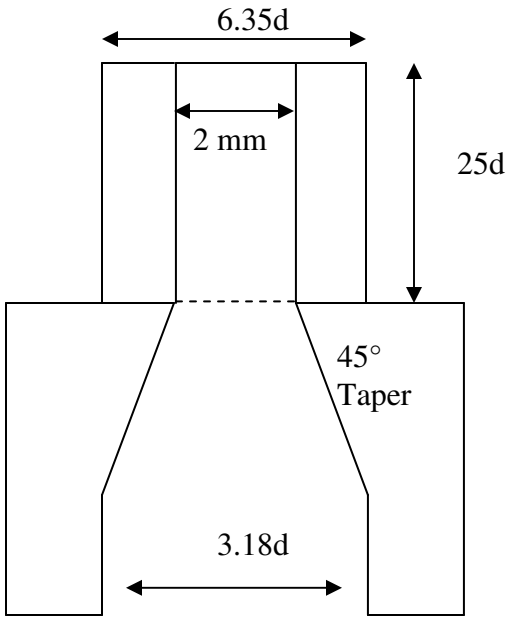


Figure 2.5 Water jet injector design.

2.1.5 Flow System Hardware

The piping used to deliver the fluid was 3/8" high pressure flexible rubber tubing. The flexible tubing allowed for minimal head loss, and provided ease of use

without complex tube bending. All the components of the flow system are summarized in Table 2.1

Table 2. 1 Flow system components

Description	**Specification**	**Accuracy**
Flowmeter	OMEGA 65mm FLD Series	±5% F.S.
Fluid Pump	Little Giant 13.5-.8 gpm	NA
Fluid Piping	3/8" High Pressure Flexible Hose	NA
Handheld Pressure Transducer	OMEGA HHP-90	±0.2% F.S.

2.1.6 Particle Image Velocimetry System

A TSI Powerview™ Particle Image Velocimetry (PIV) system (Figure 2.6) was used to measure flow velocity. A double-pulsed Nd:YAG laser (90 mJ/pulse, 6 ns pulse time) was used to provide the light source through the test section of the

wind tunnel. The time in between pulses (dT) was varied at values of 6-30 μs, depending on the momentum ratio studied. Higher cross flow velocities required a shorter dT due to the movement of the particles within each interrogation volume. The light scattered from the seed particles was captured by a CCD (charge coupled device) camera with a 28mm lens (30Hz frame rate, 355μs shutter time, and 2.8 f#). The camera has a pixel resolution of 1200 x 1600 pixels, with each pixel being 7.4 x 7.4 μm. The laser and CCD camera were controlled using a Laser Pulse™ Synchronizer. The synchronizer was programmed using an INSIGHT 3G-2TDR software which provided data acquisition, analysis, and display. Processing of the images was achieved by using a Nyquist Grid with a spot size of 32x32 pixels. The Fast Fourier Transform (FFT) correlator was chosen with a Gaussian Peak engine, and signal to noise ratio (SNR) filter set at SNR filter > 1.2.

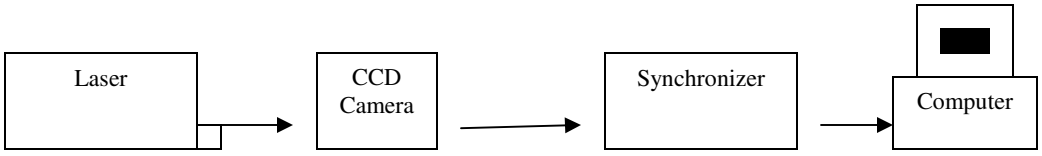


Figure 2.6 TSI Particle Image Velocimetry setup

2.1.7 PIV Background

Particle image velocimetry is a non-intrusive technique for flow measurement using a two-dimensional laser light sheet. A laser beam is formed into a 2mm two-dimensional sheet using a combination of cylindrical lenses. The light sheet can be arranged parallel or perpendicular to the direction of flow, with the receiving optics oriented perpendicular to the plane of light.

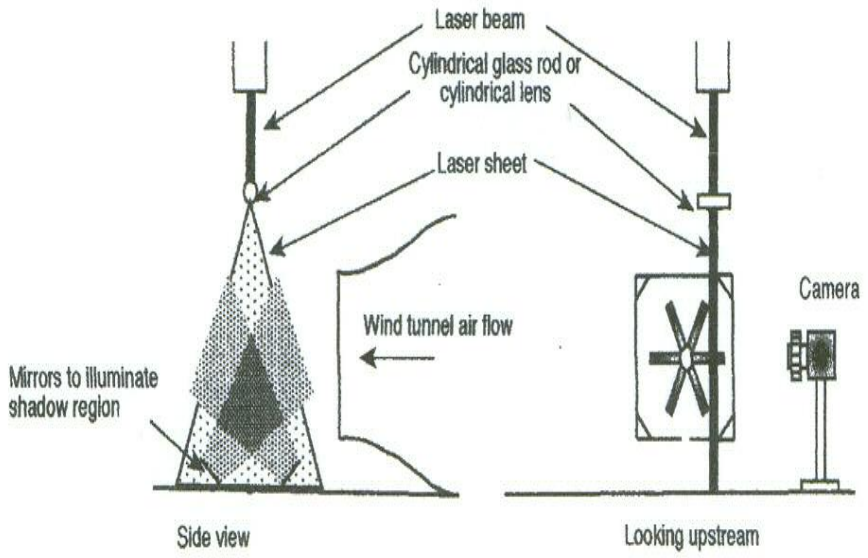


Figure 2.7 Illustration of a typical PIV arrangement in a wind tunnel (Courtesy of Grant 1997).

One possible arrangement of the PIV set-up in a wind tunnel is illustrated in Figure 2.7. The thickness of the light sheet is dependent on the cylindrical lens characteristics. The flow is "seeded" with small particles, and the particles are tracked as they pass through the light sheet. The tracking is achieved by pulsing the laser a number of times with very short pulses in duration. The scattered light from

the seeded flow is captured using either a digital camera or photo paper. Each photo paper includes both pulses capturing the movement of the particle within the photo paper. The average number of particles found in a cylindrical resolution cell (Figure 2.8) is defined as the source density. If the source density $N_s>>1$, then there is a high particle density in the flow and interference from the scattered light will occur. If $N_s<<1$, then the flow has a low particle density and is then referred to as low density PIV.

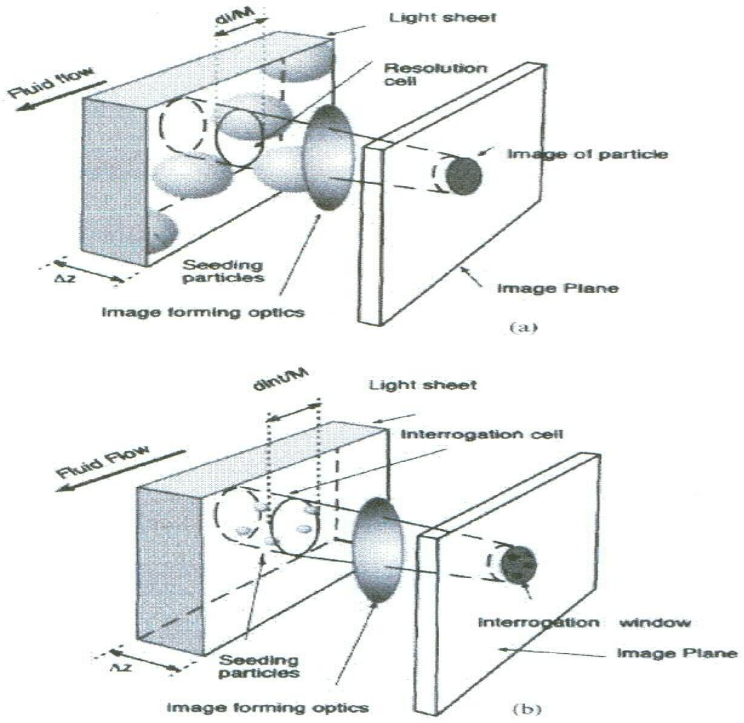


Figure 2.8 Illustration of the "interrogation" cell for source (a), and image density (b) (Courtesy of Grant 1997).

Figure 2.8 shows the test volume from within the thickness of the incident light sheet. The "interrogation" window is defined as the intersection of the light

sheet with the image window. The image density N_I is very similar to the source density, but is a measurement of the density of the particles within the "interrogation" window on the photo sheet. In other words, it is a measure of the number of particles within an elemental volume focused on the receiving optics. For $N_I<<1$, the image is said to have low image density. For high image density cells, it becomes difficult to discern complimentary pairs of a particle requiring extensive statistical measures to determine which particles coincide. An example of a high seeding density image is found in Figure 2.9.

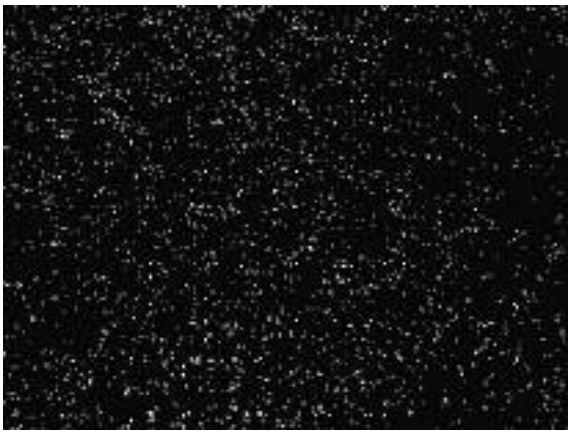


Figure 2.9 Double pulsed particle image (courtesy of Dantec Dynamics.com)

While older methods utilize PIV transparency sheets to create Young's fringe patterns, advances in PIV methodology allow for the image to be captured and digitized using a CCD camera (Grant 1997). Using the CCD, and post-processing software, autocorrelation of what is done through digital transformation. The CCD allows for real time data collection that can be monitored for the SNR. The real time

data stream allows for the user to adjust the autocorrelation techniques, spot size, pulse time, as well as the beam intensity to attain a more desirable SNR. Optimizing the signal to noise ratio helps to reduce the number of bad measurements that may arise due to light noise in the image. After the image pair is digitized an autocorrelation technique must be chosen to relate each seed particle captured from one time step image to the next. The user specifies an "interrogation area" which is made up of a group of pixels in the image (figure 2.10). Within each "interrogation area" correlation produces signal peaks relating each individual particle movement from one laser pulse to the next. The correlation process produces three peaks with the two end peaks being located at ±ΔX, where ΔX is the displacement of the individual particle from one image to the next. With knowledge of the change in position of the light intensity peak as a function of laser pulse time, the velocity magnitude and direction can be resolved.

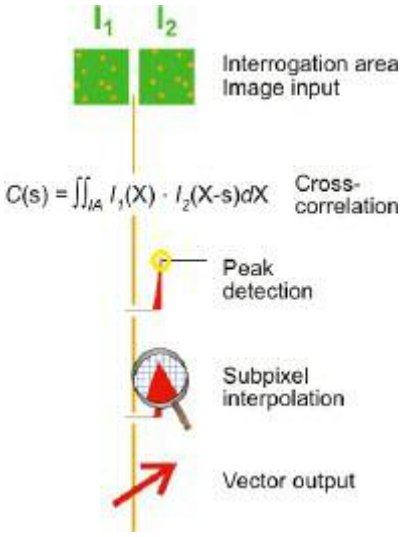


Figure 2.10 Schematic of the image capture process (Dantec Dynamics.com).

Currently, the autocorrelation is computed automatically by the PIV software giving the user several autocorrelation options resulting in the same peaks seen in figure 2.10. The end result is a processed set of images with velocity vectors throughout the field of view (FOV). After all images have been processed, several post-processing techniques such as erroneous vector removal, and vector interpolation allow the user to optimize the final image accuracy, also included in the PIV software package. Other post processing techniques may be used to get more information from the vector field such as, velocity biasing, strain rate information, vorticity contours, and various other turbulence quantities (figure 2.11).

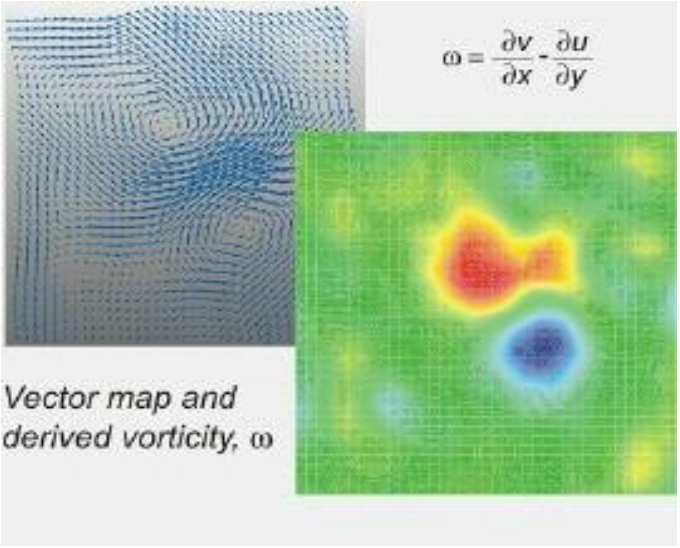


Figure 2.11 Vector and vorticity contours from PIV measurements
(courtesy of Dantec Dynamics.com)

. The validity of PIV measurements is hinged on the ability of the seeded particles to accurately follow the flow. Some research in the past has been devoted to this subject. Using the particle dynamic equations, taking into account the steady-state drag force, gravitational force, mass effect, fluid acceleration, and the Basset force, Lecuona et al. (2002) modeled particle trajectories in strong vortices. A non-dimensional time scale, called the Stokes number, was used to relate the particle response time to the flow response time.

$$St = \frac{\omega d_p^2}{18\nu\varepsilon} \qquad \text{(eq. 5)}$$

Where, ω is the vortex frequency of revolution, d_p is the particle diameter, ν_c is the fluid kinematic viscosity, and ε is the ratio of the density of the fluid to the density of the particle. It is generally accepted that particles with Stokes numbers less than 0.1 will follow the fluid streamlines accurately. For this particular study, the particle diameters were distributed around a mean diameter of 1μm, with fluid and particle density ratios of the order of 10^{-3} (corresponding to water seeding). For the Rankine vortex, the tangential velocity at the edge of the vortex was 25 m/s with a vortex radius of 0.05m. Rankine vortices have a solid rotation at the center, where the tangential speed in the vortex is inversely proportional to the distance from the center. Lecuona et al. (2002) showed that with single injection, particles tended to migrate away from vortex centers creating particle-free zones. The lack of high

seeding density in the vortex center was shown to result in velocities, which were in error when comparing PIV results of azimuthal velocities with theory, at various radial coordinates. This is one of the drawbacks of PIV measurements in low particle-density zones. The lack of particles results in low signal to noise ratio, and requires larger spot sizes, which increase the chance for erroneous image pairing throughout the entire flow field.

Khalitov and Longmire (2003) studied the response of glass beads in a fully-developed turbulent channel flow of air. Five different particle sizes were used with Stokes numbers ranging from 0.2-10, based on the integral time scales. To calculate these Stokes numbers, the authors used the channel half width (h) and the gas streamwise fluctuation (u') in the calculation of the dissipation $[(u')^3/h]$ and integral fluid time scale (h/u'). The authors were interested in determining the ability of these monodisperse spheres to track the flow using slip velocities, single point, and two point correlations. Each measurement was compared to "true gas" measurements made using 1μm size fog particles (glycerin droplets). The results showed that larger particles ($St > 1.4$) lagged behind the gas flow at the centerline, and moved faster at the walls. The researchers also showed that smaller particles tend to congregate in low speed streaks. Drift velocities in the center plane where shown to be small for all the range of particles tested. Both two point and single point correlations were shown to decrease with increasing particle size (increasing Stokes number). Stokes numbers less than 1 showed very good correlations to the gas flow in turbulent channel flow.

Using the definition of the Stokes number, the findings of Lecuona et al. (2002), and Khalitov and Longmire (2003), it is assumed that particles with Stokes numbers less than 1 will accurately follow the flow. Based on values from Ferziger et al. (1999), Kelso et Al. (1996), the Stokes numbers were computed to range from 0.004-0.4 for olive oil drops with a mean diameter of 1 μm. Particles of similar diameter, with less density would follow the streamlines with minimum deviation. Therefore, particles of nominal diameter of 1μm were chosen as seed particles in this study.

2.1.8 Two Phase JICF Methodology

The primary objective of this research is to track the cross flow and its interaction with the liquid jet. Researchers have surmised that the body of the jet acts much like a cylinder in a cross flow due to marked density difference between the cross flow and the jet fluid. For high $q > 6$, researchers have shown that a straight column of liquid is present for some distance, before droplets are stripped off the body of the jet by the cross flow. Also, the Reynolds number for the flow around a cylinder may be calculated using the diameter of the jet, similar to single phase JICF. For the flow around a cylinder, unsteady vortex shedding is onset at Reynolds numbers greater than 40. Both of these factors are influenced by the jet exit velocity and cross flow velocity. Using both of these parameters, the jet diameter and velocity are set at fixed values, while the cross flow velocity is variable.

Taking into account the momentum ratio, q, a jet diameter of 2mm was used with a jet exit velocity of 3.25 m/s. Using the jet diameter, the Reynolds number for the flow around the jet was calculated and the cross flow velocity was varied. The various test parameters used in this two-phase JICF study are summarized in Table 2.

Table 2. 2 Select Experimental parameters for two phase JICF

U_∞ (m/s)	U_j (m/s)	Re_∞	Re_j	q (momentum ratio)	Weber Number	Re_{cyl}	Stokes Number (St)
7.28	3.25	2.03E5	5,752	172.80	1.72	890	0.004
11.50	3.25	3.21E5	5,752	69.25	4.30	1,405	0.006
15	3.25	4.19E5	5,752	40.70	7.32	1,833	0.008
22.07	3.25	6.17E5	5,752	18.80	15.85	2,700	0.231
30	3.25	8.38E5	5,752	10.18	29.29	3,667	0.481

For each case, the jet velocity was held constant while the cross flow velocity is varied. The momentum ratio (q) was set at values greater than 6 to ensure that a proper column of liquid was present before any instabilities were formed, or break up in the jet body began. At each cross flow velocity, the Reynolds number based on the

diameter of the test section (Re_∞) is given along with the Reynolds number for the jet based on the jet diameter (Re_j). Additionally, for each case, the Reynolds number based on the jet diameter (Re_{cyl}) was greater than 40, leading to the onset of vortex shedding in the wake of the jet. The Stokes number was calculated using the findings of Lecuona et al. (2002), and Khalitov and Longmire (2003). At every cross flow velocity, the Stokes number was less than 1, leading to proper flow tracking within the wake vortices using the 1 μm sized olive oil droplets. The olive oil seeding will be only used to validate the wind tunnel calibration that will follow. Due to oversaturation of the CCD camera from the large droplets of water, the Mie scattered image had to be filtered out to prevent from damaging the camera. Using the findings of Cessou et al. (2005), laser fluoresceine tagging was used to track the gas phase in this setup. Cessou et al. (2005) successfully showed that at 532 nm, Rhodamine 610 could be used to track the gas flow in a multiphase flow such as this.

For this study, Rhoadime 610 perchlorate was initially chosen. Rhodamine 610 percholorate is a mildly toxic fluoresceine powder, which when illuminated by an Nd-YAG laser, is excited to wavelengths ranging from 570–620 nm. The powder is only dissolvable in either methanol or ethanol. When dissolved in ethanol at a molar concentration of 4.2E-4, and excited by a laser of 532nm, Rhodamine 610 fluoresces to a maximum wavelength of 596nm (exciton.com). Ethanol was initially chosen for this case because of its ease of purchase and safety. However, due to the low vapor pressure of ethanol and methanol, both fluids could not be used in the high-speed cross flow, such as the one used in this study.

Kiton Red 620 is a powder, similar to Rhodamine 610, but is completely soluble in water. When excited by a 532 nm laser, Kiton Red 620 fluoresces in the range of 570-604 nm. To help raise the vapor pressure, 50 ml of Ethylene Glycol was added to the water to further prevent any evaporation that might occur before reaching the illumination region of the wind tunnel.

Since only the fluoresced light is of particular interest, all incoming green laser light into the camera must be filtered out. An OMEGA optical filter, which attenuated all wavelengths below 550nm and passed all wavelengths above 550nm, was used (Figure 2.12). The mixture of water and Kiton Red 620 was atomized in a TSI Model 9306 aerosol generator, which produced drops of less than 1μm in diameter. The drops were injected through a 1" hose 4' upstream of the liquid jet, to avoid any disturbances due to injection of the seeding. With this setup, the Mie scattered light from the body of the jet was filtered out and the fluoresced light from the seeding in the gas phase was tracked. Not only was the CCD camera safe from over saturation, but a clear distinction could now be made between the signals from the atomized particles and the signals from the jet and tracer particles in the gas flow, thereby reducing any errors that might arise due to interference between the signals from the two phases.

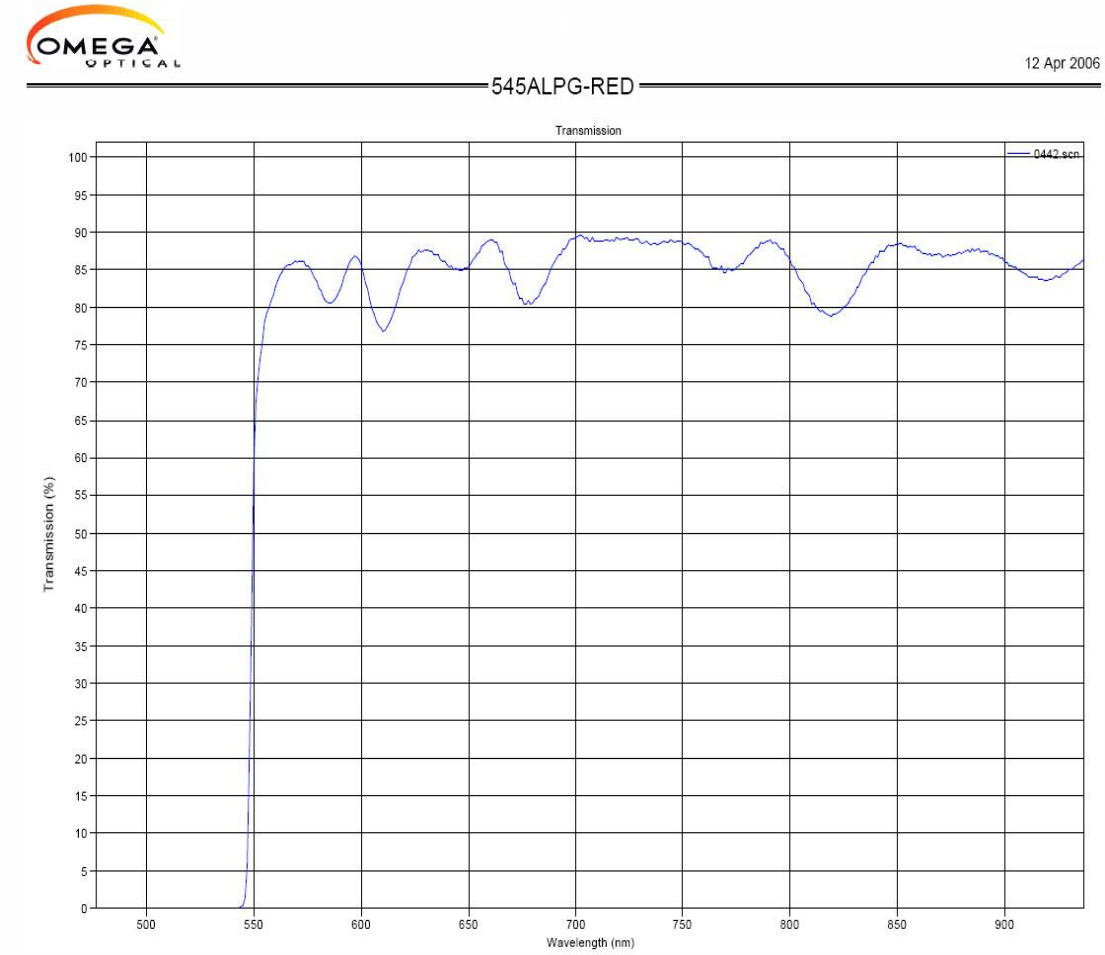


Figure 2.12 Transmission spectra for optical filter
(courtesy of TSI.com)

CHAPTER 3

COMPUTATIONAL RESULTS

3.1 Computational Results

FLUENT's Volume Of Fluid (VOF) solver was used to model a two phase time dependent 2-d JICF. The VOF solver uses standard continuity and momentum equations to model the motion of the two phases as they move through the domain.

$$\frac{\partial}{\partial t}\rho u_j + \frac{\partial}{\partial x_i}\rho u_i u_j = -\frac{\partial P}{\partial x_j} + \frac{\partial}{\partial x_i}\mu\left(\frac{\partial u_i}{\partial x_j} + \frac{\partial u_j}{\partial x_i}\right) + \rho g_j + F_j \qquad \text{(eq. 6)}$$

The complexity arises when the two fluid phases come into contact. This is where the VOF solver is unique. Properties such as the density (ρ), and viscosity (μ) must be known apriori before the momentum equations can be solved. Each cell is assigned a volume fraction value (α) for the magnitude of the phase which is present within each cell. The interface tracking between the two phases is accomplished by solving a continuity equation for each phase.

$$\frac{\partial \alpha}{\partial t} + u_i \frac{\partial \alpha}{\partial x_i} = 0 \qquad \text{(eq. 7)}$$

The volume fraction value within each cell is used to calculate the density (ρ), and viscosity (μ) of the fluid mixture within that cell. With knowledge of the fluid properties in a cell, the momentum equations may be solved.

$$\rho = \alpha_2 \rho_2 + (1 - \alpha_2)\rho_1 \qquad \text{(eq. 8)}$$

$$\mu = \alpha_2 \mu_2 + (1 - \alpha_2)\mu_1 \qquad \text{(eq. 9)}$$

Further complexity arises when reconstructing the shape of the interface between the two fluids. To achieve this FLUENT gives the user a couple options. For this particular study the geometric reconstruction scheme was used, due to its simplicity. The geometric reconstruction scheme utilizes a piecewise linear interpolation of the boundary within each cell. Using the volume fraction and the volume fraction derivatives within a cell, the scheme determines the position of the linear interface relative to the center of each partially filled cell. Next the solver calculated the amount of advecting fluid through each face using the linear interface representation and information of the normal and tangential velocities on the face. Finally the volume fraction in each cell is calculated through the balance of fluxes calculated in the previous step. For this type of boundary reconstruction scheme, a time dependent solution had to be chosen.

To validate the findings, results from a two phase time dependent liquid free jet simulation were compared to published theory. Initially, however, a flow domain was constructed using GAMBIT for both the free jet and 2-d JICF simulations. For the free jet an axisymetric domain was constructed with the jet inlet at the left of the domain, and outflow conditions at the outer boundaries (figure 3.1). The outflow condition was shown to give more accurate results which converged to a final solution. For the 2-d JICF the left boundary was a specified velocity, with the top and

far right boundaries being an outflow boundary condition. The bottom boundary was specified as a wall.

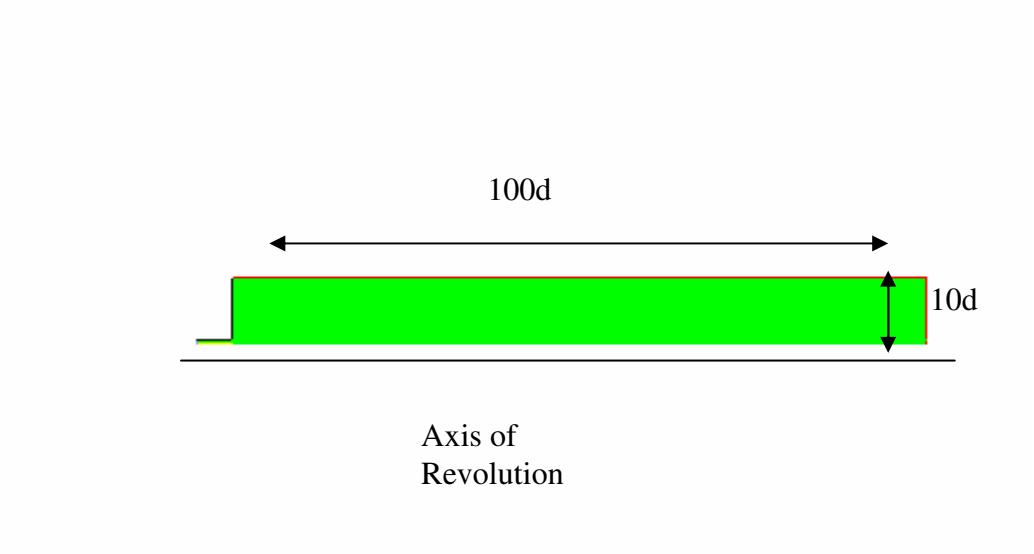


Figure 3.1. Computational domain for free jet

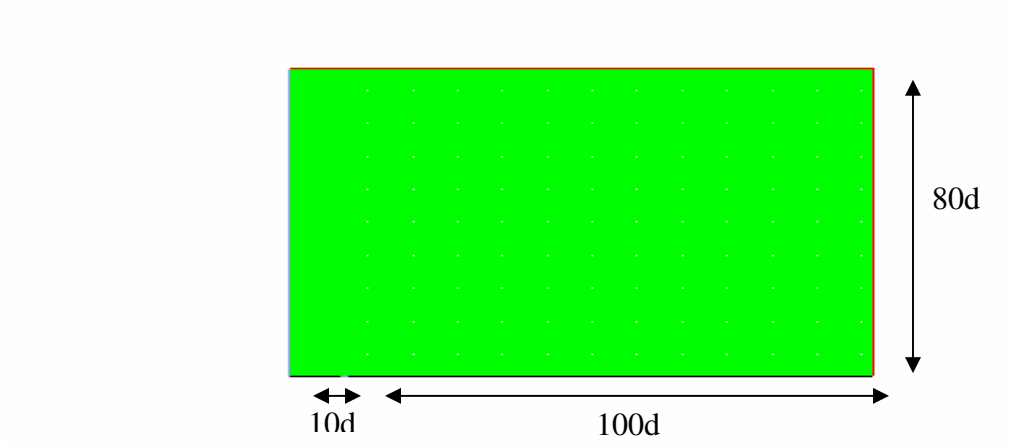


Figure 3.2. Computational domain for 2-d JICF

The meshing scheme using was a standard square mesh with smaller grids near the jet exit and immediately downstream of the exit. The free jet domain was shown to be grid independent, and time independent by showing that the initial break

up location for each case was independent of time step and grid size. The solution showed grid independence with 57,000 cells.

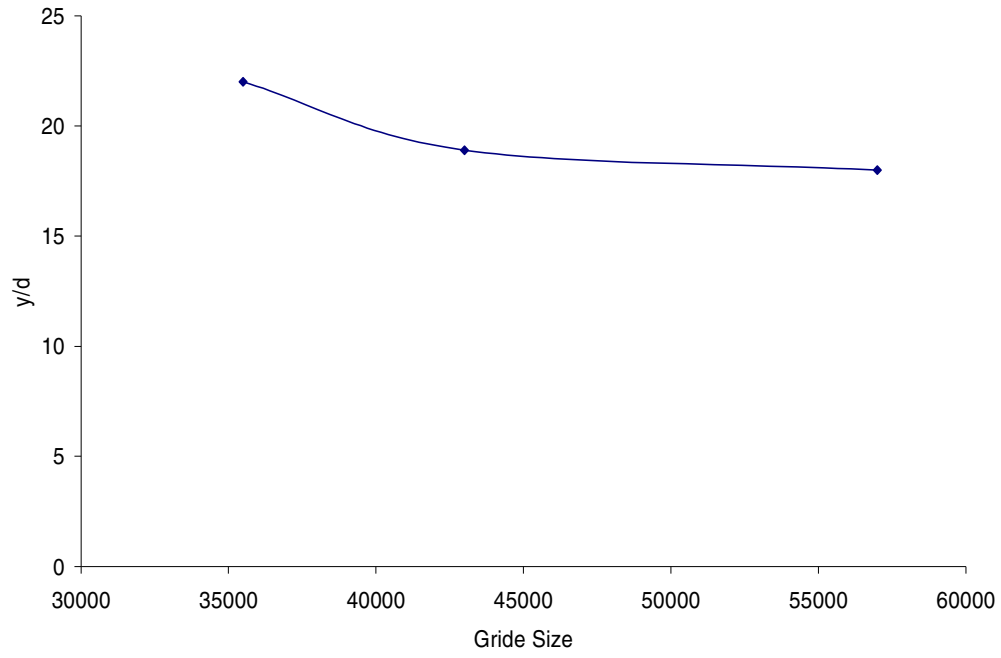


Figure 3.3. Break up locations of a free jet for various grid sizes.

For the 2-d JICF the domain was shown to be grid independent by comparing the equivalent diameter for each case. The equivalent diameter is specified as a ratio between the droplet mean diameter, and jet diameter. The results became grid independent with 56,800 cells.

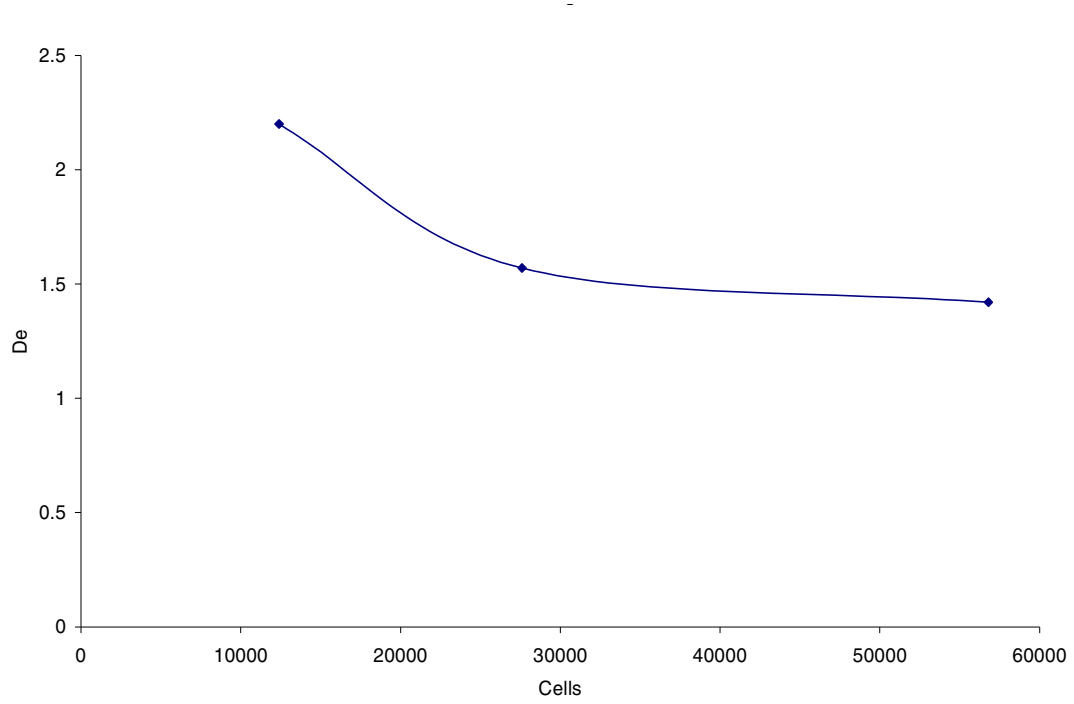


Figure 3.4. Convergence of equivalent diameter with grid size for a 2-d JICF.

To validate the results from the VOF solver, the results of the free jet were compared to theoretical results from a Rayleigh instability analysis and compared with the droplet diameter from the VOF solution. The droplet sizes were determined by measuring the size of the first droplet to break off the liquid column. Lord Rayleigh found that the largest disturbance wavelength that leads to break up was $\lambda = 9.016a$, where λ is the wavelength of disturbance, and (a) is the radius of the jet. If we assume that the entire volume of fluid of a single drop consists of the entire volume of one wavelength of instability then we can equate the two and solve for the droplet diameter.

Equation the two volumes, $\frac{\pi d^3}{6} = \pi a^2 \lambda$, and solving for $\frac{d}{2a}$, we find that the initial droplet diameter normalized by the jet diameter is 1.89. Comparing the solution from FLUENT's VOF solver of 1.42, it is found that the numerical simulation is 25% different than the theoretical solution of Lord Rayleigh. Thus, the following results are purely qualitative and only show general trends resulting from variations in the momentum ratio q.

Initially, a q value of 20 was used, where the cross stream velocity is $U_\infty = 1$ and the jet velocity is $U_j = 0.5$.

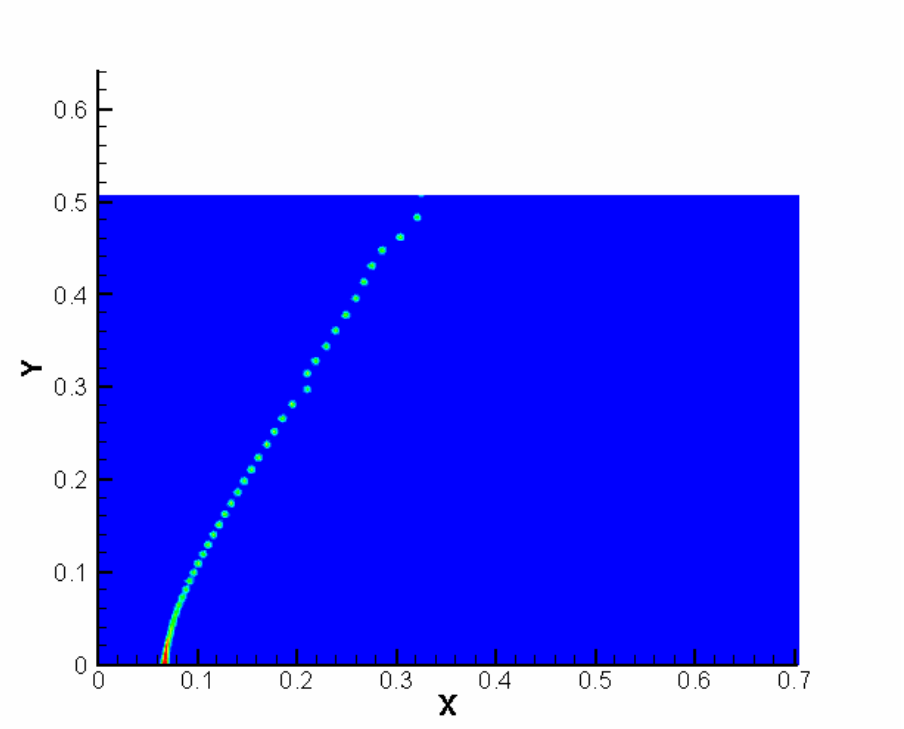


Figure 3.5. Volume of fluid solution for q=20.

Figure 3.5 shows the jet exiting from its outlet, and reacting with the cross flow. The red color indicates that the cell has a liquid volume ratio of 1, and the dark blue indicates a liquid volume ratio of 0. The plot shows that the jet is bent by the momentum of the cross flow and the shear forces break up the column of liquid. The break up location of the jet was found by analyzing the point at which the liquid column breaks up into individual droplets. This break up location was shown to be dependent on the momentum ratio q, as indicated by table 3.1.

Table 3. 1 Break up locations with varying momentum ratios.

	q= 20 (U_∞=1, U_j=.5)	q= 81.3 (U_∞=.5, U_j=.5)	q= 3252 (U_∞=.5, U_j=1)
Break up location (X/d) From jet	2.86	2	6.48
Break up Height (Y/d)	12.28	14	34.33

Table 3.1 shows that as the momentum ratios are increased, the break up location moves further in the x direction as well as the y direction. Simply put, the greater the momentum of the cross flow, the further the jet bends in the direction of the cross flow. Also, as the momentum ratio increases, the jet momentum increases pushing the jet further in the y-direction before shear forces from the cross flow break up the jet into individual droplets. When comparing the y break up location with the

finding of Fuller et al. (1997), moderate agreement is seen. Fuller et al. (1997) showed a break up location of Y/d=10.4, at q=20. The VOF solution gives a value of Y/d=12.28. Any agreement that may be seen at lower momentum ratios becomes very poor at higher momentum ratios. For example, at q=81.3, the VOF solution gives a Y/d break up location of 14, while the findings of Fuller et al. (1997) showed a break up location of Y/d=31 at the same momentum ratio. Due to the purely qualitative nature of this study, these differences are acceptable, but show some promise for the future of the VOF solver for two phase jet break up study.

At a q value of 81.3 the jet shows the least amount of bend in the direction of the cross flow (figure 3.6).

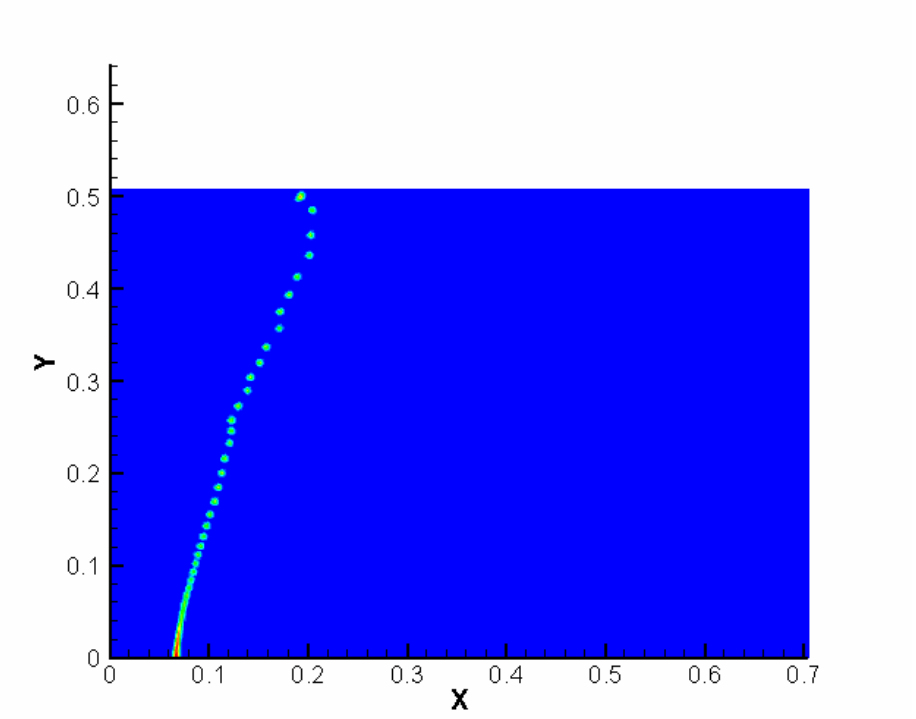


Figure 3.6. Volume of fluid solution for q=81.3

These initial computational results show qualitatively the general trends in the interaction between the cross flow momentum and jet momentum. These results will hopefully closely mirror the results of the experimental findings, on a qualitative level. In the future, comparisons will be made between the computational model, and the experimental findings.

CHAPTER 4

EXPERIMENTAL RESULTS

4.1 Experimental Results

4.1.1 Liquid Jet Analysis

To ensure that the break up of the liquid jet is entirely due to the aerodynamic forces introduced, the stability of the jet without a cross flow was studied. In figure 2.5, a schematic of the injector design can be found. The injector was designed in such a way to limit the amount of turbulence due to the change in cross section from a 6 mm exit to a 2 mm exit diameter.

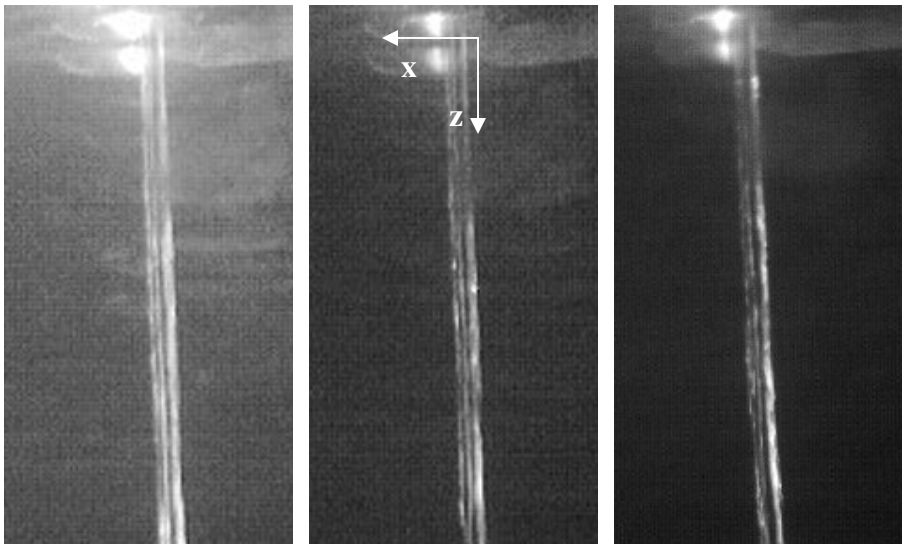


Figure 4.1 Images of 2mm water jet exit

Figure 4.1 shows a smooth column boundary of liquid with little to no instability in the boundary due to exit turbulence from the injector. The importance of this observation is to emphasize that any instabilities that might be found in subsequent cases is entirely due to the interaction between the liquid jet and the cross flow. The design of the injector is adequate in producing an un-disturbed water jet for this study.

4.1.2 Stability Analysis

The break up of a liquid jet in cross flow is greatly influenced by disturbances that grow along the upstream side of the jet. As Aalburg et al. (2004) illustrated, there are distinct disturbances of measurable wavelength, which can be found on the upstream side of the jet. These disturbances grow in amplitude and eventually lead to the break up of the liquid column. After the initial break up of the liquid column, large ligaments of fluid are separated and undergo a secondary aerodynamic break up mechanism breaking the ligaments up into smaller droplets (figure 4.2).

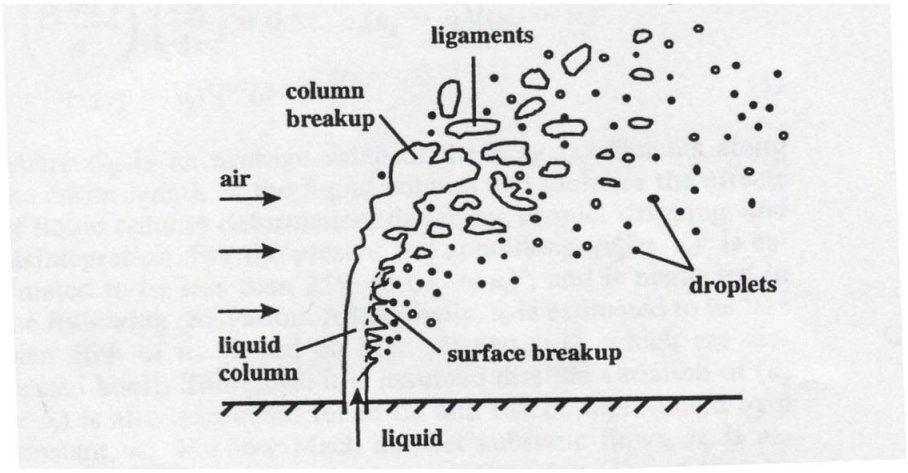


Figure 4.2 Illustration of the break up process of a two phase JICF (courtesy of Fuller et al. 1997)

There are four main classifications of the break up of a liquid jet, enhanced capillary break up, bag break up, multimode break up, and shear break up, at various critical Weber numbers. Capillary break up has characteristics similar to the break up of a free jet in still air, where disturbances form along the jet column leading to droplet separation. Bag break up is described by its presence of large ligaments, or "bags" of fluid separated from the break up point at the end of the jet. This type of break up generally has the highest amplitude disturbances before ligament separation. Shear break up is characterized by extreme jet bending, with little to no ligament formation. In shear break up, droplets are sheared off the sides of the jet as well as the rear of the jet (surface break up). Multimode break up is a combination of both bag break up and shear break up. In this regime, large ligaments of fluid are found as well as small droplets, in the wake of the jet. Fuller et al. (1997) were one of the first researchers to propose a distinct break up regime for the two-phase JICF at various

critical Weber numbers of 14, 35, and 80, for the onset of bag break, multimode break up, and shear break up, respectively.

Taking into account the critical Weber numbers of Fuller et al. (1997) and Aalburg et al. (2004), a study on the break up of the two-phase JICF at relatively low Weber numbers was conducted. Images of the jet break up can be found in figures 4.3 and 4.4, with a 255 μs exposure time.

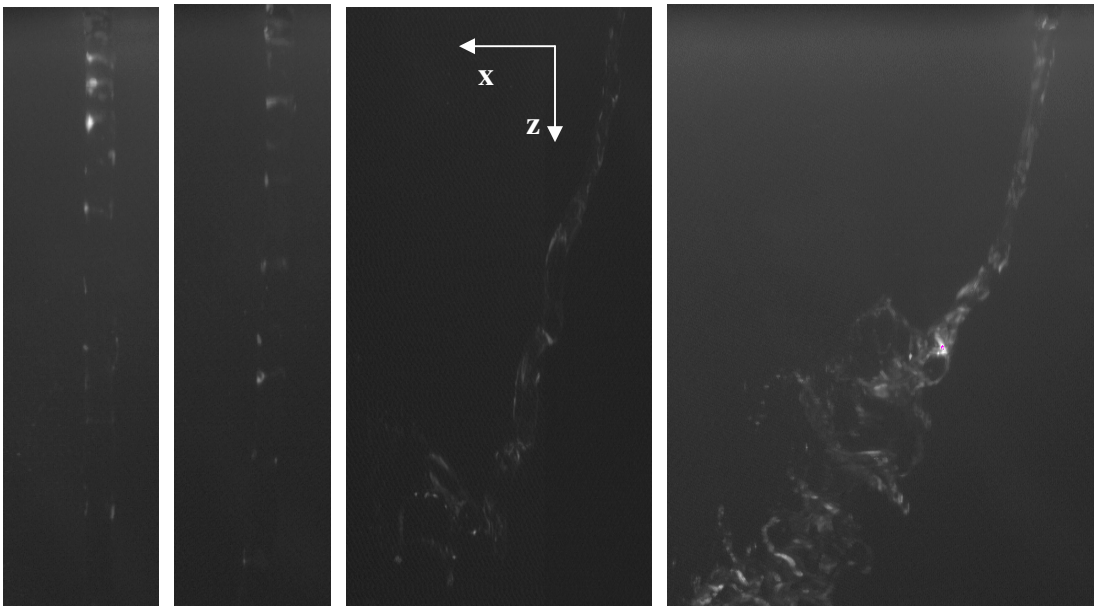


Figure 4.3 Visualization of the break up process of a water jet in cross flow: a) q = 172, We = 1.72, Column break up; b) q = 69.25, We = 4.3, Column break up; c) q = 40.7, We = 7.32, Bag break up; d) q = 18.8, We = 15.85, Multimode break up.

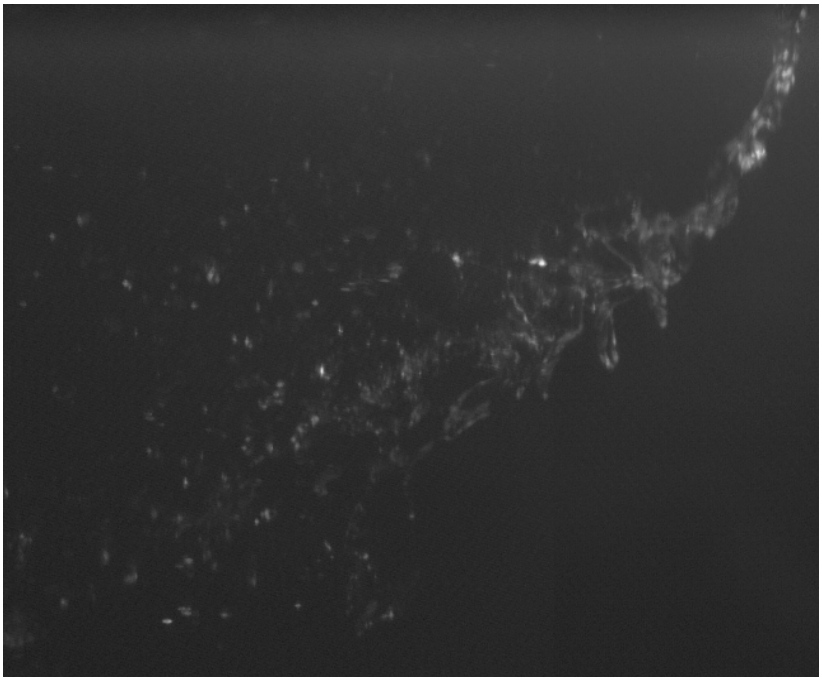


Figure 4.4 Break up process for q = 10, We = 29.29, Multimode break up.

In figures 4.3 and 4.4, a montage of the break up processes for the various momentum ratios is found. The transition from a bag break up with large ligaments, to multimode break up with some ligaments and some droplet shearing is seen. Figure 4.3(c) shows a bag like break up mechanisms, while figure 4.3(d) shows the transition to a multimode break up. Figure 4.3(d) shows the onset of multi-mode break up at a Weber numbers of 15.85. The onset of multimode break up according to Aalburg et al. (2004) does not occur until a critical Weber number of 30. However, this picture shows multimode break up at critical Weber number below 30.

At every momentum ratio, disturbances can be found on the upstream side of the jet in the X-Z plane. Most notable are the disturbances seen in figure 4.3 (c) and

(d). These disturbances grow in magnitude and lead to the fracturing of the liquid at the trough of the disturbance wave. Figure 4.4, shows very distinct disturbance waves on the upstream side of the jet. This type of multimode break up shows "bags" or liquid break off with small sheared droplets as well. The break up process appears to be much more violent in nature. The frequencies of these waves were measured similar the methods of Aalburg et al. (2004). Using a magnification scale, the distance between the centers of each "node" of the wavelength was measured as a function of the Weber number (figure 4.5), using a dial gage caliper. Due to the penetration of the low Weber number jets out of the FOV of the CCD camera, the disturbance characteristics in the jets corresponding to the Weber number range of 10-40 could only be measured.

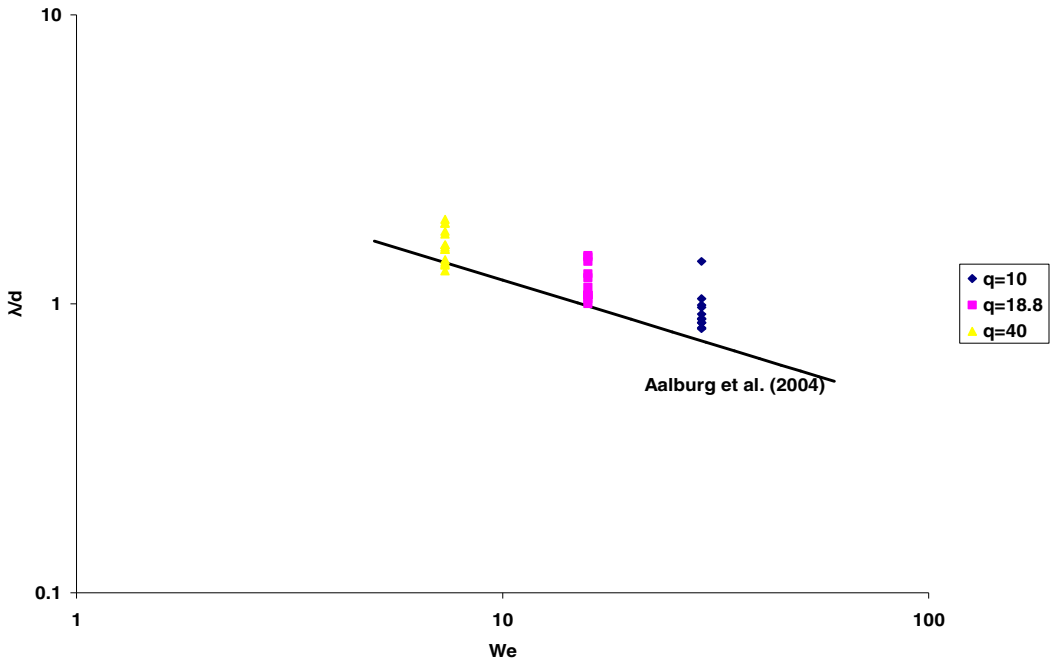


Figure 4.5 Disturbance wavelengths as a function of Weber number.

For each Weber number, 100 images were collected using the PIV CCD camera, where, on average, only 20% of the images had clear measurable wavelengths. Each reported wavelength has an estimated uncertainty of only 10% (95% confidence), with most of the uncertainty as a result of the deviation in measured values. The measured wavelengths decreased as the Weber number increased. This is a well-known trend for liquid jets injected into subsonic cross flows. The measured wavelengths were compared with the experimental curve fit of Aalburg et al. (2004). Good agreement is seen between the two results with a maximum deviation of about 25%. This result is reasonable considering that the published uncertainties of Aalburg et al. (2004) were on the order of ±25%.

Along with the disturbance wavelengths, the break up locations were documented and compared with previous results (Fuller et al. 1997, Aalburg et al. 2004). For this study, the vertical break up location (penetration into the stream), Z_b, as well as the streamwise break up location ,X_b, was measured using similar methods as the disturbance measurements (figure 4.6 and 4.7). Specifically, the streamwise break up location was defined as the distance from the center of the injector to the middle of the first disconnect in the liquid column. The break up height was measured as the distance from the wall to the middle of the first disconnect in the liquid column.

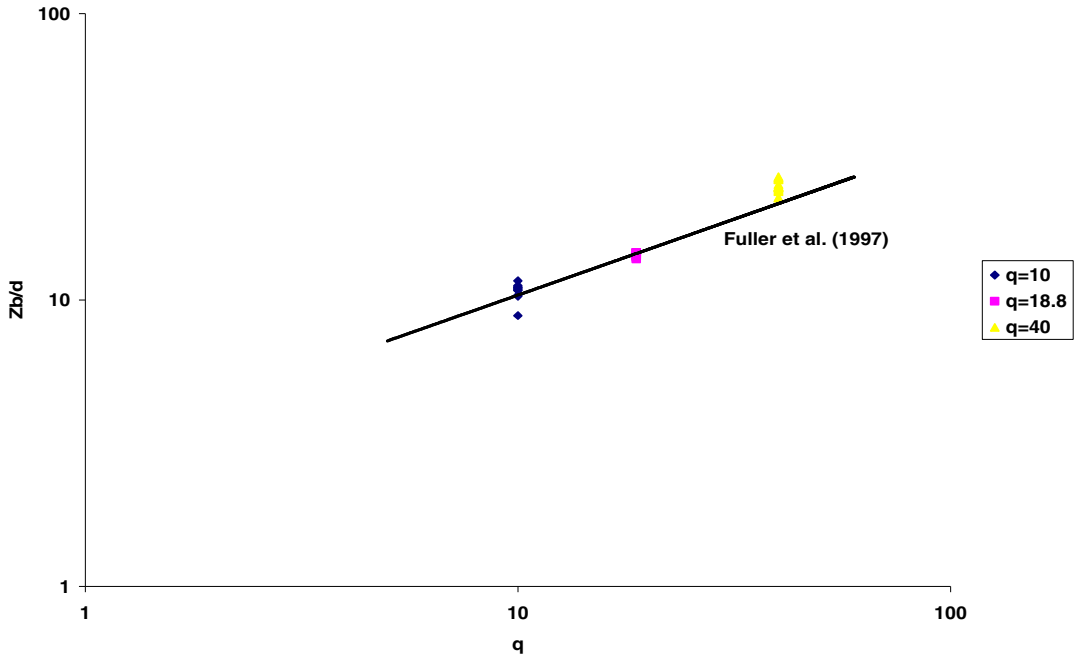


Figure 4.6 Non-dimensional break up location, Z_b, as a function of Weber number.

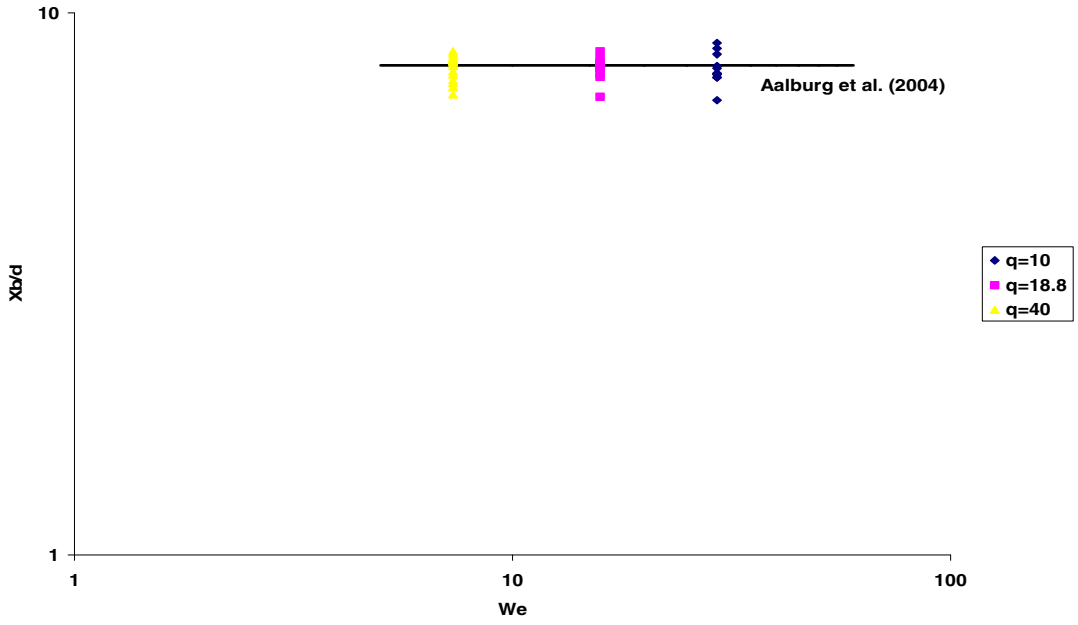


Figure 4.7 Non-dimensional break up location, X_b, as a function of Weber number.

Figures 4.6 and 4.7 show the non-dimensional break up locations for each Weber number tested. Each figure is plotted along with the published experimental curve fits of Fuller et al. (1997) and Aalburg et al. (2004). All primary break up locations are reported with a maximum of 10% uncertainty, and show excellent agreement with published results. The penetration of the jet decreased as the Weber number was increased. An increase in the Weber number implies an increase in the cross flow velocity, and therefore, an increase in the drag exerted on the jet. The increased drag on the jet results in a significant bending in the cross flow direction, and a decreased penetration. The streamwise break up location is shown to be independent of the Weber number and constant at a value of about 7.9 jet diameters for the present range of momentum ratios. The reasoning for this was first proposed by Fuller et al. (1997) who stated that the aerodynamic force, which accelerates the liquid, also reduces the time required for the column to break up affectively canceling both factors yielding a constant downstream break up location.

Using the same methodology as before, the trajectory of the jet was measured using a magnification scale at various downstream locations. Following a similar derivation first proposed by Fuller et al. (1997), the trajectory equation can be rearranged to solve for the drag coefficient (C_d) on the jet at various momentum flux ratios.

$$\frac{x}{d} = \frac{C_d}{\pi}\left(\frac{\rho_\infty U_\infty^2}{\rho_j U_j^2}\right)\left(\frac{z^2}{d^2}\right) \qquad \text{(eq. 10)}$$

Rearranging this equation to solve for C_d, it was found that the drag coefficient on the jet was 1.6, 2.22, and 2.05, at momentum flux ratios of 40, 18.8, and 10, respectively. Comparing the drag coefficient for a liquid jet with the drag coefficient on a solid cylinder, within the range of Re_{cyl} tested, similarities are seen. The drag on a solid cylinder in this Reynolds number range is constant at a value of 1.2, whereas the current findings show drag coefficients of very comparable magnitudes. For this reason, a liquid jet in cross flow can be assumed to act similar to a solid cylinder in cross flow in the near field.

While disturbances are in fact present in the X-Z plane, disturbances are also seen in the X-Y plane of the jet for the three lowest momentum ratios. The three-dimensional nature of the instability has been commented on by Aalburg et al. (2004), and various other researchers.

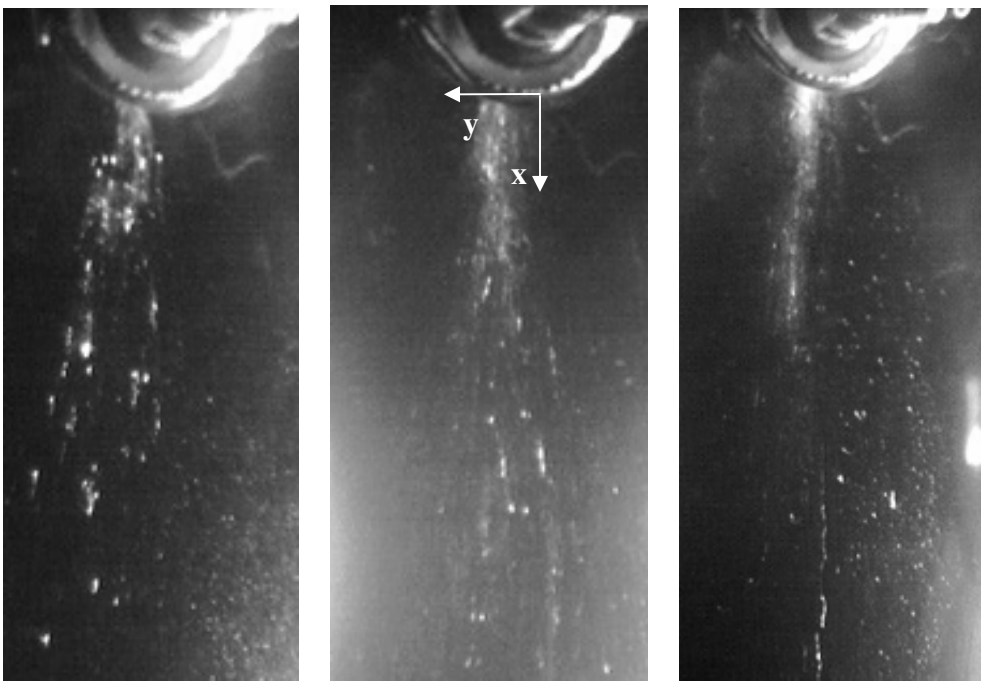


Figure 4.8 View of disturbances in the body of the jet in the x-y plane at: a) q = 40.7, We = 7.32, multimode break up; b) q = 18.8, We = 15.85, shear break up; c) q = 10, We = 29.29, shear break up.

From Figure 4.8, it is observed that the disturbances seen in the X-Z plane are also present in the X-Y plane. The higher momentum ratio images could not be analyzed in this plane due to the minimal bending of the jet in the downstream direction. The three-dimensional nature of the disturbance may shed some light on the influence of the wake on the break up of the liquid column. Aalburg et al. (2004) attributed the disturbance in the x-z plane to Rayleigh Taylor instabilities, which arise due to the shearing of a less dense fluid against a more dense fluid. This shearing occurs along the body of the jet, while in the X-Z plane the shearing occurs on the undisturbed portion of the spray very near the exit point of the jet. This column of

liquid may act like a cylinder in cross flow resulting in the shedding of vortices downstream of the jet. The periodic shedding of vortices would result in a pressure distribution along the circumference of the jet, which might lead to the formation of disturbances seen in figure 4.5. As the location of the flow separation changes, the resulting force direction would change, thus resulting in a change in the jet break up location.

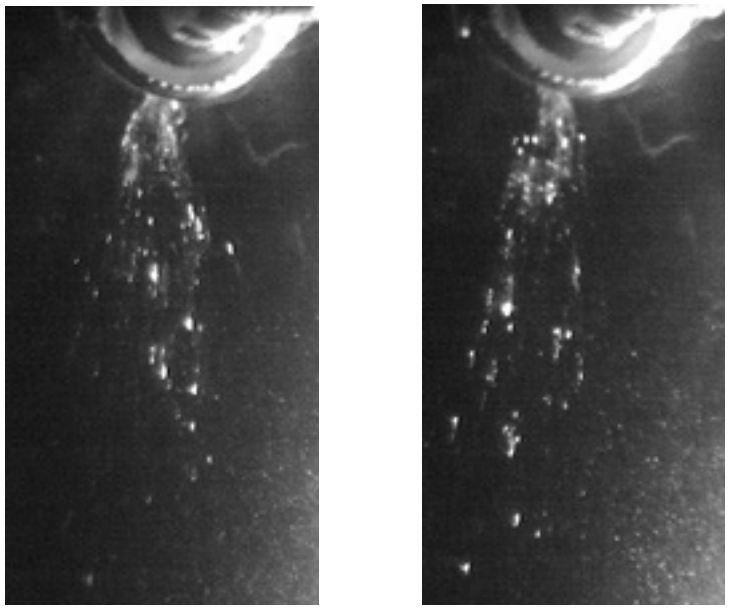


Figure 4.9 Transient nature of the break off point for q = 40.7

Figure 4.9 shows the change in the location of the break off point for q = 40.7, from the top of the jet surface. Throughout the course of the break up process, the jet appears to "wave" in a sinusoidal nature along the y-axis. As discussed, this transient nature in the X-Y plane may be attributed to a transient variation in the pressure distribution along the circumference of the jet.

In this section, the break-up characteristics have been described quantitatively and qualitatively. Taking into account all of the results from this study, and the published results of Fuller et al. (1997 & 1998), and Aalburg et al. (2004 & 2005), a spray characteristic matrix has been created. The matrix contains the ranges of the Weber numbers and momentum ratios from this study. The spray matrix is designed to allow a designer the ability to know what sort of spray break up could be expected with known non-dimensional Weber number and momentum ratio, at Oh < 0.1 (Appendix A table A23).

4.1.3 Spray Characteristics

The structure of the jet as it is atomized by the high speed cross flow is inherently three-dimensional, as figures 4.4 and 4.8 show. By placing the high-speed camera under the jet, a more detailed view of the jet break up process is revealed. Due to the increased penetration of the jet in the Z direction for high momentum values, images could only be taken for q = 10, 18.8, and 40.7.

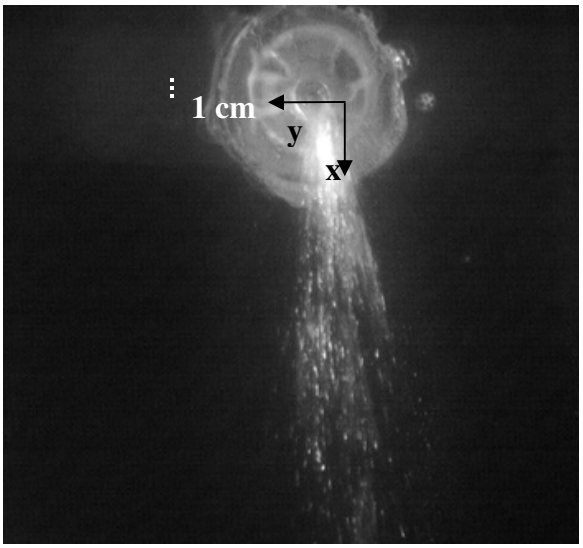


Figure 4.10 View of the jet spray for q = 10, We = 29.29.

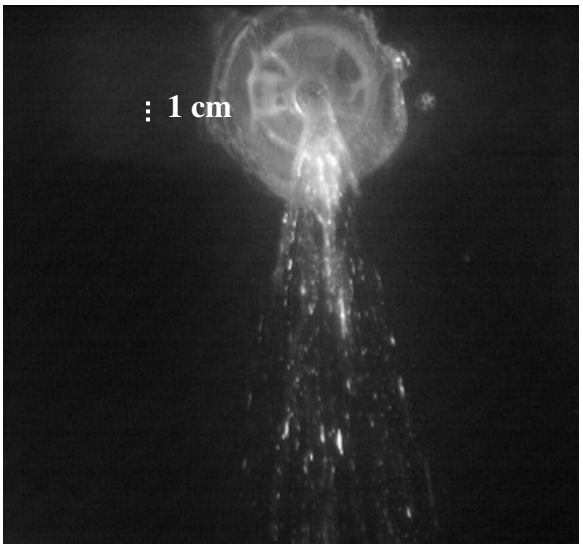


Figure 4.11 View of the jet spray for q = 18.8, We = 15.85.

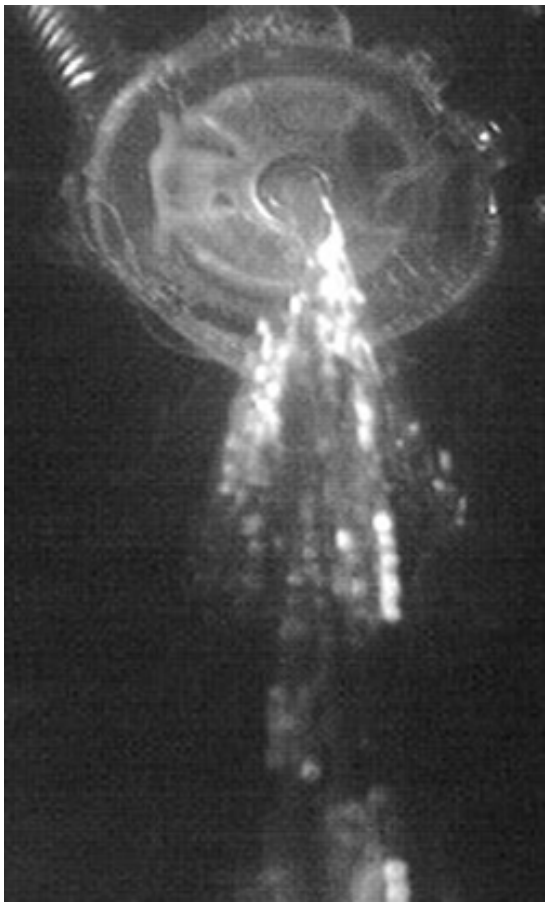


Figure 4.12 View of the jet spray for q = 40.7, We = 7.32.

Comparing all three images shows that the break up process seen in figure 4.12 is completely different from those seen in figures 4.10 and 4.11. For q = 40.7, large "ligaments" of liquid break off the jet and "explode" outward spreading in a linear fashion. The ligaments are stretched in the direction of the cross flow. This was first observed by Fuller etl al. (1997). For q = 10, and 18.8, the images show the liquid being "sheared" off the sides of the jet spreading the droplets outward in a linear fashion as well. The width of the spray for q = 18.8, seems to be wider with a less dense spray core, when compared to q = 10.

To further understand how the jet spreads at various downstream locations, measurements were made of the spray core for q = 10, and 18.8. A scaled image was used to determine the magnification of the image which was in turn used to determine the actual sizes in 20 consecutive images. The measurement averages were used with a maximum standard deviation of only 6% of the averages.

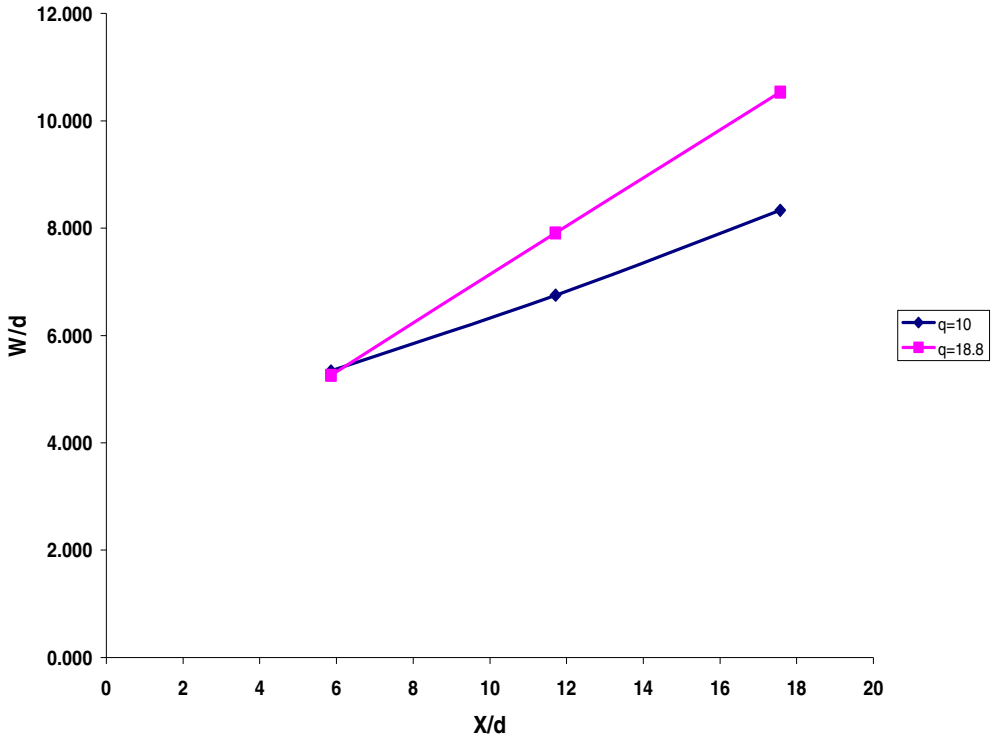


Figure 4.13 Non-dimensional spray width at various downstream locations.

Figure 4.13 shows that for both momentum fluxes, the width of the jet was comparable at 5 diameters downstream of the center of the jet. This result is in agreement with those of Fuller et al. (1997) and Aalburg et al. (2004) who found that

independent of the momentum ratio and Weber number, the downstream break up location was constant at 8 diameters downstream of the jet. At downstream locations of 12 and 17.5 diameters, the width of the spray seems to grow linearly, however it is dependent on the momentum flux value. For the higher momentum flux, the spray becomes wider than that for the lower momentum flux. This is confirmed when looking at figures 4.10 and 4.11. However, for both cases it seems that the jet is "flattened" out by the cross flow, causing the jet to spread linearly in the Y-direction. It would make sense then that at higher cross flow values (lower q), the jet would spread more in the transverse direction. Figure 4.13, however, shows the opposite trend.

The discrepancy is due to the method of measurement. The purely qualitative nature of simply measuring the spray core is the cause of this error. In reality, the spray extends much further outward into the dark regions of the images used for this analysis. The size of the droplets does not allow for a large amount of light to be reflected from these drops preventing them from showing up on the images. At the lower momentum flux, more droplets are being sheared from the sides of the jet, at smaller Sauter Mean Diameters (SMD), which would give the impression that the spray width is in fact smaller than the width found in the higher momentum ratio image.

The findings of Madabhushi (2003), both experimentally and computationally, showed that the droplets along the width of the spray extended nearly 60 diameters in each direction. The findings, however, did show that a well-defined spray core did

exist within 10 diameters in each direction. The light is reflected readily from this region, thus allowing it to show up in the images used for this analysis. For this reason, the measurements made are purely qualitative, and should only help define the various trends seen in the interaction between the cross flow and the jet.

Using the trends seen in the results, a fairly good approximation of the bending process of the jet may be determined. Inspection of figures 4.10, and 4.11, shows the cross flow momentum "flattening" the upstream side of the jet causing it to expand outward in the y-direction.

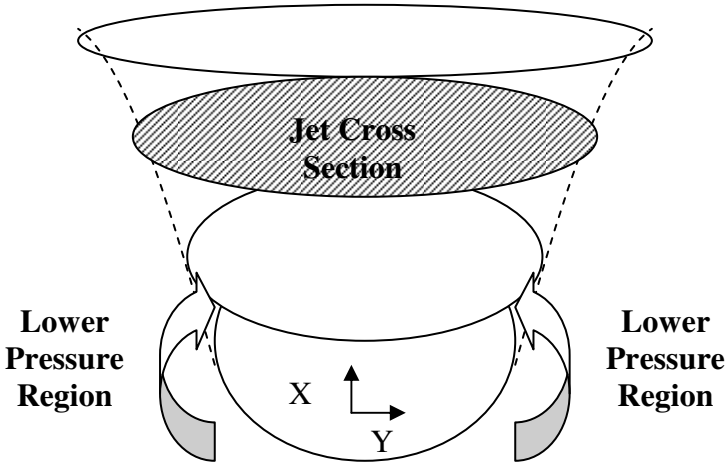


Figure 4.14 Display of change in the cross section of the jet at various downstream locations.

As previous researchers have shown, the drag on the jet is very similar to that of a solid cylinder of equivalent diameter. This drag bends the jet in the downstream direction causing the cross section of the jet to change from a circle to an ellipsoidal

shape, before the break off point. Coupled with the lower pressure along the sides of the jet the "stretching" in the transverse direction becomes more pronounced. Whether or not this "stretching" process is steady or unsteady is yet to be determined, however, any unsteadiness may significantly contribute to the surface waves seen in figure 4.4.

4.1.4 PIV Cross Sectional Velocity Map

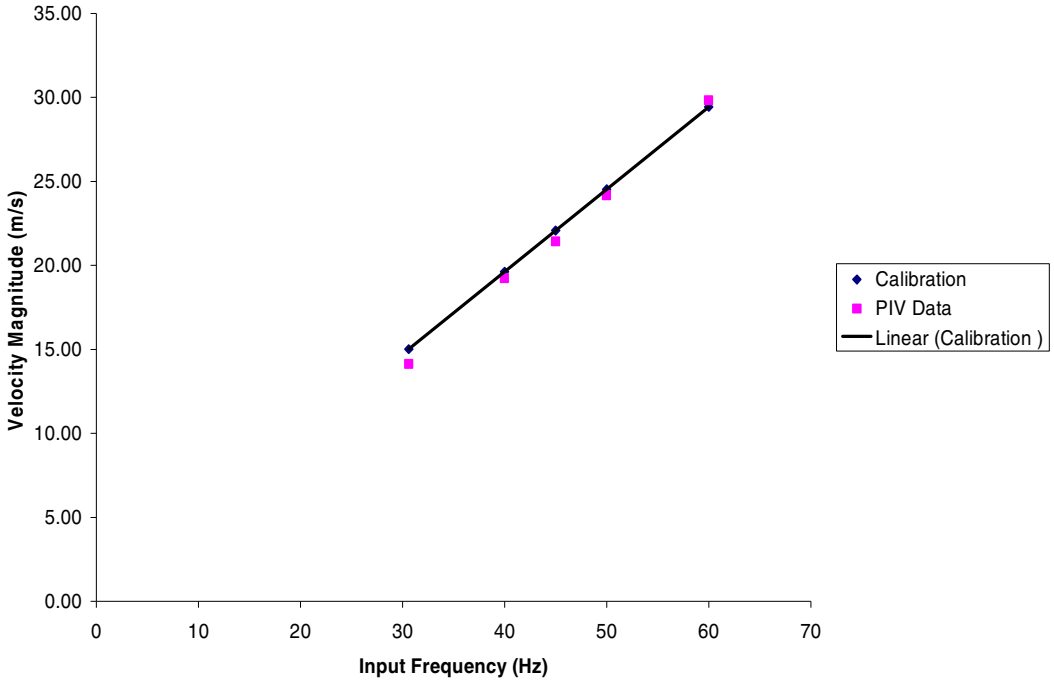


Figure 4.15 Wind tunnel velocity validation using PIV.

Figure 4.15 shows that the PIV data from the mean field in the cross section very closely resembles the data given from the previous calibration in figure 2.4. The maximum difference between calibration and measured data using the PIV is only 5%. The validation not only shows that the calibration used is accurate, but it also indicates that the methodology used for the PIV is correct as well. In addition to validating the cross sectional velocities, the PIV mapped the velocity profile across the cross diameter of the test section (figure 4.16).

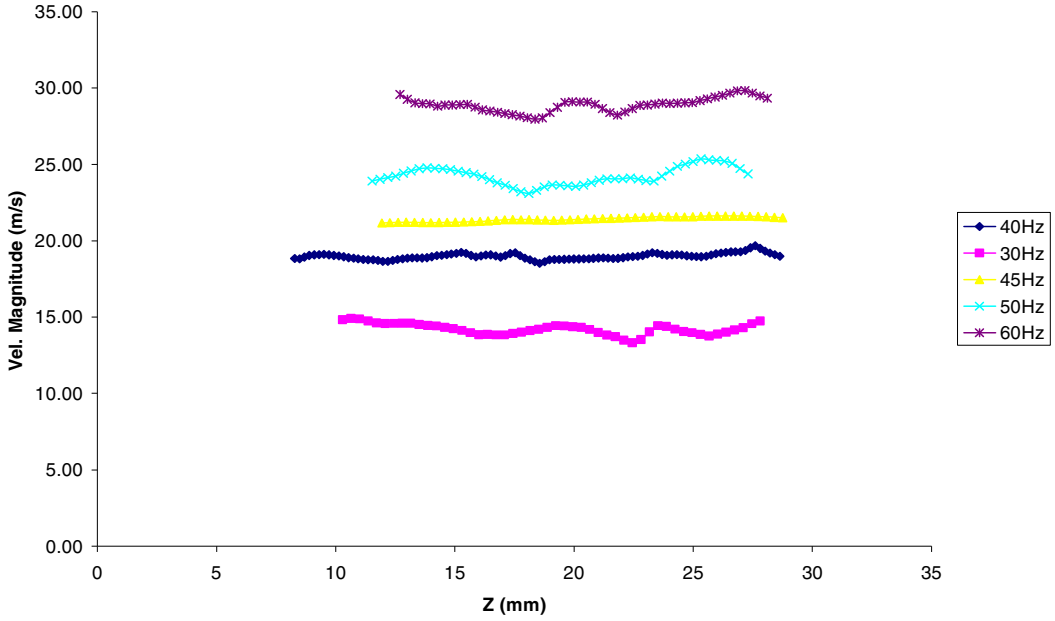


Figure 4.16 Wind tunnel velocity in the cross section of the wind tunnel using PIV.

Figure 4.16 shows a very even velocity profile along the centerline of the wind tunnel. At higher wind tunnel frequency (cross sectional velocity) the profile

becomes somewhat erratic, but well within acceptable limits for this study. This result is important in showing that any disturbance in the jet is primarily due to the interaction of the two fluid streams.

4.1.5 Axial PIV Results for JICF

Using the mixture of laser fluorescent powder and water for cross flow tagging, the interaction between the gaseous high speed cross flow and water jet can be investigated further. It was shown in section 4.1.4 that the cross flow of air was uniform and somewhat stable, with the proper output velocity as a function of indicated velocity. The initial test plane for the PIV system was aligned with the axial plane of the water jet (Figure 4.17).

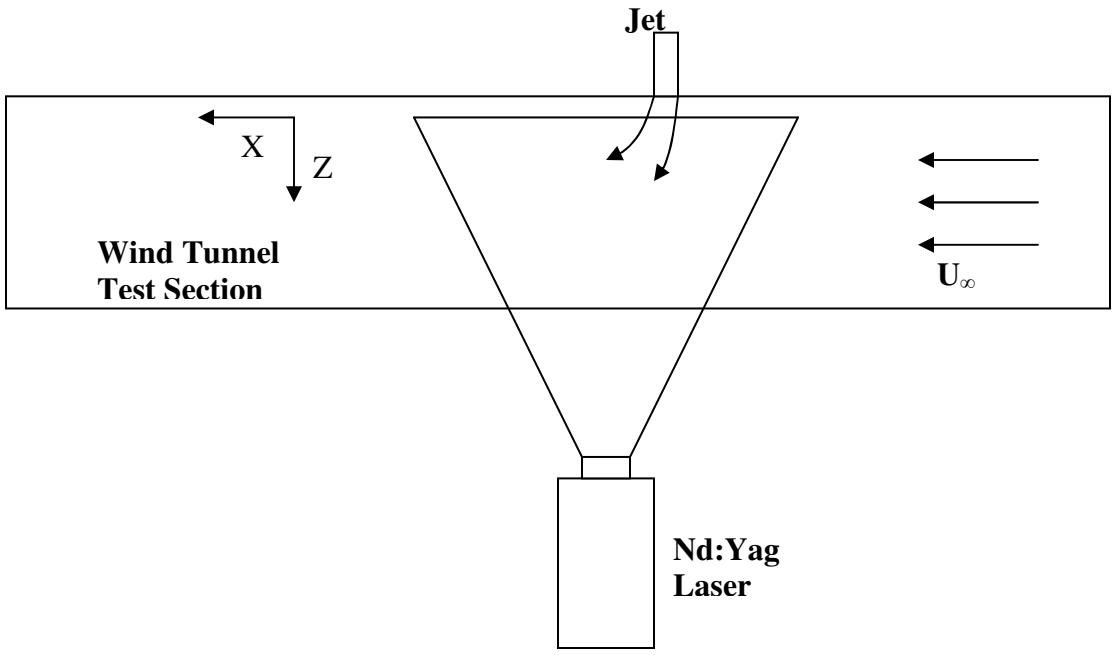


Figure 4.17 PIV measurement plane for all axial locations.

Measurements in the X-Z plane were made at various spanwise locations ranging from Y/d = 0, 2, and 4. All images were collected using the methodology explained previously, and post processed with no interpolation. By not performing any interpolation of the data, no false information is shown. However, there appears to be holes in the velocity field due to the highly three-dimensional nature of the flow field. Due to the dissipation of flow seeding, at least 100 successive images were needed to get an average flow field.

Instantaneous resulting images were lacking in data density. Each set of successive 100 images was repeated under the exact some conditions to get a sense of the variance in the velocity field from image set to image set. The variance was found to range from 4%-6% throughout the entire flow field. This is more than appropriate for this study, and from this point forward each average velocity field is assumed to be "fully imaged" with no significant variation occurring with the inclusion of more image sets.

For the first momentum ratio of q = 172, the jet has a very little bend due to the low speed cross flow (figure 4.3a). The imaging plane is in the X-Z plane at a spanwise location of Y/d=0. With very little dissipation of the seeding particles, a full velocity field was obtained showing the low speed cross flow moving around the body of the liquid jet issuing downward. All vector fields for each momentum ratio have the same color scaling to show any variations in velocity magnitude.

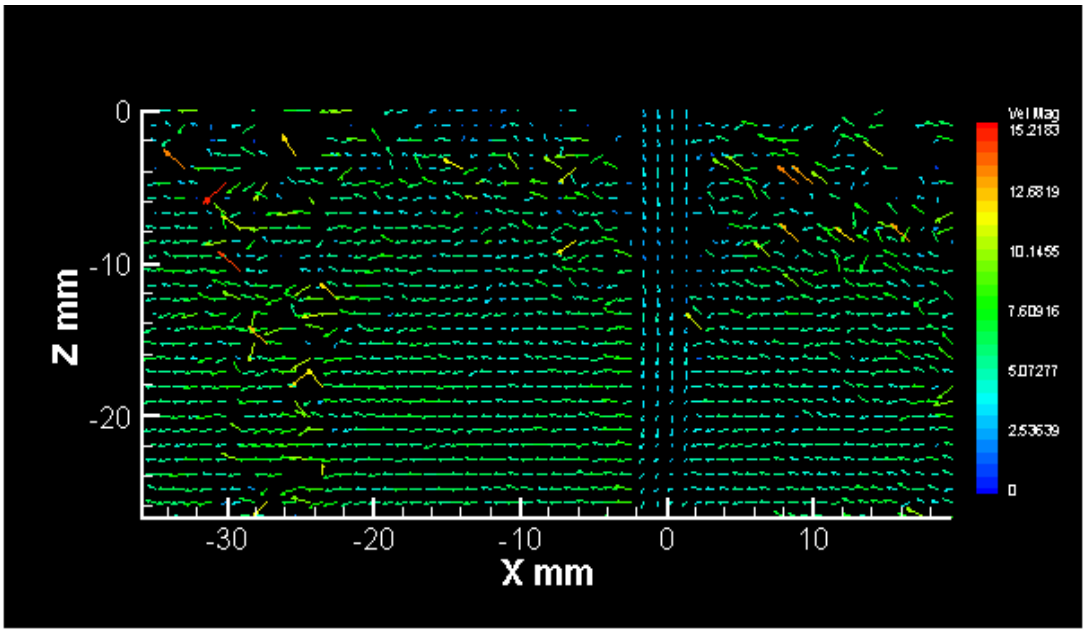


Figure 4.18 PIV vector field for q=172 at Y/d=0.

Figure 4.18 shows a vector field with a high density of seeding particles near the central region of the image. The vectors at the interaction point between the jet and the cross flow show a very straight directionality with no seeding particles showing up in the body of the water jet. At the rear boundary of the jet there appears to be a slight acceleration of the cross flow with a high velocity magnitude with is then decelerated to the initial cross flow velocity. It appears that the cross flow is in fact moving around the body of the jet and being slightly accelerated by the jet boundary, as shown in figure 4.14.

To further validate this assumption, measurements were taken at spanwise locations of Y/d = 2, and 4.

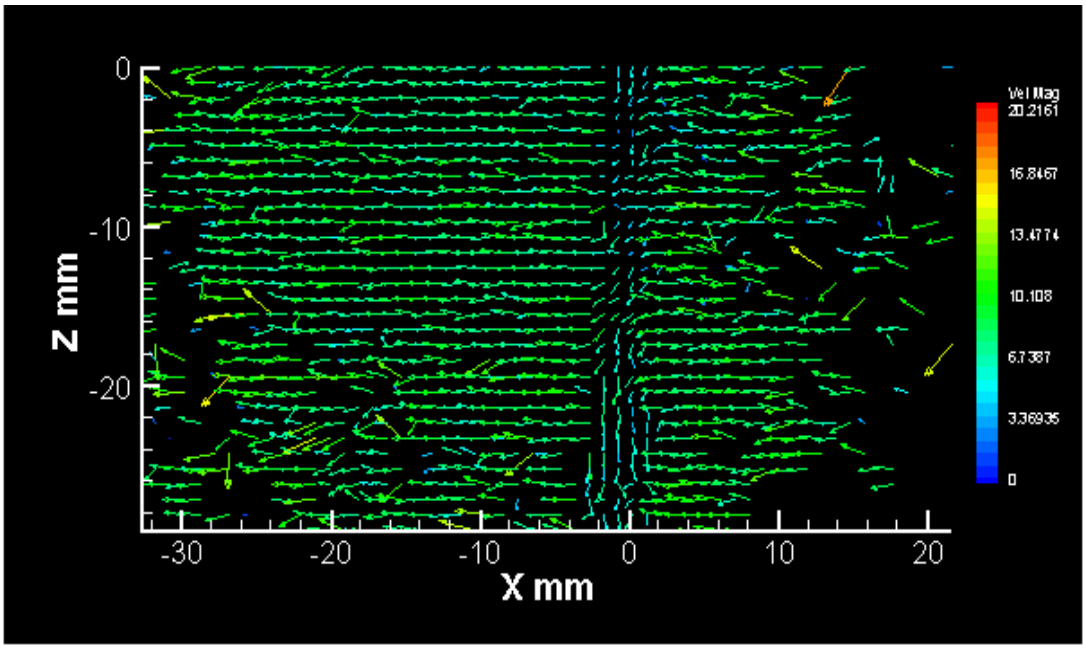


Figure 4.19 PIV vector field for q=172 at Y/d=2.

Figure 4.19 shows that the vectors are very straight along the upstream boundary of the jet, with some cross flow velocity vectors in the jet body. Due to the averaging of the velocity field, some of the vectors within the boundaries of the jet are shown to be a combination of the cross flow velocity in the X direction and the jet velocity in the Z direction. In fact, instantaneous images show that these vectors are along the direction of the cross flow.

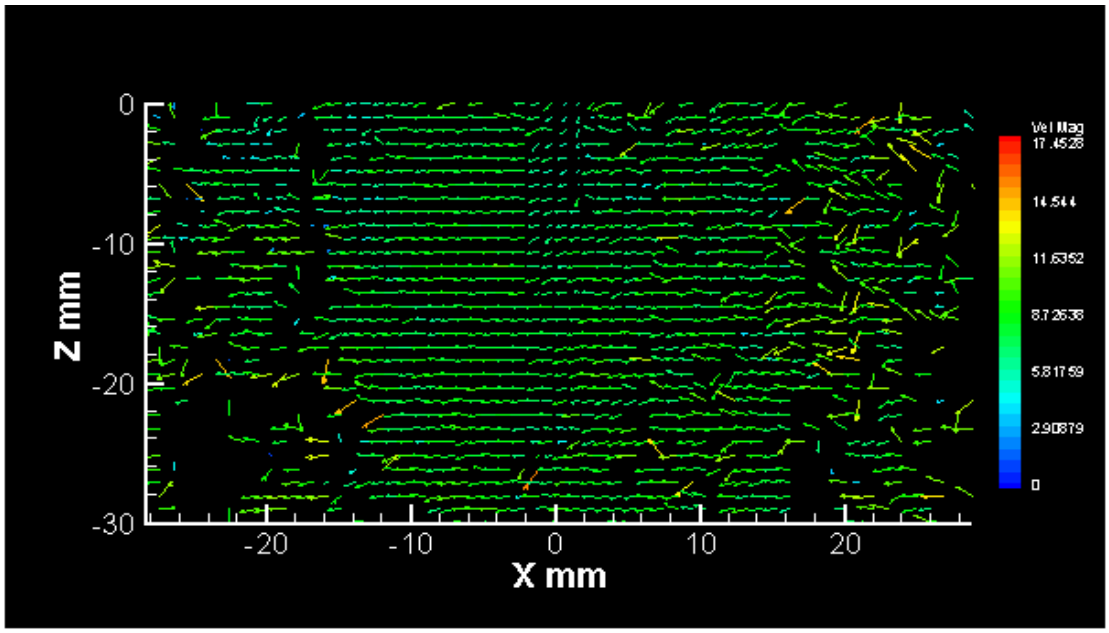


Figure 4.20 PIV vector field for q =172 at Y/d = 4.

Figure 4.20 shows a much better vector map at a larger spanwise location of 4 diameters from the center of the jet. Almost all information on the water jet is lost by the cross flow wrapping around the boundary of the jet. At 4 diameters from the jet boundary the seeding particles have moved around the column, and show up as velocity vectors equal in magnitude to the cross flow velocity. No appreciable acceleration is noticed in the vector field, however, it very well could be contained somewhere between the spanwise locations of 2 and 4 diameters. The complexity arises when analyzing the flow data in the exact boundary between the two flow regimes. Data is either lost, not present, or the actual droplets used for seeding coalesce with the water jet. The best indication of any acceleration may be seen in the X-Y plane, which will be shown later on.

For the second momentum ratio of 69.25, similar PIV velocity fields were obtained. The results show the jet bending more in the downstream direction.

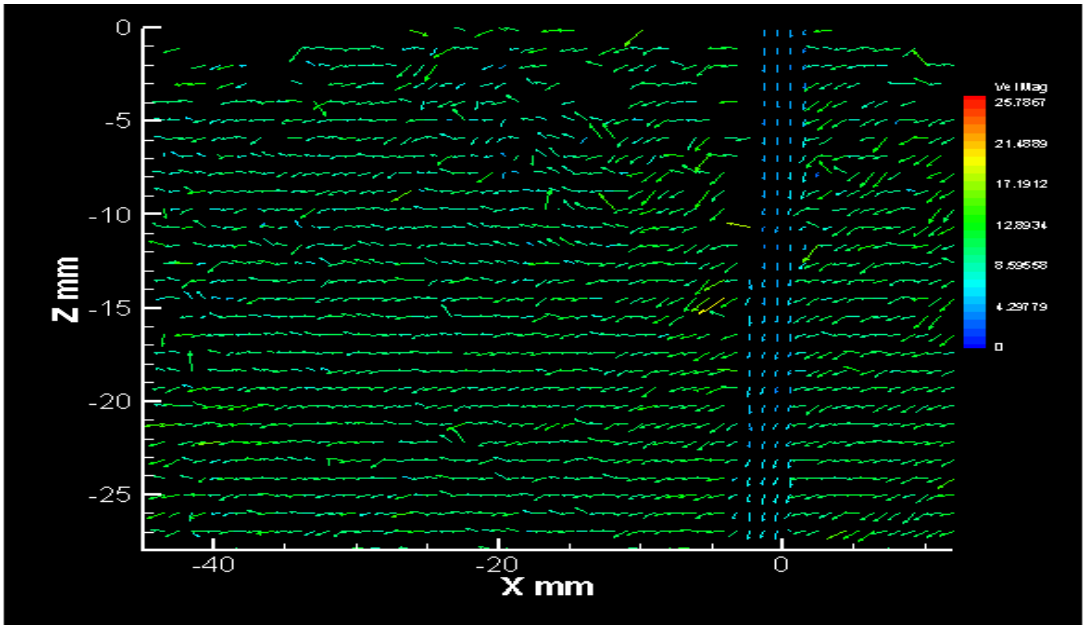


Figure 4.21 PIV vector field for q=69 at Y/d=0.

For this momentum ratio, the jet shows further bending with the cross flow moving around the body of the jet. At the downstream boundary of the jet, along the upper boundary, there appears to be a distinct lack of cross flow vectors. This region shows lost information not only along the boundary, but also at several downstream locations. The source of this error could be from the cross flow moving in and out of the laser light sheet, causing the information to be lost or removed as erroneous data. This observation further supports the idea that the cross flow is in fact moving around the jet and not being pushed downward in the axial direction of the jet. Also, the

presence of downstream locations showing a somewhat periodic loss of information could indicate the presence of some instabilities in the cross flow due to vortex shedding or separation of the cross flow. Again, more information is required and will be obtained when the plane of the laser light sheet is moved into the X-Y plane. Again, the plane of measurements was moved to a spanwise location of 2 diameters to see if any differences are seen.

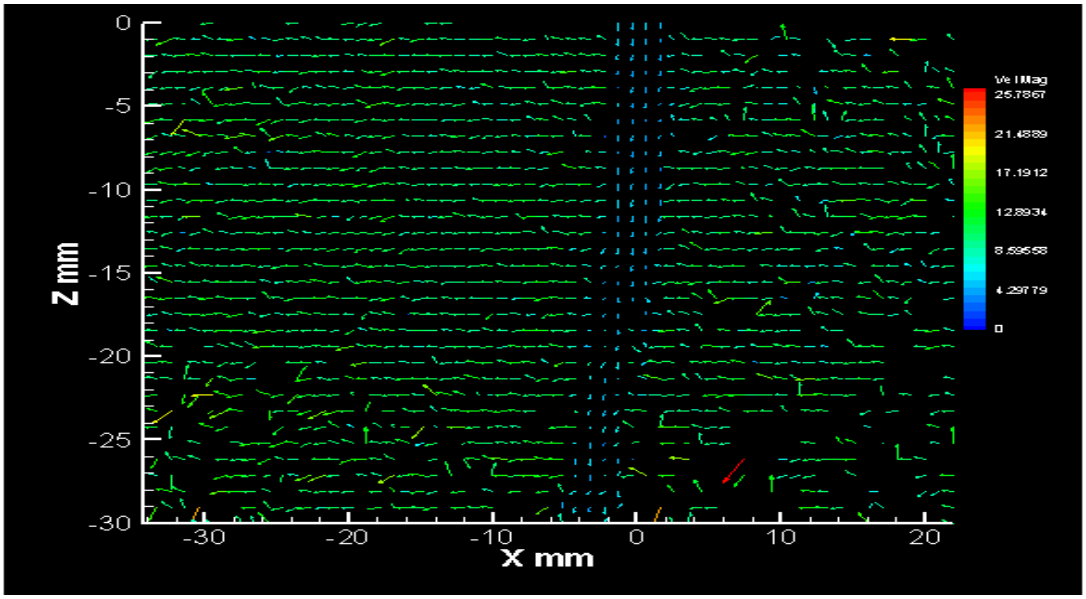


Figure 4.22 PIV vector field for q = 69 at Y/d=2.

Figure 4.22 immediately shows that any lost data at the downstream boundary of the jet is recovered at 2 diameters in the spanwise direction. This further supports the idea that at the very central region, downstream of the jet, there appears to be some instability due to the cross flow moving rapidly around the body of the jet.

For q = 40 (figure 4.23), many similar trends, such as those in previous momentum ratios, are observed.

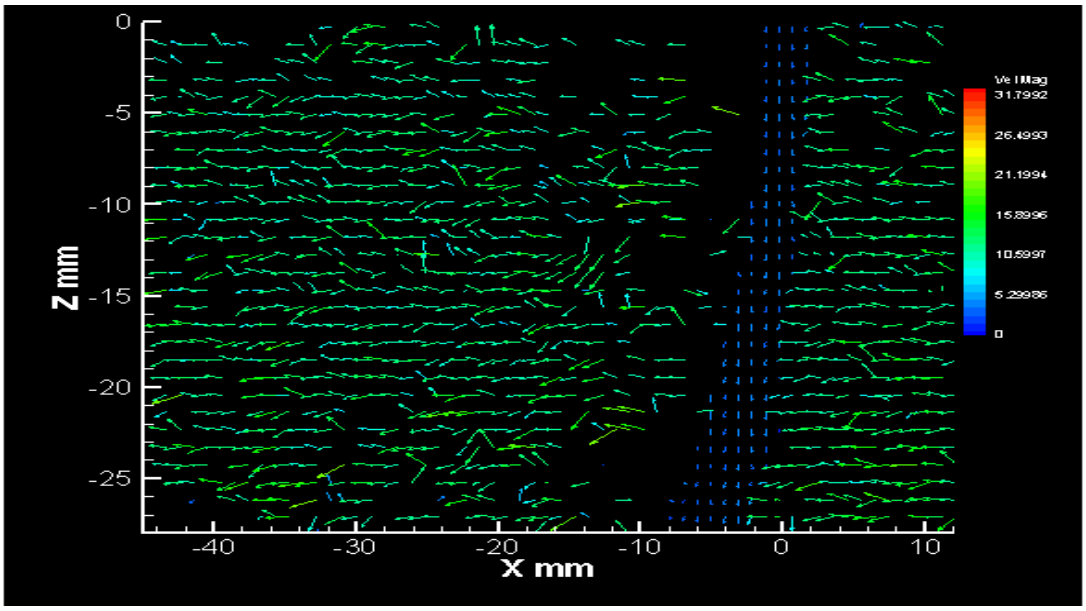


Figure 4.23 PIV vector field for q=40 at Y/d=0.

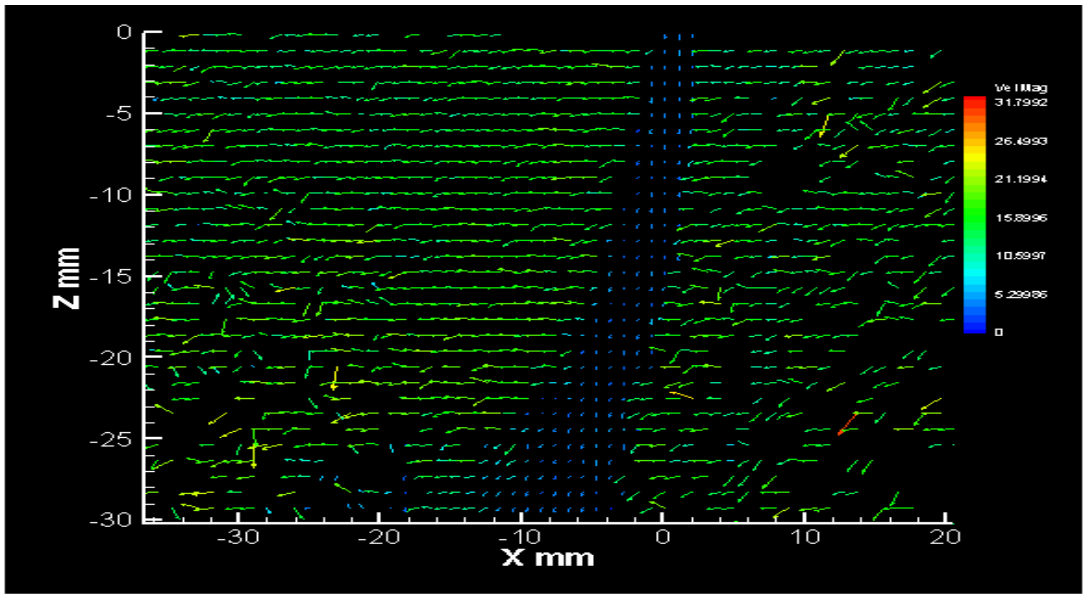


Figure 4.24 PIV vector field for q=40 at Y/d=2.

Figures 4.23, and 4.24 each show a liquid jet bending in the downstream direction with straight velocity vectors along the upstream boundary of the jet. With the measurement plane at the center of the jet (Y/d=0), again there appears to be a distinct loss of flow information in the downstream side of the jet with some periodicity. When the plane is moved to 2 diameters, the information is regained and the velocity plots show very straight velocity vectors with no periodicity. Even at a higher cross flow velocity, the flow appears to continue to move around the body of the jet resulting in lost information at the central downstream location of the flow field.

For q = 18.8, the jet bends in the downstream direction with straight cross flow velocity vectors passing around the body of the jet.

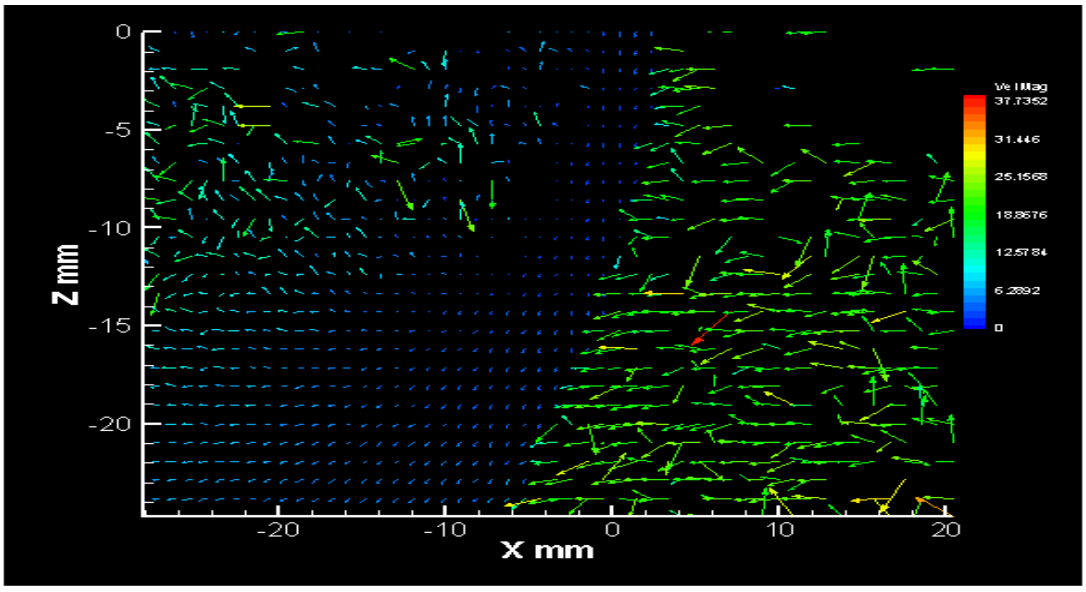


Figure 4.25 PIV vector field for q=18.8 at Y/d=0.

Similar to the cases of previous momentum ratios, there appears to be a highly turbulent structure in the downstream wake of the jet. This conclusion is reached by observing the velocity vectors at the rear of the jet which show a very random directionality. The droplets from the jet begin mixing and accelerating as they move downstream. By observed the differences in the length and direction of the vectors it is seen that the sheared droplets in the wake of the jet accelerate as they move downstream as well as change direction. When comparing this cross sectional slice with one from a spanwise location of 2 diameters it is observed that any turbulent structures present in the central slice are now removed due to the steady nature of the flow wrapping around the jet.

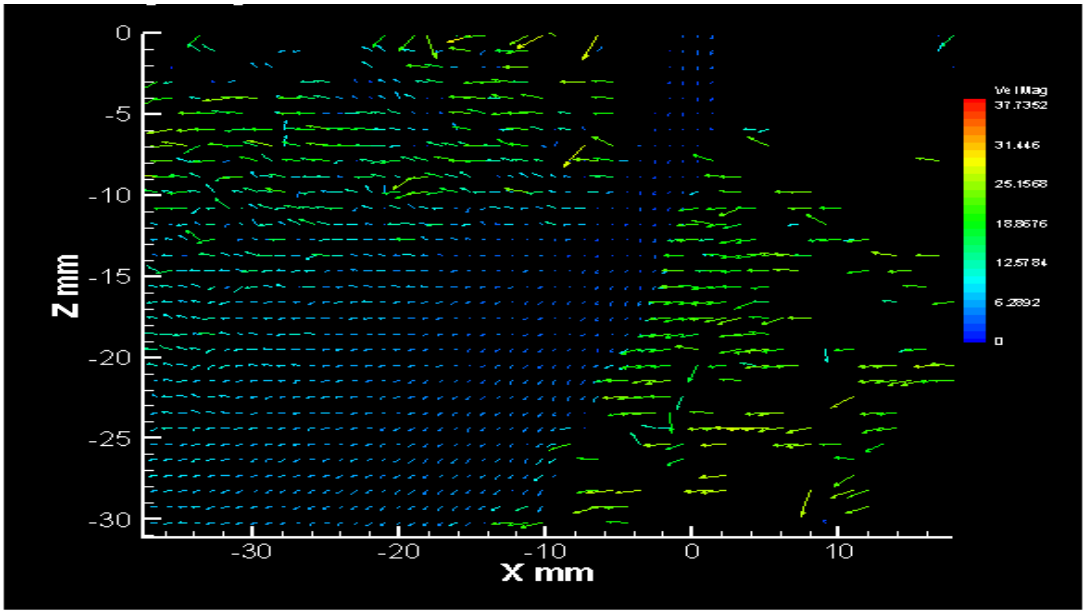


Figure 4.26 PIV vector field for q=18.8 at Y/d=2.

Figure 4.26 shows a distinct instability wave along the upstream boundary of the jet with straight cross flow velocity vectors. On the downstream side of the jet the flow appears to recover and regain its flow directionality.

At the highest cross flow velocity, lowest momentum ratio; q=10, much of the downstream information on the cross flow is lost in high rate of droplet shear occurring along the rear of the jet. The velocity magnitudes indicate that droplets are being shearing off the sides of the jet and accelerating as they move downstream.

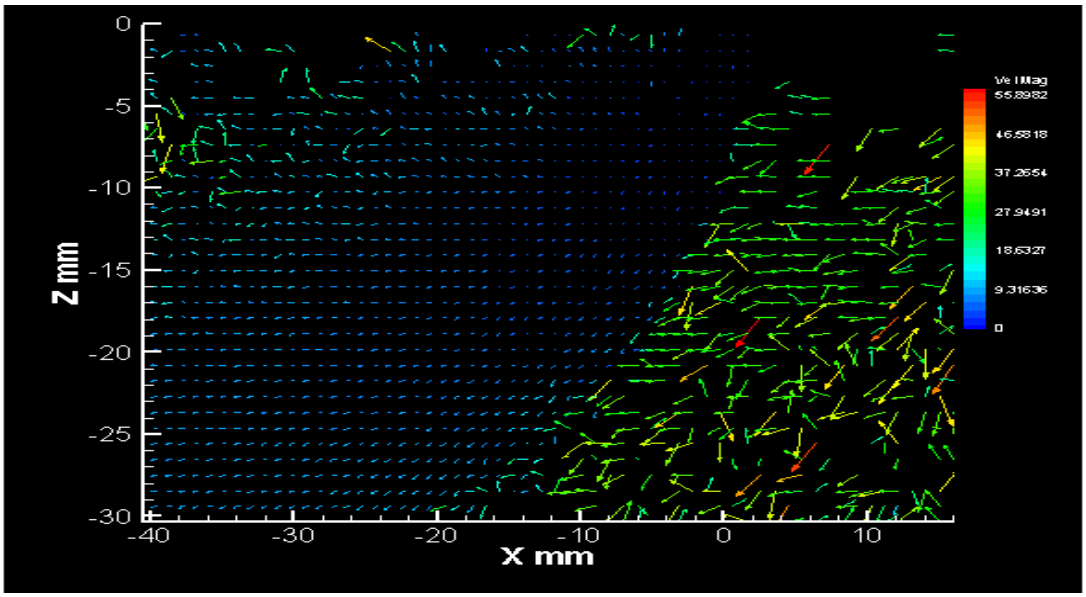


Figure 4.27 PIV vector field for q=10 at Y/d=0.

There still appears to be somewhat of a periodic loss of information on the downstream side of the jet. A close inspection of these vectors shows that the directionality is highly random. This could be due to eddy formation in the wake of the jet. Further analysis needs to be done in the X-Y plane to determine if these eddys are present.

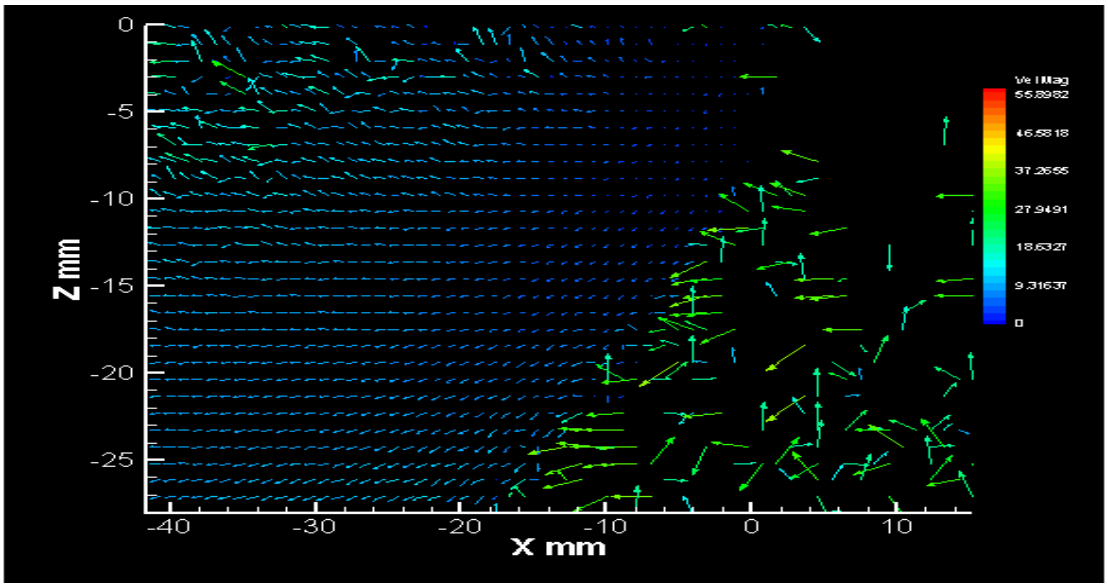


Figure 4.28 PIV vector field for q=10 at Y/d=2.

At 2 diameters, in the spanwise direction, the cross flow remains straight with some periodicity in the downstream wake. Figure 4.28 was averaged over 200 images producing a low number of velocity vectors in the upstream side of the JICF. This was primarily due to seeding dissipation, and evaporation at a high speed cross flow velocity of 30 m/s. Also, much of the seeding gets moved around the body of the jet and is subsequently lost in the violent shearing of droplets along the sides and the rear of the jet. In summary, the X-Z plane gives plenty of information on the mechanism of the jet break up. The cross flow vectors are straight along the upstream boundary of the jet indicating a mechanism whereby, the air is moved around the body of the jet possibly contributing to the instability leading to jet break up. As the vectors pass around the jet and meet in the central downstream side, periodic loss of flow information is observed in the wake. This loss of information could indicate an

eddy structure rotating and "pushing out" any seed particles due to centrifugal force present on these particles.

Lecuona et. Al (2002) came to a similar conclusion showing that strong vortices resulted in a significant depletion of particle concentrations 1 second after the onset of vorticity. These "holes" on the data may be markers of strong vorticity in the flow, which may aid in the mixing of sheared jet droplets and seeding particles. This result indicates the origin of the disturbances may not be the Rayleigh-Taylor instability. As explained previously, these instability waves directly affect the break up of the jet. An understanding of the instability mechanism is needed to better control the atomization by the gaseous cross flow. The next step is to take velocity field measurements in the X-Y plane at a single Z location (Z/d=10) to see if any support may be given to these primary findings.

4.1.6 Spanwise JICF Results

Axial measurements in the X-Z plane showed the cross flow and its interaction with the water jet boundary. The PIV vector fields indicated that the air did not follow the curvature of the jet, but simply passed around the body of the jet with some lost information in the very near field downstream of the jet. To better understand the interaction between the cross flow and the jet boundary, PIV measurements were taken in the X-Y plane at a non-dimensional distance of 10 diameters from the wall. This location was chosen to allow for measurements to be made outside of any boundary layer that may exist at the wall of the test section.

Also, inside the boundary layer, the three- dimensional nature of the flow resulted in many seeding particles moving through the thickness of the light sheet, which flooded the vector field with erroneous data. With this in mind, measurements were limited to within 10 diameters from the wall due to the lack of flow seeding further from the wall.

While measuring the velocity fields of the free stream only, it was noticed that the wind tunnel had fallen out of calibration. For this reason, the momentum ratios were adjusted to reflect the change in free stream velocity for the spanwise measurements. Instead of momentum ratios of q = 69 and 40 with free stream velocities of 11.5 and 15 m/s, respectively, the momentum ratios were changed to reflect the new free stream velocities (Table 4.2)

Table 4. 2 Adjusted momentum ratio's for re-calibrated free stream velocities.

$U_{\infty old}$ (m/s)	$U_{\infty new}$ (m/s)	q_{old} (momentum ratio)	q_{new} (momentum ratio)	Weber Number (new)
11.50	10.50	69.25	77.89	3.58
15	14	40.70	43.81	6.37

Spanwise measurements in the X-Y plane were limited to these two momentum ratios due to liquid droplet congregation on the walls of the test section. In order for the PIV system to track the seeding, a dark background must be present. At higher cross flow velocities, the liquid jet was bent more severely depositing large amounts of liquid droplets on the surface of the wind tunnel. The deposition of sheared jet droplets resulted in spurious vectors showing up in the background of the image, preventing any measurements of accurate velocity fields to be obtained. For this reason, only two momentum ratios allowed for deposition free measurements, and these will be the main focus of this section.

At both momentum ratios, repeatability and image independence studies were conducted. Both sets of results showed great repeatability to within 3% deviation from day to day, while all vector fields were shown to be image capture independent after 200 images to within 3% deviation as well. Low seeding in the flow field prohibited any instantaneous flow fields from being captured. Each instantaneous image only provided a few good vectors, making it necessary to average multiple consecutive images to obtain an entire flow field. To ensure that all image fields were completely converged, 300 images were collected and average velocity fields were calculated.

For the first momentum ratio of 77.89, the curvature of the jet is very similar to that seen in figures 4.18 and 4.19 from the previous section. This allowed for measurements to be made with little to no deposition of either seeding particles or liquid droplets from the jet. The direction of the free stream vectors are in the

streamwise X direction and should help to picture the proper orientation of the flow field. In essence these measurements are made as a cross sectional "slice" of the X-Y plane.

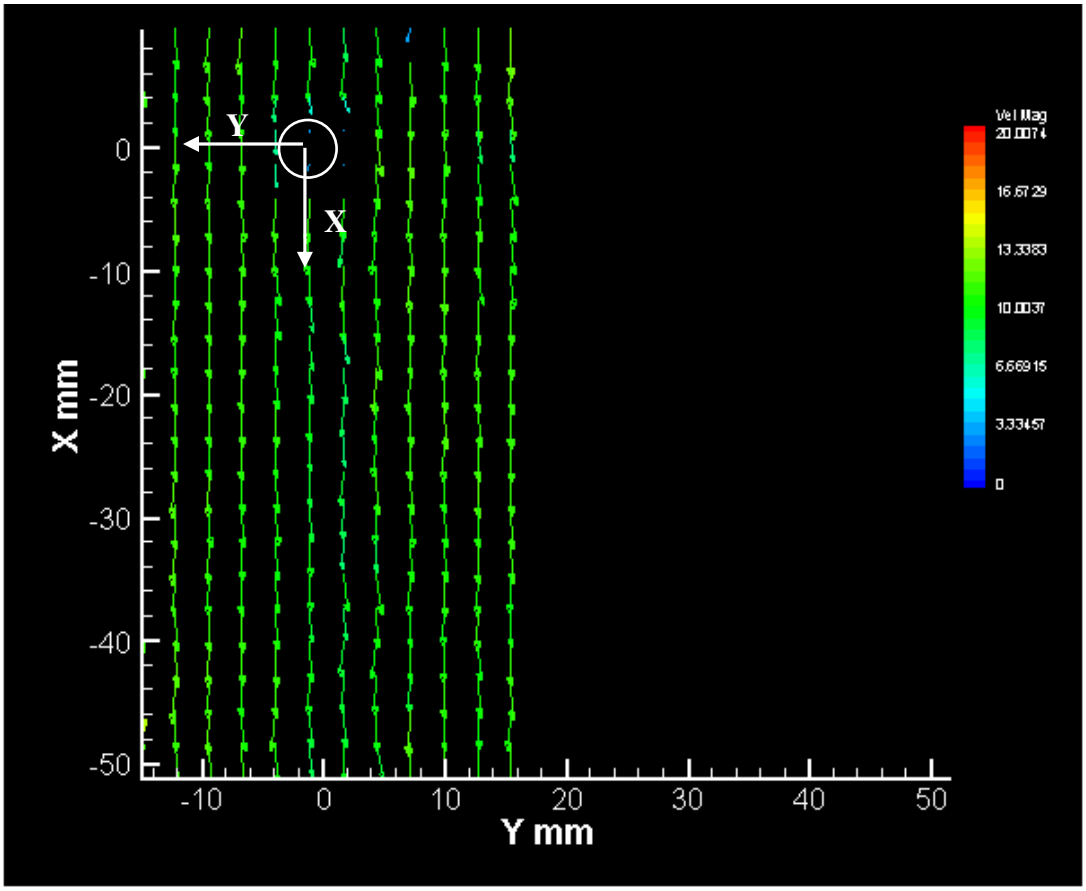


Figure 4.29 PIV vector field for q=77.89 at Z/d=10.

Figure 4.29 shows a vector map of the free stream flow as it interacts with the liquid jet. To aid in the image, an approximate location of the jet outlet is provided. Any free stream vectors within the downstream width of the jet are "blocked out" by the liquid column as it is bent downstream. The free stream vectors seem to be relatively oriented in the downstream direction with very small changes in velocity

magnitude. Due to interference form the injector, no vectors were collected in the very near field of the jet. It should be noted that this is an average field, and any periodicity or instability would not show up in this figure. As stated previously, limitations due to seeding density did not allow for any analysis of instantaneous vector fields which would have yielded much more useful information.

For q = 43.81, similar results were obtained. The vector field is very straight, with a change in the free stream magnitude. For the lower momentum ratio, the jet spreads more in the spanwise direction, further limiting any downstream observations that may be made (as seen in section 4.1.3).

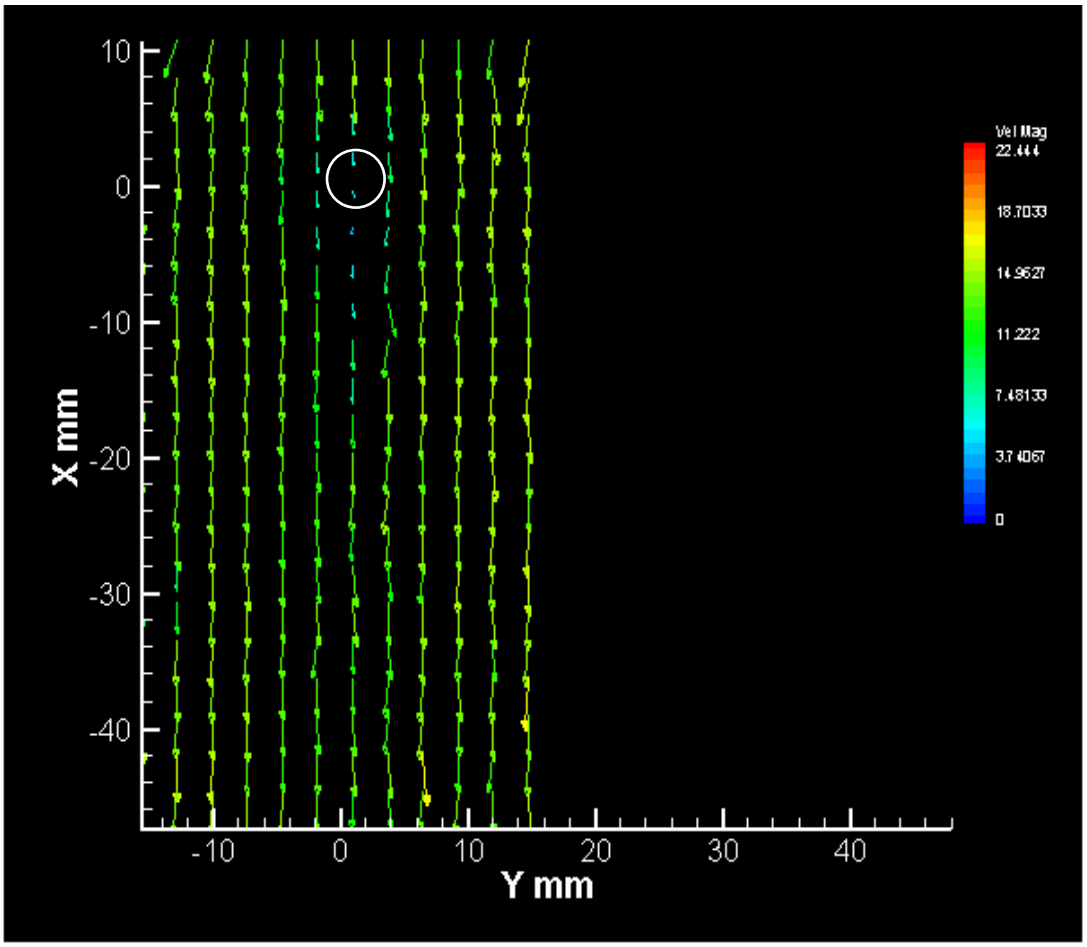


Figure 4.30 PIV vector field for q=43.81 at Z/d=10.

Both velocity vector fields show a distinct orientation to the cross flow downstream. Any motion through the thickness of the light sheet would result in erroneous vectors that would show up as very low velocities. These vector fields did not show this tendency, therefore it can be surmised that most the flow is oriented in the downstream direction. This further supports the idea that no free stream air is following the jet column as it is bent downstream. The air is simply moving around the body of the jet and interacting with the liquid boundary.

To better understand the nature of this interaction, several rakes were placed in the near field of the jet at various spanwise locations of Y/d from the side of the jet. The velocity magnitudes were non-dimensionalized by the mean velocity of the free stream air. Downstream X/d locations were taken from the center of the jet with negative X/d values being the upstream locations and positive X/d locations being downstream.

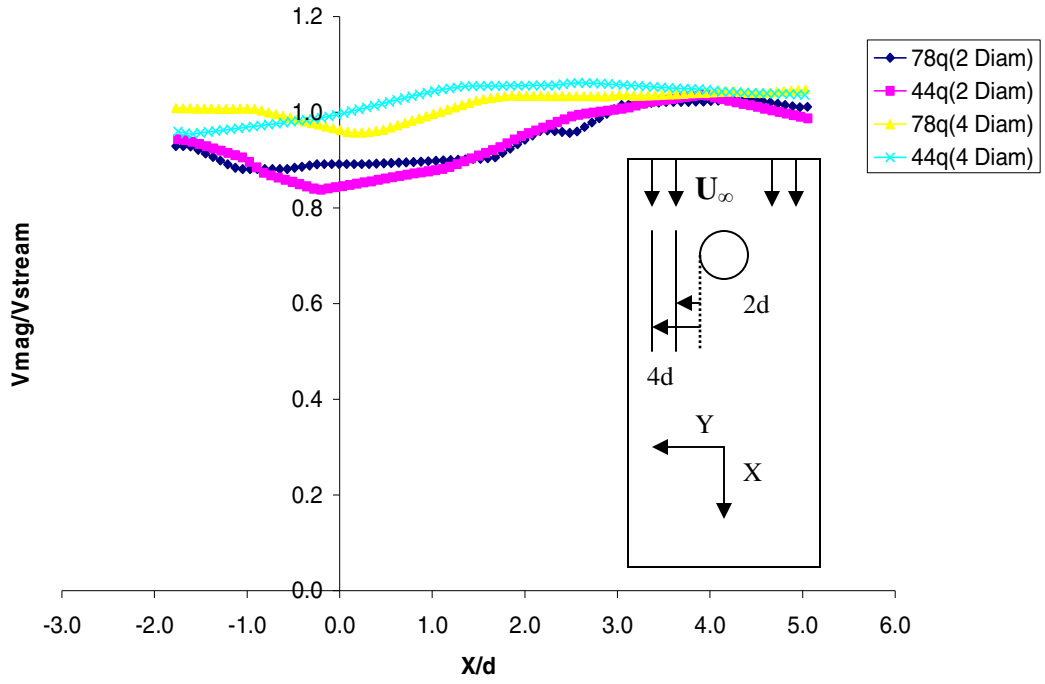


Figure 4.31 Near field velocity profiles at Z/d=10.

Figure 4.31 sheds more light into the mechanisms of the interactions between the jet and the cross flow. Both momentum ratios show about a 20% reduction in

velocity magnitude 2 diameters from the side of the jet. When comparing the two momentum ratios it is observed that the lower momentum ratio (higher cross flow velocity) has a more significant reduction in velocity magnitude than the higher momentum ratio, at the same spanwise location. The width of the defect for the higher q seems to be larger, while the magnitude of the defect for q = 44 is larger.

At 4 diameters, both momentum ratios show a small recovery to values closer to the free stream velocity, while still showing some remnants of the jet boundary effects. Both spanwise locations show a near full recovery towards the free stream velocity around 3 diameters downstream of the jet. Due to the geometry of the setup, no wake deficit measurements could be made at the rear of the jet column. The side velocity profiles, however, provide more than enough information to infer that there is a significant velocity defect at the rear of the jet. Any effects that may be observed in the near field of the jet are obviously felt through the entire flow field.

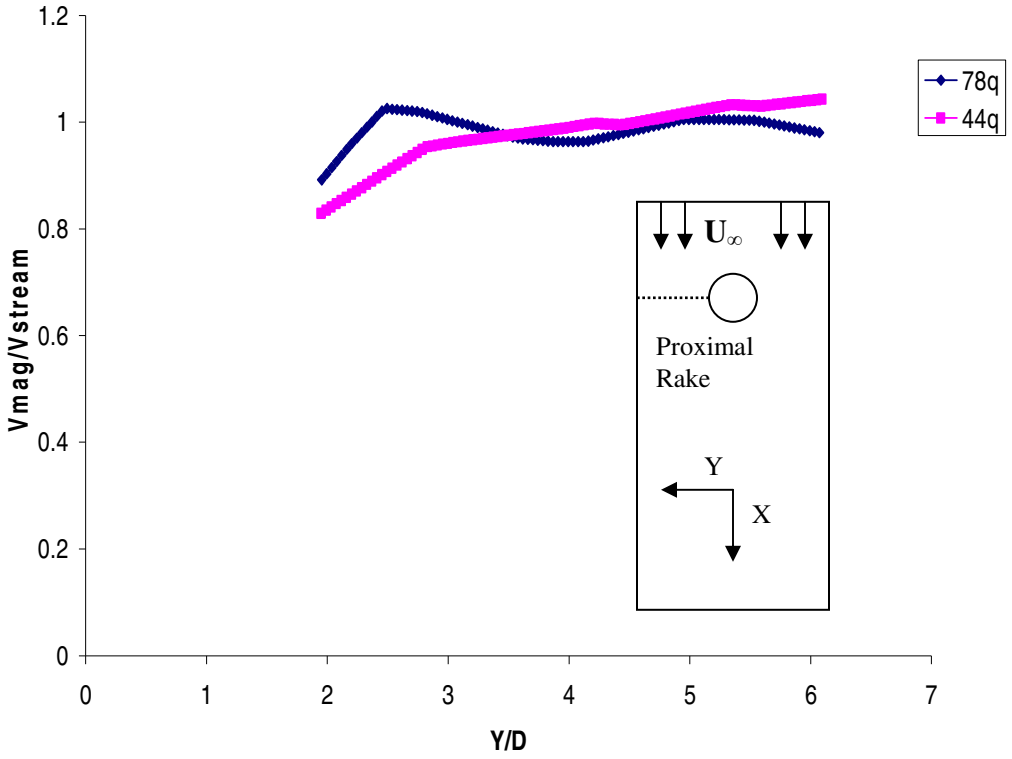


Figure 4.32 Proximal velocity profiles at Z/d=10.

Figure 4.32 shows the velocity profiles of the boundary layer velocities along the side of the jet. Measurements could only be taken up to Y/d=2, but it is clearly seen that both momentum ratios also experience a velocity defect near the sides of the jet. The lower momentum value has a much more intense velocity defect than the higher momentum ratio. This is in good agreement to the findings seen in Figure 4.31.

The explanation of this velocity defect sheds some insight into the break up mechanism of the two-phase JICF. The observed velocity defect is due to a region of

intense shear at the boundary of the liquid jet and the cross flow. This intense shear is only magnified as the free stream velocity is increased, thus resulting in a larger velocity defect for lower values of q. This shear results in the removal of droplets from the jet surface, and the "stretching" of the liquid column in the spanwise direction along the sides of the jet. Coupled with the extremely high drag on the front of the jet, the jet expands in the spanwise direction, and begins to break apart.

The stripped droplets from the side of the jet are carried off by the cross flow following its streamlines and being carried to the rear of the jet. This explains the increased deposition of jet liquid droplets along the side walls of the test section (Figures 4.5 a, b, and c). The droplets that are sheared from the sides of the jet are very small which allows them to be "dragged" through the free stream at a much higher velocity than the larger droplets. This is complimentary to the findings of Fuller et Al. (1998) who were able to show that along the sides of the jet there exist droplets moving at much higher velocities than those near the center of the jet. Also, they were able to show that the Sauter Mean Diameter (SMD) of these droplets was much smaller than those in the central region as well.

Thus, the overall break up mechanism can be attributed to the high shear forces along the sides of the jet, as well as the intense drag on the front of the jet due to its shape. As the cross flow comes into contact with the jet it imparts a high drag force on the front of the jet, which has a much higher density than the cross flow. The air then passes around the jet losing nearly 20% of free stream magnitude 2 diameters away from the jet boundary, resulting in an intense shear region along the

sides of the jet. In the regime corresponding to periodic vortex shedding, this shear coupled with the pressure distribution could result in the formation of the column waves seen earlier.

Due to the geometry of the setup, and lack of seed density, the presence of the wake vortices cannot be validated directly. However, the axial velocity measurements indicate the presence of a "wake" region at the rear of the jet. Also, the PIV images displaying a periodic loss of information support the presence of periodically shed vortices from the separation of the shear layer on the jet surface. Therefore, these images provide indirect evidence of the presence of wake structures that significantly affect the jet break up; in this regard, the wake structures play a similar role to those in a single-phase JCIF that contribute to mixing.

CHAPTER 5
CONCLUSIONS AND RECOMMENDATIONS

5.1 Conclusions

The break up mechanisms of a liquid jet in a high speed cross flow of air were studied for various momentum ratios. The three-dimensional flow patterns were visualized using high-speed camera images and PIV measurements in different planes. Based on the results, the following conclusions are made:

1. Lower momentum ratios increased jet bending in the downstream direction; disturbance waves were present in the jet for all the momentum ratios studied.
2. Reasonable agreement was obtained between the present results involving the onset of multimode break up, disturbance wavelengths, and the break up locations and results from past studies; however, the critical Weber number criterion provided by Aalburg et al (2004) appears to be limited. Multimode break up was observed at a Weber number of 15.85, well short of the critical Weber number of 30 specified by Aalburg et al (2004). A comprehensive table was developed highlighting the different types of

break up and regimes encountered in two-phase as a function of the Weber number and the momentum ratio.

3. The PIV measurements indicate that the cross flow wraps around the jet, similar to the flow around a solid cylinder. The measurements highlight the presence of a wake in the rear of the jet and indirectly indicate the presence of periodically shed vortices.
4. The wake structures appear to influence the jet break up significantly. The high shear on the sides of the jet results in the stripping of drops from the jet surface; the shear layer separation from the jet sides could trigger the column waves observed on the jet. It appears that the Rayleigh-Taylor instability is not a leading reason for the jet instability for the momentum ratios between 10 and 172.
5. The present method of using an optical filter and fluorescent seeding droplets for PIV measurements in a two-phase flow provides an avenue to make velocity measurements in different regions of the two-phase JCIF.
6. FLUENT'S Volume of Fluid (VOF) solver package showed great promise for the computational study of a two phase JICF.

5.2 Recommendations

Some of the recommendations to improve future research on this subject are:

1. Construction of the injector and wind tunnel setup in such a way that no interference results in the near field of the jet exit. This would allow for measurements to be made at the top of the test section preventing any interference from the bent liquid column as well.
2. Improvement in the injection of the seeding particles. The current setup produces seeding only in the near wall region. A global seeding system should be designed to seed the entire test section to allow for the capture of instantaneous images.
3. Using a higher speed wind tunnel, study of the critical Weber number for the onset of shear break up.
4. Utilization of a three-dimensional setup for the PIV system to obtain multi plane measurements simultaneously.

REFERENCES

Aalburg, C., Faeth, G.M., Sallam, K.A., 2004 "Properties of Nonturbulent Round Liquid Jets in Uniform Cross flows." *Proceedings of 42nd Aerospace Sciences Meeting and Exhibit*, January 5-8, 2004, Reno, Nevada, USA.

Aalburg, C., Faeth, G.M., Sallam, K.A., Lin, K.C., Carter, C.D., Jackson, T.A., 2004 "Break up of Aerated-Liquid Jets in Supersonic Cross flows." *Proceedings of 42nd Aerospace Sciences Meeting and Exhibit*, January 5-8, 2004, Reno, Nevada, USA.

Aalburg, C., Faeth, G.M., Sallam, K.A., 2004 "Deformation and Surface Waves Propertices of a Round Nonturbulent Liquid Jets in Gaseous Cross flow." *Proceedings of FEDSM2005*, June 19-23, 2005, Houston, TX, USA.

Aalburg, C., Metwally, H.M., Ng, C-L, Sallam, K.A., 2005 "Break up of Round Nonturbulent Liquid Jets in Gaseous Cross flow." *AIAA Journal*, **42** no. 12, pp. 2529-2540.

Andreopoulos, J., 1985 "On the Structure of Jets in a Cross flow." *Journal of Fluid Mechanics*, **157**, pp. 163-197.

Azzopardi, B.J., Birouk, M., Stabler, T., 2003 "Primary break-up of a viscous Liquid Jet in a Cross Airflow." *Particle and Particle System Characterization*, **20**, pp. 283-289.

Baines, D., Keffer, J.F., 1962 "The Round Turbulent Jet in a Cross-Wind." *J. Fluid Mechanics*, **15** no. 4, pp 481-496.

Bartelheimer, J., Finke, H., Grunefeld, G., Kruger, S., 2000 "Gas-Phase Velocity Field Measurements in Sprays Without Particle Seeding." *Experiments in Fluids*, **29**, pp. 238-246.

Bartelheimer, J., Finke, H., Grunefeld, G., Kruger, S., 2000 "Probing the Velocity Fields of Gas and Liquid Phase Simultaneously in a Two-Phase flow." *Experiments in Fluids*, **29**, pp. 322-330.

Blanchard, J.N., Brunet, Y., Merlen, A., 1999 "Inlfuence of a Counter rotating vortex Pair on the Staility of a Jet in a Cross Flow: an Experimental Study by Flow Visualizations." *Experiments in Fluids*, **63**, pp. 63-74.

Boedec, T., Simoens, S., 2001 "Instantaneous and Simultaneous Planar Velocity Field Measurements of Two Phases for Turbulent Mixing of High Pressure Sprays." *Experiments in Fluids*, **31**, pp. 506-518.

Camussi, R., Guj, G., Stella, A., 2002 "Experimental Study of a Jet in a Cross flow at Very Low Reynolds Number." *Journal of Fluid Mechanics*, **454**, pp. 113-144.

Carvalho, I.S., Heitor, M., 1998 "Liquid Film Break-up in a Model of a Prefilming Airblast Nozzle." *Experiments in Fluids*, **24**, pp. 408-415.

Cessou, A., Kosiwczuk, W., Lecordier, B., Tinite, M., 2005 "Simultaneous velocity field Measurements in Two-Phase Flows for Tubulent Mixing of Sporay by Means of Two-Phase PIV," *Exp. In Fluids*, **39**, pp. 895-908.

Chambers, F.W., Sallam, K.A., Sankarakrishnan, R., 2005 "Effects of Turbulece on the Break up of Round Liquid Jets in Gaseous Cross flow." *2005 ASME Fluids*

Engineering Division Summer Meeting and Exhibition, June 19-23, 2005, Houston, TX, FEDSM2005-77407.

Chang, J.M., Huang, R.F., 1994 "The Stability and Visualized Flame and Flow Structures of a Combusting Jet in Cross Flow." *Combustion and Flame*, **98**, pp. 267-278.

Chassaing, P, Claria, A., George, J., Sananes, F., 1974 "Physical Characteristics of Subsonic Jets in a Cross-Stream." *J. Fluid Mechanics*, **62** no. 1, pp. 41-64.

Cowling, R., Soria, J., 2005 "Flow Visualization through Model Abdominal Aortic Aneurysm." *Fourth Australian Conference on Laser Diagnostics in Fluid Mechanics and Combustion*, The University of Adelaide, South Australia, Australia, December 7-9, 2005, pp. 33-36.

Driscoll, K.D., Gray, C., Sick, V., 2003 "Simultaneous Air/Fuel-Phase PIV Measurements in a Dense Fuel Spray." *Experiments in Fluids,* **35**, pp. 112-115.

Dullenkopf, K., Gindele, J., Hentschel, W., Merzkirch, W., Raposo, J., Rottenkolber, G., Spicher, U., Wittig, S., 2002 "Spray Analysis of a Gasoline Direct Injector by Means of Two-Phase PIV." *Experiments in Fluids*, **32**, pp. 710-721.

Eiff, O.S., Keffer, J., 1997 "On the Structure in the Near-wake Region of an Elevated Turbulent Jet in a Cross flow." *Journal of Fluid Mechanics*, **333**, pp. 161-195.

Eskinazi, S., Moussa, Z.M., Trischka, J.W., 1977 "The Near Field in the Mixing of a Round Jet with a Cross-Stream." *J. Fluid Mechanics*, **80** no. 1, pp. 49-81.

Fearn, R., Weston, R.P., 1974 "Vorticity Associated with a Jet in Cross Flow." *AIAA Journal*, pp. 1666-1671.

Ferre, J.A., Giralt, F., Rivero, A., 2001 "Organized Motions in a Jet in Cross flow." *Journal of Fluid Mechanics*, **444**, pp. 117-149.

Ferziger, J.H., Street, R.L., Yuan, L.L., 1999 "Large-eddy Simulations of a Round Jet in Cross flow." *Journal of Fluid Mechanics*, **379**, pp. 71-104.

Fric, T.F., Roshko, A., 1994 "Vortical Structure in the Wake of a Transverse Jet." *Journal of Fluid Mechanics*, **279**, pp. 1-47.

Fuller, R.P, Kirkendall, K.A., Wu, P-K, 1997 "Break up Processes of Liquid Jets in Subsonic Cross flows." *Journal of Propulsion and Power*, **13** no. 1, pp. 64-73.

Fuller, R.P, Kirkendall, K.A., Wu, P-K, 1998 "Spray Structures of Liquid Jets Atomized in Subsonic Cross flows." *Journal of Propulsion and Power*, **14** no. 2, pp. 173-182.

Gollahalli, S.R., Pardiwalla, D., "Comparison of the Flame Characteristics of Turbulent Circular and Elliptic Jets in a Crossflow." *Journal of Energy Resources Technology*, **124**, pp. 197-203.

Grant, I., 1997 "Particle Image Velocimetry: a review." *Proc. Instn. Mech. Engrs.*, **211**, pp. 55-76.

Hester, D.D., McMahon, H.M., Palfery, J.G., 1971 "Vorte Shedding from a Turbulent Jet in a Cross-Wind." *J. Fluid Mechanics*, **48** no. 1, pp. 73-80.

Horn, K.P., Reichenbach, R.E., 1971 "Investigation of Injectant Properties on Jet Penetration in a Supersonic Stream." *AIAA Journal*, **9** no. 3, pp. 469-472.

Huang, R.F., Yang, M.J., "Thermal and Concentration Fields of Burner-Attached Jet Flames in Cross Flow." *Combustion and Flame*, **105**, pp. 211-224.

Kelso, R.M., Lim, T.T., Perry, A.E., 1996 "An Experimental Study of Round Jets in Cross-Flow." *Journal of Fluid Mechanics*, **306**, pp. 111-144.

Khalitov, D.A., Longmire, E.K., 2003 "Effect of Particle Size on Velocity correlations in Tubulent Channel Flow." *Proceedings of 4th ASME/FED and JSME Joint Fluids Conference*, July 6-10, 2003, Honolulu, Hawaii, USA.

Kiger, K.T., Pan, C., 2000 "PIV Technique for the Simultaneous Measurement of Dilute Two-Phase Flows." *Journal of Fluids Engineering*, **122**, pp. 811-818.

Kompenhans, J., Stanislas, M., Westerweel, J., 2000 "Particle Image Velocimetry: Progress towards Industrial Application," Dordrecht: Kluwer Academic Publishers, pp. 177-180.

Larsen, P.S., Ozcan, O., 2001 "Laser Doppler Anemometry Study of a Turbulent Jet in Cross flow." *AIAA Journal*, **41**, no. 8, pp. 1614-1615.

Lecuona, A., Nogueira, J., Ruiz-Rivas, U., 2002 "Simulation of Particle Trajectories in a voretex-Induced Flow: application to seed-dependent flow measurement techniques." *Journal of Measurement Science Technology*, **13**, pp. 1020-1028.

Less, D.M., Schetz, J.A., 1986 "Transient behavior of Liquid jets injected normal to a high-velocity gas stream." *AIAA Journal*, **24** no. 12, pp. 1979-1985.

Melling, A., 1997 "Tracer Particles and Seeding for Particle Image Velocimetry." *Journal of Measurement Science and Technology*, **8**, pp. 1406-1416.

Padhye, A., Schetz, J.A., 1977 "Penetration and Break up of Liquids in Subsonic Airstreams." *AIAA Journal*, **15** no. 15, pp. 1385-1390.

Pourdeyhimi, B., Vahedi Tafreshi, H., 2003 “The Effects of Nozzle Geometry on Waterjet Break up at High Reynolds Numbers.” *Experiments in Fluids*, **35**, pp. 364-371.

Schetz, J.A., 1980 “Injection and Mixing in Turbulent Flow,” New York City: *AIAA*, pp. 162.

APPENDIX A

Table A 1 Wind tunnel calibration using pitot probe. 118
Table A 2 Rotameter flow meter calibration check. 119
Table A 3 Viscosity measurements of jet fluid. 119
Table A 4 Jet width measurements for q = 18.8 120
Table A 5 Jet width measurements for q = 10. 121
Table A 6 Test section velocity check with PIV 122
Table A 7 Cross sectional velocity profile for 30 Hz. 123
Table A 8 Cross sectional velocity profile for 40 Hz. 125
Table A 9 Cross sectional velocity profile for 45 Hz. 127
Table A 10 Cross sectional velocity profile for 50 Hz. 129
Table A 11 Cross sectional velocity profile for 60 Hz. 131
Table A 12 Wind tunnel calibration re-check with pitot probe. 133
Table A 13 Image variance of PIV measurements for q = 78. 134
Table A 14 Image variance of PIV measurements for q = 44. 135
Table A 15 Repeatability of PIV images for q = 78. 136
Table A 16 Repeatability of PIV images for q = 44. 136
Table A 17 Side velocity profile for q = 78, at Y/d = 2. 137
Table A 18 Side velocity profile for q = 78, at Y/d = 4. 139
Table A 19 Side velocity profile for q = 44, at Y/d = 2. 141
Table A 20 Side velocity profile for q = 44, at Y/d = 4. 143
Table A 21 Proximal velocity profile for q = 78. 145
Table A 22 Proximal velocity profile for q = 44. 147
Table A 23 Spray characteristic break up matrix 150
Table A 24 Wavelength and break up locations for q=10. 152
Table A 25 Wavelength and break up locations for q=18.8. 152
Table A 26 Wavelength and break up locations for q=40. 153

Table A 1 Wind tunnel calibration using pitot probe.

Controller Freq	Pos	Delta P (mmH20)	Delta P (in H20)	Delta P (Pa)	V (m/s)	Q (m3/s)
10	1	1.3	0.0512	12.758	4.646	0.816
	2	1.3	0.0512	12.758	4.646	0.816
	3	1.3	0.0512	12.758	4.646	0.816
	avg	1.3	0.0512	12.758	4.646	0.816
	stdev	0	0.0000	0.000	0.000	0.000
15	1	2.8	0.1103	27.479	6.819	1.198
	2	2.8	0.1103	27.479	6.819	1.198
	3	2.8	0.1103	27.479	6.819	1.198
	avg	2.8	0.1103	27.479	6.819	1.198
	stdev	0	0.0000	0.000	0.000	0.000
20	1	5	0.1970	49.071	9.112	1.601
	2	5	0.1970	49.071	9.112	1.601
	3	5	0.1970	49.071	9.112	1.601
	avg	5	0.1970	49.071	9.112	1.601
	stdev	0	0.0000	0.000	0.000	0.000
25	1	8	0.3152	78.513	11.526	2.025
	2	8.1	0.3191	79.494	11.598	2.038
	3	8.1	0.3191	79.494	11.598	2.038
	avg	8.07	0.3178	79.167	11.574	2.034
	stdev	0.06	0.0023	0.567	0.041	0.007
30	1	12.2	0.4807	119.732	14.233	2.501
	2	12.2	0.4807	119.732	14.233	2.501
	3	12.1	0.4767	118.751	14.175	2.491
	avg	12.17	0.4794	119.405	14.214	2.497
	stdev	0	0.0000	0.000	0.000	0.000
35	1	17.2	0.6777	168.803	16.900	2.969
	2	17.2	0.6777	168.803	16.900	2.969
	3	17.2	0.6777	168.803	16.900	2.969
	avg	17.2	0.6777	168.803	16.900	2.969
	stdev	0	0.0000	0.000	0.000	0.000
40	1	22.8	0.8983	223.762	19.458	7.226
	2	22.8	0.8983	223.762	19.458	7.226
	3	22.8	0.8983	223.762	19.458	7.226
	avg	22.8	0.8983	223.762	19.458	7.226
	stdev	0	0.0000	0.000	0.000	0.000
50	1	37.5	1.4775	368.029	24.954	9.268
	2	37.5	1.4775	368.029	24.954	9.268
	3	37.5	1.4775	368.029	24.954	9.268
	avg	37.5	1.4775	368.029	24.954	9.268
60	1	55.3	2.1788	542.720	30.304	11.254
	2	55.2	2.1749	541.738	30.276	11.244
	3	55.2	2.1749	541.738	30.276	11.244
	avg	55.23	2.1762	542.066	30.285	11.247

stdev	0	0.0000	0.000	0.000	0.000

Table A 2 Rotameter flow meter calibration check.

Trial #	Rotameter Flow Rate (lpm)	Actual Flow Rate (lpm)
1	0.6	0.626
2	0.6	0.624
3	0.6	0.623
1	0.4	0.426
2	0.4	0.415
3	0.4	0.428
1	0.8	0.792
2	0.8	0.788
3	0.8	0.791
1	0.5	0.524
2	0.5	0.526
3	0.5	0.53
1	0.7	0.713
2	0.7	0.707
3	0.7	0.72

Table A 3 Viscosity measurements of jet fluid.

Trial	Time (s)	Kinematic Viscosity (cSt)	Kinematic Viscosity (m2/s)	Dynamic Viscosity (m2/s)
1	77.33	1.16	1.16E-06	1.16E-03
2	74.04	1.11	1.11E-06	1.11E-03
3	77.36	1.16	1.16E-06	1.16E-03
4	75.78	1.14	1.14E-06	1.14E-03
5	75.73	1.14	1.14E-06	1.14E-03
6	75.30	1.13	1.13E-06	1.13E-03
7	76.74	1.15	1.15E-06	1.15E-03
8	74.85	1.12	1.12E-06	1.12E-03
9	73.84	1.11	1.11E-06	1.11E-03
10	75.12	1.13	1.13E-06	1.13E-03
avg	75.61	1.13	1.13E-06	1.13E-03
stdev	1.2406	0.0186	1.86E-08	1.86E-05

Table A 4 Jet width measurements for q = 18.8

Xpaper (in)	Xactual (cm)	Xactual (mm)	X/d	Wpaper (in)	Wactual (cm)	Wactual (mm)	W/d
0.25	1.172	11.715	5.858	0.222	1.040	10.403	5.201
0.25	1.172	11.715	5.858	0.216	1.012	10.122	5.061
0.25	1.172	11.715	5.858	0.234	1.097	10.965	5.483
0.25	1.172	11.715	5.858	0.224	1.050	10.497	5.248
0.25	1.172	11.715	5.858	0.23	1.078	10.778	5.389
0.25	1.172	11.715	5.858	0.22	1.031	10.309	5.155
0.25	1.172	11.715	5.858	0.219	1.026	10.262	5.131
0.25	1.172	11.715	5.858	0.234	1.097	10.965	5.483
0.25	1.172	11.715	5.858	0.27	1.265	12.652	6.326
0.25	1.172	11.715	5.858	0.2	0.937	9.372	4.686
0.25	1.172	11.715	5.858	0.2	0.937	9.372	4.686
0.25	1.172	11.715	5.858	0.222	1.040	10.403	5.201
0.25	1.172	11.715	5.858	0.213	0.998	9.981	4.991
0.25	1.172	11.715	5.858	0.232	1.087	10.872	5.436
0.25	1.172	11.715	5.858	0.208	0.975	9.747	4.873
0.25	1.172	11.715	5.858	0.223	1.045	10.450	5.225
0.25	1.172	11.715	5.858	0.226	1.059	10.590	5.295
0.25	1.172	11.715	5.858	0.231	1.082	10.825	5.412
0.25	1.172	11.715	5.858	0.229	1.073	10.731	5.366
0.25	1.172	11.715	5.858	0.236	1.106	11.059	5.530
0.500	2.343	23.430	11.715	0.343	1.607	16.073	8.037
0.500	2.343	23.430	11.715	0.329	1.542	15.417	7.709
0.500	2.343	23.430	11.715	0.345	1.617	16.167	8.083
0.500	2.343	23.430	11.715	0.328	1.537	15.370	7.685
0.500	2.343	23.430	11.715	0.343	1.607	16.073	8.037
0.500	2.343	23.430	11.715	0.339	1.589	15.886	7.943
0.500	2.343	23.430	11.715	0.330	1.546	15.464	7.732
0.500	2.343	23.430	11.715	0.311	1.457	14.574	7.287
0.500	2.343	23.430	11.715	0.388	1.818	18.182	9.091
0.500	2.343	23.430	11.715	0.343	1.607	16.073	8.037
0.500	2.343	23.430	11.715	0.289	1.354	13.543	6.771
0.500	2.343	23.430	11.715	0.310	1.453	14.527	7.263
0.500	2.343	23.430	11.715	0.350	1.640	16.401	8.201
0.500	2.343	23.430	11.715	0.320	1.500	14.995	7.498
0.500	2.343	23.430	11.715	0.342	1.603	16.026	8.013
0.500	2.343	23.430	11.715	0.348	1.631	16.307	8.154
0.500	2.343	23.430	11.715	0.351	1.645	16.448	8.224
0.500	2.343	23.430	11.715	0.344	1.612	16.120	8.060
0.500	2.343	23.430	11.715	0.359	1.682	16.823	8.411
0.500	2.343	23.430	11.715	0.340	1.593	15.933	7.966
0.750	3.515	35.145	17.573	0.444	2.081	20.806	10.403
0.750	3.515	35.145	17.573	0.450	2.109	21.087	10.544
0.750	3.515	35.145	17.573	0.442	2.071	20.712	10.356
0.750	3.515	35.145	17.573	0.46	2.156	21.556	10.778

0.750	3.515	35.145	17.573	0.462	2.165	21.649	10.825
0.750	3.515	35.145	17.573	0.453	2.123	21.228	10.614
0.750	3.515	35.145	17.573	0.441	2.067	20.665	10.333
0.750	3.515	35.145	17.573	0.430	2.015	20.150	10.075
0.750	3.515	35.145	17.573	0.484	2.268	22.680	11.340
0.750	3.515	35.145	17.573	0.458	2.146	21.462	10.731
0.750	3.515	35.145	17.573	0.416	1.949	19.494	9.747
0.750	3.515	35.145	17.573	0.409	1.917	19.166	9.583
0.750	3.515	35.145	17.573	0.452	2.118	21.181	10.590
0.750	3.515	35.145	17.573	0.440	2.062	20.619	10.309
0.750	3.515	35.145	17.573	0.460	2.156	21.556	10.778
0.750	3.515	35.145	17.573	0.483	2.263	22.634	11.317
0.750	3.515	35.145	17.573	0.442	2.071	20.712	10.356
0.750	3.515	35.145	17.573	0.428	2.006	20.056	10.028
0.750	3.515	35.145	17.573	0.453	2.123	21.228	10.614
0.750	3.515	35.145	17.573	0.484	2.268	22.680	11.340

Table A 5 Jet width measurements for q = 10.

Xpaper (in)	Xactual (cm)	Xactual (mm)	X/d	Wpaper (in)	Wactual (cm)	Wactual (mm)	W/d
0.25	1.172	11.715	5.858	0.228	1.068	10.684	5.342
0.25	1.172	11.715	5.858	0.23	1.078	10.778	5.389
0.25	1.172	11.715	5.858	0.244	1.143	11.434	5.717
0.25	1.172	11.715	5.858	0.246	1.153	11.528	5.764
0.25	1.172	11.715	5.858	0.23	1.078	10.778	5.389
0.25	1.172	11.715	5.858	0.226	1.059	10.590	5.295
0.25	1.172	11.715	5.858	0.233	1.092	10.918	5.459
0.25	1.172	11.715	5.858	0.223	1.045	10.450	5.225
0.25	1.172	11.715	5.858	0.221	1.036	10.356	5.178
0.25	1.172	11.715	5.858	0.226	1.059	10.590	5.295
0.25	1.172	11.715	5.858	0.222	1.040	10.403	5.201
0.25	1.172	11.715	5.858	0.238	1.115	11.153	5.576
0.25	1.172	11.715	5.858	0.227	1.064	10.637	5.319
0.25	1.172	11.715	5.858	0.22	1.031	10.309	5.155
0.25	1.172	11.715	5.858	0.225	1.054	10.544	5.272
0.25	1.172	11.715	5.858	0.227	1.064	10.637	5.319
0.25	1.172	11.715	5.858	0.218	1.022	10.216	5.108
0.25	1.172	11.715	5.858	0.237	1.111	11.106	5.553
0.25	1.172	11.715	5.858	0.21	0.984	9.841	4.920
0.500	2.343	23.430	11.715	0.313	1.467	14.667	7.334
0.500	2.343	23.430	11.715	0.315	1.476	14.761	7.381
0.500	2.343	23.430	11.715	0.316	1.481	14.808	7.404
0.500	2.343	23.430	11.715	0.270	1.265	12.652	6.326
0.500	2.343	23.430	11.715	0.272	1.275	12.746	6.373
0.500	2.343	23.430	11.715	0.275	1.289	12.887	6.443

0.500	2.343	23.430	11.715	0.288	1.350	13.496	6.748
0.500	2.343	23.430	11.715	0.298	1.396	13.964	6.982
0.500	2.343	23.430	11.715	0.275	1.289	12.887	6.443
0.500	2.343	23.430	11.715	0.305	1.429	14.292	7.146
0.500	2.343	23.430	11.715	0.300	1.406	14.058	7.029
0.500	2.343	23.430	11.715	0.275	1.289	12.887	6.443
0.500	2.343	23.430	11.715	0.280	1.312	13.121	6.560
0.500	2.343	23.430	11.715	0.270	1.265	12.652	6.326
0.500	2.343	23.430	11.715	0.276	1.293	12.933	6.467
0.500	2.343	23.430	11.715	0.309	1.448	14.480	7.240
0.500	2.343	23.430	11.715	0.272	1.275	12.746	6.373
0.500	2.343	23.430	11.715	0.278	1.303	13.027	6.514
0.500	2.343	23.430	11.715	0.288	1.350	13.496	6.748
0.750	3.515	35.145	17.573	0.356	1.668	16.682	8.341
0.750	3.515	35.145	17.573	0.345	1.617	16.167	8.083
0.750	3.515	35.145	17.573	0.358	1.678	16.776	8.388
0.750	3.515	35.145	17.573	0.36	1.687	16.870	8.435
0.750	3.515	35.145	17.573	0.345	1.617	16.167	8.083
0.750	3.515	35.145	17.573	0.365	1.710	17.104	8.552
0.750	3.515	35.145	17.573	0.360	1.687	16.870	8.435
0.750	3.515	35.145	17.573	0.359	1.682	16.823	8.411
0.750	3.515	35.145	17.573	0.360	1.687	16.870	8.435
0.750	3.515	35.145	17.573	0.368	1.724	17.245	8.622
0.750	3.515	35.145	17.573	0.355	1.664	16.635	8.318
0.750	3.515	35.145	17.573	0.365	1.710	17.104	8.552
0.750	3.515	35.145	17.573	0.340	1.593	15.933	7.966
0.750	3.515	35.145	17.573	0.359	1.682	16.823	8.411
0.750	3.515	35.145	17.573	0.330	1.546	15.464	7.732
0.750	3.515	35.145	17.573	0.343	1.607	16.073	8.037
0.750	3.515	35.145	17.573	0.358	1.678	16.776	8.388
0.750	3.515	35.145	17.573	0.365	1.710	17.104	8.552
0.750	3.515	35.145	17.573	0.368	1.724	17.245	8.622

Table A 6 Test section velocity check with PIV.

Freq (Hz)	Mean Velocity PIV (m/s)	Mean Velocity Calib. (m/s)	Percent Difference
30.6	14.13	15.01	5.86
40	19.23	19.62	1.99
45	21.42	22.07	2.96
50	24.18	24.53	1.41
60	29.83	29.43	1.36

Table A 7 Cross sectional velocity profile for 30 Hz.

30HZ				
X (mm)	Z (mm)	U (m/s)	V (m/s)	Vel. Mag (m/s)
64.262	27.812	-14.733	-0.714	14.752
64.262	27.454	-14.554	-0.539	14.567
64.262	27.097	-14.298	-0.341	14.304
64.262	26.739	-14.167	-0.216	14.168
64.262	26.381	-14.020	-0.250	14.023
64.262	26.024	-13.877	-0.277	13.880
64.262	25.666	-13.762	-0.297	13.765
64.262	25.308	-13.856	-0.234	13.859
64.262	24.951	-13.985	-0.171	13.987
64.262	24.593	-14.054	-0.100	14.056
64.262	24.235	-14.206	0.126	14.212
64.262	23.878	-14.385	0.413	14.398
64.262	23.520	-14.427	0.536	14.444
64.262	23.162	-14.012	0.561	14.031
64.262	22.805	-13.509	0.597	13.532
64.262	22.447	-13.290	0.562	13.313
64.262	22.089	-13.470	0.246	13.486
64.262	21.732	-13.705	-0.130	13.712
64.262	21.374	-13.817	-0.280	13.820
64.262	21.016	-13.995	-0.236	13.998
64.262	20.659	-14.190	-0.207	14.192
64.262	20.301	-14.319	-0.117	14.320
64.262	19.943	-14.370	0.012	14.371
64.262	19.586	-	0.136	14.416

		14.415		
		-		
64.262	19.228	14.437	0.244	14.440
64.262	18.870	14.319	0.378	14.326
		-		
64.262	18.513	14.184	0.546	14.197
		-		
64.262	18.155	14.103	0.555	14.116
		-		
64.262	17.797	14.011	0.478	14.022
		-		
64.262	17.440	13.913	0.410	13.922
		-		
64.262	17.082	13.827	0.252	13.836
		-	-	
64.262	16.725	13.822	0.064	13.833
		-	-	
64.262	16.367	13.846	0.389	13.856
		-	-	
64.262	16.009	13.833	0.545	13.845
		-	-	
64.262	15.652	13.975	0.499	13.985
		-	-	
64.262	15.294	14.121	0.466	14.130
		-	-	
64.262	14.936	14.234	0.299	14.240
		-	-	
64.262	14.579	14.322	0.091	14.327
		-		
64.262	14.221	14.409	0.095	14.413
		-		
64.262	13.863	14.446	0.206	14.451
		-	-	
64.262	13.506	14.507	0.062	14.516
		-	-	
64.262	13.148	14.589	0.346	14.603
		-	-	
64.262	12.790	14.590	0.438	14.603
		-	-	
64.262	12.433	14.585	0.286	14.594
		-	-	
64.262	12.075	14.570	0.118	14.574
		-	-	
64.262	11.717	14.623	0.087	14.625
		-		
64.262	11.360	14.747	0.020	14.748
		-		
64.262	11.002	14.880	0.144	14.882
		-		
64.262	10.644	14.915	0.083	14.916
		-	-	
64.262	10.287	14.825	0.043	14.827

Table A 8 Cross sectional velocity profile for 40 Hz.

40HZ				
X (mm)	Z (mm)	U (m/s)	V (m/s)	Vel. Mag (m/s)
65.180	28.631	-18.955	-0.385	18.991
65.180	28.425	-19.049	-0.586	19.092
65.180	28.219	-19.148	-0.790	19.199
65.180	28.014	-19.215	-0.776	19.312
65.180	27.808	-19.314	-0.593	19.502
65.180	27.603	-19.403	-0.428	19.673
65.180	27.397	-19.327	-0.375	19.534
65.180	27.192	-19.238	-0.342	19.371
65.180	26.986	-19.193	-0.316	19.285
65.180	26.780	-19.208	-0.389	19.279
65.180	26.575	-19.221	-0.459	19.273
65.180	26.369	-19.179	-0.477	19.232
65.180	26.164	-19.129	-0.481	19.190
65.180	25.958	-19.081	-0.519	19.146
65.180	25.753	-18.996	-0.619	19.061
65.180	25.547	-18.910	-0.718	18.975
65.180	25.341	-18.886	-0.741	18.951
65.180	25.136	-18.902	-0.713	18.967
65.180	24.930	-18.910	-0.684	18.975
65.180	24.725	-18.925	-0.616	19.020
65.180	24.519	-18.940	-0.536	19.068

65.180	24.313	-18.956	-0.526	19.086
65.180	24.108	-18.979	-0.612	19.070
65.180	23.902	-19.002	-0.694	19.054
65.180	23.697	-19.059	-0.684	19.102
65.180	23.491	-19.139	-0.660	19.175
65.180	23.286	-19.179	-0.639	19.209
65.180	23.080	-19.091	-0.594	19.120
65.180	22.874	-19.002	-0.550	19.032
65.180	22.669	-18.965	-0.532	18.994
65.180	22.463	-18.942	-0.525	18.971
65.180	22.258	-18.918	-0.516	18.946
65.180	22.052	-18.868	-0.453	18.895
65.180	21.847	-18.814	-0.388	18.842
65.180	21.641	-18.799	-0.365	18.828
65.180	21.435	-18.828	-0.386	18.856
65.180	21.230	-18.857	-0.408	18.884
65.180	21.024	-18.836	-0.444	18.863
65.180	20.819	-18.811	-0.492	18.841
65.180	20.613	-18.793	-0.533	18.822
65.180	20.408	-18.787	-0.557	18.817
65.180	20.202	-18.782	-0.581	18.811
65.180	19.996	-18.773	-0.618	18.804
65.180	19.791	-18.759	-0.654	18.795
65.180	19.585	-18.742	-0.684	18.783
65.180	19.380	18.740	0.676	18.776
65.180	19.174	18.741	0.666	18.772
65.180	18.969	-18.713	-0.640	18.742

65.180	18.763	-18.597	-0.567	18.624
65.180	18.557	-18.496	-0.499	18.521
65.180	18.352	-18.596	-0.511	18.625
65.180	18.146	-18.714	-0.528	18.746
65.180	17.941	-18.823	-0.491	18.855
65.180	17.735	-18.995	-0.372	19.029
65.180	17.530	-19.167	-0.252	19.204
65.180	17.324	-19.134	-0.233	19.164
65.180	17.118	-19.008	-0.280	19.030
65.180	16.913	-18.914	-0.324	18.930
65.180	16.707	-18.981	-0.294	18.999
65.180	16.502	-19.059	-0.257	19.080
65.180	16.296	-19.046	-0.283	19.067
65.180	16.091	-18.984	-0.354	19.003
65.180	15.885	-18.922	-0.421	18.940
65.180	15.679	-19.021	-0.459	19.043

Table A 9 Cross sectional velocity profile for 45 Hz.

45HZ

X (mm)	Z (mm)	U (m/s)	V (m/s)	Vel. Mag (m/s)
66.007	28.753	-21.487	-0.451	21.500
66.007	28.410	-21.518	-0.468	21.531
66.007	28.067	-21.548	-0.483	21.562
66.007	27.723	-21.577	-0.500	21.593
66.007	27.380	-21.583	-0.511	21.599
66.007	27.037	-21.597	-0.521	21.613
66.007	26.694	-21.603	-0.532	21.620

66.007	26.350	-21.599	-0.536	21.617
66.007	26.007	-21.595	-0.542	21.613
66.007	25.664	-21.591	-0.545	21.609
66.007	25.321	-21.577	-0.560	21.597
66.007	24.977	-21.551	-0.576	21.572
66.007	24.634	-21.535	-0.593	21.558
66.007	24.291	-21.539	-0.596	21.561
66.007	23.948	-21.547	-0.594	21.567
66.007	23.605	-21.558	-0.591	21.577
66.007	23.261	-21.548	-0.585	21.565
66.007	22.918	-21.524	-0.575	21.542
66.007	22.575	-21.499	-0.566	21.517
66.007	22.232	-21.479	-0.558	21.496
66.007	21.888	-21.466	-0.551	21.482
66.007	21.545	-21.456	-0.546	21.471
66.007	21.202	-21.439	-0.536	21.454
66.007	20.859	-21.421	-0.524	21.435
66.007	20.515	-21.402	-0.510	21.416
66.007	20.172	-21.382	-0.494	21.396
66.007	19.829	-21.358	-0.468	21.370
66.007	19.486	-21.336	-0.440	21.347
66.007	19.142	-21.319	-0.413	21.329
66.007	18.799	-21.338	-0.380	21.348
66.007	18.456	-21.356	-0.348	21.365
66.007	18.113	-21.374	-0.318	21.383
66.007	17.770	-21.368	-0.328	21.377
66.007	17.426	-21.368	-0.341	21.379

66.007	17.083	-21.361	-0.351	21.373
66.007	16.740	-21.329	-0.339	21.341
66.007	16.397	-21.289	-0.325	21.300
66.007	16.053	-21.255	-0.312	21.266
66.007	15.710	-21.234	-0.320	21.244
66.007	15.367	-21.216	-0.332	21.227
66.007	15.024	-21.196	-0.344	21.208
66.007	14.680	-21.185	-0.352	21.198
66.007	14.337	-21.172	-0.357	21.185
66.007	13.994	-21.164	-0.363	21.178
66.007	13.651	-21.170	-0.359	21.184
66.007	13.307	-21.184	-0.351	21.197
66.007	12.964	-21.198	-0.341	21.211
66.007	12.621	-21.193	-0.329	21.205
66.007	12.278	-21.171	-0.314	21.183
66.007	11.934	-21.151	-0.300	21.163

Table A 10 Cross sectional velocity profile for 50 Hz.

50HZ				
X (mm)	Z (mm)	U (m/s)	V (m/s)	Vel. Mag (m/s)
68.048	27.293	-24.364	0.134	24.370
68.048	26.965	-24.717	-0.187	24.724
68.048	26.636	-25.063	-0.508	25.072
68.048	26.308	-25.199	-0.756	25.212
68.048	25.979	-25.236	-0.963	25.257
68.048	25.651	-25.273	1.169	25.302

68.048	25.323	-25.311	-1.446	25.355
68.048	24.994	-25.116	-1.788	25.187
68.048	24.666	-24.922	-2.130	25.019
68.048	24.338	-24.764	-2.349	24.878
68.048	24.009	-24.466	-2.046	24.556
68.048	23.681	-24.158	-1.755	24.226
68.048	23.352	-23.866	-1.441	23.912
68.048	23.024	-23.902	-1.303	23.940
68.048	22.696	-23.999	-1.177	24.030
68.048	22.367	-24.091	-1.051	24.115
68.048	22.039	-24.031	-1.038	24.055
68.048	21.711	-24.034	-0.999	24.055
68.048	21.382	-24.036	-0.960	24.056
68.048	21.054	-23.948	-0.931	23.967
68.048	20.725	-23.795	-0.744	23.809
68.048	20.397	-23.642	-0.556	23.651
68.048	20.069	-23.558	-0.408	23.563
68.048	19.740	-23.592	-0.363	23.595
68.048	19.412	-23.626	-0.329	23.629
68.048	19.083	-23.658	-0.273	23.660
68.048	18.755	-23.516	-0.525	23.526
68.048	18.427	-23.286	-0.771	23.302
68.048	18.098	-23.066	-1.021	23.090
68.048	17.770	-23.179	-1.190	23.210
68.048	17.442	-23.384	-1.293	23.420
68.048	17.113	-23.588	-1.395	23.630
68.048	16.785	-23.739	-1.494	23.787

68.048	16.456	-23.940	-1.613	23.996
68.048	16.128	-24.141	-1.732	24.204
68.048	15.800	-24.294	-1.820	24.362
68.048	15.471	-24.382	-1.924	24.459
68.048	15.143	-24.471	-2.039	24.556
68.048	14.814	-24.560	-2.130	24.652
68.048	14.486	-24.619	-2.153	24.713
68.048	14.158	-24.651	-2.143	24.744
68.048	13.829	-24.687	-2.138	24.780
68.048	13.501	-24.633	-1.957	24.714
68.048	13.173	-24.508	-1.638	24.568
68.048	12.844	24.383	1.319	24.422
68.048	12.516	-24.208	-1.047	24.233
68.048	12.187	-24.104	-1.025	24.128
68.048	11.859	-23.999	-1.003	24.023
68.048	11.531	-23.892	0.893	23.911

Table A 11 Cross sectional velocity profile for 60 Hz.

60HZ

X (mm)	Z (mm)	U (m/s)	V (m/s)	Vel. Mag (m/s)
66.177	28.113	-29.328	-0.737	29.337
66.177	27.799	-29.465	-0.864	29.479
66.177	27.484	-29.646	-1.055	29.667
66.177	27.170	-29.810	-1.221	29.837
66.177	26.855	-29.780	-1.210	29.807
66.177	26.540	-29.640	-1.052	29.660
66.177	26.226	-29.499	-0.895	29.514

66.177	25.911	-29.401	-0.805	29.413
66.177	25.596	-29.283	-0.591	29.291
66.177	25.282	-29.167	-0.374	29.172
66.177	24.967	-29.048	-0.162	29.048
66.177	24.653	-29.032	-0.116	29.032
66.177	24.338	-29.009	-0.084	29.009
66.177	24.023	-28.986	-0.052	28.986
66.177	23.709	-29.017	-0.054	29.017
66.177	23.394	-28.949	-0.045	28.949
66.177	23.079	-28.881	-0.036	28.881
66.177	22.765	-28.858	-0.027	28.858
66.177	22.450	-28.654	0.065	28.654
66.177	22.135	-28.439	0.107	28.440
66.177	21.821	-28.230	0.178	28.232
66.177	21.506	-28.383	0.370	28.388
66.177	21.192	-28.645	0.689	28.658
66.177	20.877	-28.908	1.008	28.928
66.177	20.562	-29.062	1.082	29.083
66.177	20.248	-29.066	0.847	29.081
66.177	19.933	-29.092	0.597	29.101
66.177	19.618	-29.059	0.386	29.062
66.177	19.304	-28.739	0.355	28.741
66.177	18.989	-28.388	0.315	28.390
66.177	18.674	-28.039	0.276	28.040
66.177	18.360	-27.960	0.288	27.962
66.177	18.045	-28.053	0.408	28.057
66.177	17.731	-28.147	0.527	28.152

66.177	17.416	-28.247	0.557	28.253
66.177	17.101	-28.325	0.428	28.330
66.177	16.787	-28.411	0.294	28.414
66.177	16.472	-28.491	0.163	28.492
66.177	16.157	-28.569	0.136	28.570
66.177	15.843	-28.747	-0.010	28.749
66.177	15.528	-28.925	-0.155	28.927
66.177	15.214	-28.903	-0.137	28.905
66.177	14.899	-28.884	-0.014	28.886
66.177	14.584	-28.882	0.126	28.884
66.177	14.270	-28.807	0.193	28.807
66.177	13.955	-28.956	0.016	28.957
66.177	13.640	-28.981	0.137	28.983
66.177	13.326	-29.032	-0.295	29.034
66.177	13.011	-29.252	-0.568	29.261
66.177	12.696	-29.550	-1.044	29.577

Table A 12 Wind tunnel calibration re-check with pitot probe.

Frequency (Hz)	DeltaP (in H20)	Vpitot (m/s)	Vcalib (m/s)
23.5	0.27	10.56	11.5
23.5	0.27	10.56	11.5
23.5	0.27	10.56	11.5
23.5	0.27	10.56	11.5
avg	0.27	10.56	11.5
stdev	0	0	0
30.6	0.49	14.24	15
30.6	0.48	14.09	15
30.6	0.49	14.24	15
30.6	0.48	14.09	15
avg	0.49	14.17	15
stdev	0.0058	0.0866	0

Table A 13 Image variance of PIV measurements for q = 78.

	Images	X (mm)	Y (mm)	Vel. Mag (m/s)	U (m/s)	V (m/s)	% Diff.
	50	149.415	192.541	11.737	0.643	11.695	
	100	149.415	192.541	10.469	0.332	10.425	12.110
	150	149.415	192.541	10.532	0.272	10.481	0.598
	200	149.415	192.541	10.630	0.204	10.567	0.924
	250	149.415	192.541	10.598	0.137	10.534	-0.309
	300	149.415	192.541	10.491	0.120	10.430	-1.019
avg.				10.743	0.284	10.688	-2.383
stdev				0.491	0.193	0.496	5.491

	Images	X (mm)	Y (mm)	Vel. Mag (m/s)	U (m/s)	V (m/s)	% Diff.
	50	152.064	180.178	11.856	0.096	11.782	
	100	152.064	180.178	10.885	0.003	10.722	-8.924
	150	152.064	180.178	10.851	0.110	10.682	-0.313
	200	152.064	180.178	10.975	0.278	10.801	1.128
	250	152.064	180.178	11.047	0.063	10.864	0.656
	300	152.064	180.178	10.953	0.022	10.785	-0.858
avg.				11.095	0.095	10.939	-1.662
stdev				0.380	0.099	0.418	4.134

	Images	X (mm)	Y (mm)	Vel. Mag (m/s)	U (m/s)	V (m/s)	% Diff.
	50	149.268	160.309	10.805	0.922	10.691	
	100	149.268	160.309	10.447	0.121	10.299	-3.422
	150	149.268	160.309	10.340	0.291	10.171	-1.041
	200	149.268	160.309	10.458	0.322	10.304	1.130
	250	149.268	160.309	10.294	0.328	10.135	-1.589
	300	149.268	160.309	10.439	0.285	10.277	1.389
avg.				10.464	0.378	10.313	-0.707
stdev				0.180	0.277	0.198	2.002

Field Average Velocity (m/s)	Deviation (m/s)
10.628	0.283

Table A 14 Image variance of PIV measurements for q = 44.

	Images	X (mm)	Y (mm)	Vel. Mag (m/s)	U (m/s)	V (m/s)	% Diff.
	50	149.415	192.541	15.284	0.748	15.146	
	100	149.415	192.541	13.688	0.784	13.481	-11.664
	150	149.415	192.541	13.993	0.663	13.798	2.178
	200	149.415	192.541	13.635	0.255	13.445	-2.624
	250	149.415	192.541	13.622	0.262	13.433	-0.090
	300	149.415	192.541	13.549	0.305	13.362	-0.542
avg.				13.962	0.503	13.778	-2.549
stdev				0.666	0.254	0.688	5.374

	Images	X (mm)	Y (mm)	Vel. Mag (m/s)	U (m/s)	V (m/s)	% Diff.
	50	152.064	180.178	13.456	0.185	13.315	
	100	152.064	180.178	13.264	0.276	13.116	-1.445
	150	152.064	180.178	13.841	0.368	13.687	4.168
	200	152.064	180.178	13.798	0.350	13.647	-0.308
	250	152.064	180.178	13.805	0.096	13.644	0.047
	300	152.064	180.178	13.904	0.141	13.748	0.713
avg.				13.678	0.236	13.526	0.635
stdev				0.257	0.112	0.252	2.124

	Images	X (mm)	Y (mm)	Vel. Mag (m/s)	U (m/s)	V (m/s)	% Diff.
	50	149.268	160.309	15.860	0.860	15.723	
	100	149.268	160.309	15.475	0.077	15.285	-2.486
	150	149.268	160.309	14.900	0.284	14.716	-3.860
	200	149.268	160.309	14.566	0.183	14.375	-2.297
	250	149.268	160.309	14.524	0.237	14.354	-0.286
	300	149.268	160.309	14.260	0.002	14.037	-1.853
avg.				14.931	0.274	14.748	-2.156
stdev				0.618	0.305	0.639	1.287

Field Average Velocity (m/s)	Deviation (m/s)
13.904	0.355

Table A 15 Repeatability of PIV images for q = 78.

Trial 1

Images	X	Y	Vel. Mag (m/s)	U (m/s)	V (m/s)
300	149.415	192.541	10.491	0.120	10.430
300	152.064	180.178	10.953	0.022	10.785
300	149.268	160.309	10.439	0.285	10.277
avg.			10.628		

Trial 2

Images	X	Y	Vel. Mag (m/s)	U (m/s)	V (m/s)
300	149.415	192.541	10.825	0.586	10.346
300	152.064	180.178	10.690	0.100	10.542
300	149.268	160.309	11.261	0.201	11.090
avg.			10.925		

Difference
2.723

Table A 16 Repeatability of PIV images for q = 44.

Trial1

Images	X	Y	Vel. Mag (m/s)	U (m/s)	V (m/s)
300	149.415	192.541	13.549	0.305	13.362
300	152.064	180.178	13.904	0.141	13.748
300	149.268	160.309	14.260	0.002	14.037
avg.			13.904		

Trial2

Images	X	Y	Vel. Mag (m/s)	U (m/s)	V (m/s)
300	149.415	192.541	13.500	0.595	13.056
300	152.064	180.178	13.260	0.699	12.984
300	149.268	160.309	13.817	0.694	13.461
avg.			13.526		

Difference
-2.724

Table A 17 Side velocity profile for q = 78, at Y/d = 2.

X (mm)	Y (mm)	X/d	Y/d	Vel. Mag. (m/s)	Defect
153.0946	195.0428	2	-1.771	9.849	0.929
153.0946	194.8823	2	-1.691	9.853	0.929
153.0946	194.7217	2	-1.611	9.848	0.929
153.0946	194.5611	2	-1.531	9.769	0.922
153.0946	194.4006	2	-1.450	9.690	0.914
153.0946	194.24	2	-1.370	9.610	0.907
153.0946	194.0795	2	-1.290	9.531	0.899
153.0946	193.9189	2	-1.209	9.451	0.892
153.0946	193.7584	2	-1.129	9.372	0.884
153.0946	193.5978	2	-1.049	9.342	0.881
153.0946	193.4372	2	-0.969	9.341	0.881
153.0946	193.2767	2	-0.888	9.341	0.881
153.0946	193.1161	2	-0.808	9.341	0.881
153.0946	192.9556	2	-0.728	9.341	0.881
153.0946	192.795	2	-0.647	9.341	0.881
153.0946	192.6344	2	-0.567	9.345	0.882
153.0946	192.4739	2	-0.487	9.371	0.884
153.0946	192.3133	2	-0.407	9.398	0.887
153.0946	192.1528	2	-0.326	9.424	0.889
153.0946	191.9922	2	-0.246	9.451	0.892
153.0946	191.8316	2	-0.166	9.454	0.892
153.0946	191.6711	2	-0.086	9.454	0.892
153.0946	191.5105	2	-0.005	9.454	0.892
153.0946	191.35	2	0.075	9.454	0.892
153.0946	191.1894	2	0.155	9.454	0.892
153.0946	191.0289	2	0.236	9.454	0.892
153.0946	190.8683	2	0.316	9.456	0.892
153.0946	190.7077	2	0.396	9.463	0.893
153.0946	190.5472	2	0.476	9.470	0.893
153.0946	190.3866	2	0.557	9.477	0.894
153.0946	190.2261	2	0.637	9.484	0.895
153.0946	190.0655	2	0.717	9.491	0.895
153.0946	189.9049	2	0.798	9.498	0.896
153.0946	189.7444	2	0.878	9.508	0.897
153.0946	189.5838	2	0.958	9.518	0.898
153.0946	189.4233	2	1.038	9.528	0.899
153.0946	189.2627	2	1.119	9.537	0.900
153.0946	189.1022	2	1.199	9.545	0.900
153.0946	188.9416	2	1.279	9.552	0.901
153.0946	188.781	2	1.359	9.559	0.902
153.0946	188.6205	2	1.440	9.566	0.902
153.0946	188.4599	2	1.520	9.573	0.903
153.0946	188.2994	2	1.600	9.580	0.904

153.0946	188.1388	2	1.681	9.603	0.906
153.0946	187.9782	2	1.761	9.701	0.915
153.0946	187.8177	2	1.841	9.799	0.924
153.0946	187.6571	2	1.921	9.897	0.934
153.0946	187.4966	2	2.002	9.994	0.943
153.0946	187.336	2	2.082	10.092	0.952
153.0946	187.1755	2	2.162	10.190	0.961
153.0946	187.0149	2	2.243	10.205	0.963
153.0946	186.8543	2	2.323	10.185	0.961
153.0946	186.6938	2	2.403	10.165	0.959
153.0946	186.5332	2	2.483	10.146	0.957
153.0946	186.3727	2	2.564	10.177	0.960
153.0946	186.2121	2	2.644	10.275	0.969
153.0946	186.0515	2	2.724	10.373	0.979
153.0946	185.891	2	2.805	10.470	0.988
153.0946	185.7304	2	2.885	10.568	0.997
153.0946	185.5699	2	2.965	10.666	1.006
153.0946	185.4093	2	3.045	10.764	1.015
153.0946	185.2488	2	3.126	10.777	1.017
153.0946	185.0882	2	3.206	10.787	1.018
153.0946	184.9276	2	3.286	10.798	1.019
153.0946	184.7671	2	3.366	10.808	1.020
153.0946	184.6065	2	3.447	10.818	1.021
153.0946	184.446	2	3.527	10.828	1.021
153.0946	184.2854	2	3.607	10.834	1.022
153.0946	184.1248	2	3.688	10.835	1.022
153.0946	183.9643	2	3.768	10.836	1.022
153.0946	183.8037	2	3.848	10.838	1.022
153.0946	183.6432	2	3.928	10.841	1.023
153.0946	183.4826	2	4.009	10.851	1.024
153.0946	183.3221	2	4.089	10.861	1.025
153.0946	183.1615	2	4.169	10.871	1.026
153.0946	183.0009	2	4.250	10.881	1.027
153.0946	182.8404	2	4.330	10.891	1.027
153.0946	182.6798	2	4.410	10.902	1.028
153.0946	182.5193	2	4.490	10.882	1.027
153.0946	182.3587	2	4.571	10.852	1.024
153.0946	182.1981	2	4.651	10.823	1.021
153.0946	182.0376	2	4.731	10.793	1.018
153.0946	181.877	2	4.811	10.763	1.015
153.0946	181.7165	2	4.892	10.733	1.013
153.0946	181.5559	2	4.972	10.713	1.011
153.0946	181.3954	2	5.052	10.722	1.012

Table A 18 Side velocity profile for q = 78, at Y/d = 4.

X (mm)	Y (mm)	X/d	Y/d	Vel. Mag. (m/s)	Defect
148.9736	195.0428	4	-1.771	10.694	1.009
148.9736	194.8882	4	-1.694	10.692	1.009
148.9736	194.7336	4	-1.617	10.689	1.008
148.9736	194.579	4	-1.539	10.686	1.008
148.9736	194.4244	4	-1.462	10.684	1.008
148.9736	194.2698	4	-1.385	10.681	1.008
148.9736	194.1151	4	-1.308	10.679	1.007
148.9736	193.9605	4	-1.230	10.677	1.007
148.9736	193.8059	4	-1.153	10.679	1.007
148.9736	193.6513	4	-1.076	10.681	1.008
148.9736	193.4967	4	-0.998	10.685	1.008
148.9736	193.3421	4	-0.921	10.678	1.007
148.9736	193.1875	4	-0.844	10.639	1.004
148.9736	193.0329	4	-0.766	10.600	1.000
148.9736	192.8783	4	-0.689	10.560	0.996
148.9736	192.7236	4	-0.612	10.521	0.993
148.9736	192.569	4	-0.535	10.482	0.989
148.9736	192.4144	4	-0.457	10.443	0.985
148.9736	192.2598	4	-0.380	10.403	0.981
148.9736	192.1052	4	-0.303	10.364	0.978
148.9736	191.9506	4	-0.225	10.325	0.974
148.9736	191.796	4	-0.148	10.286	0.970
148.9736	191.6414	4	-0.071	10.247	0.967
148.9736	191.4867	4	0.007	10.207	0.963
148.9736	191.3321	4	0.084	10.168	0.959
148.9736	191.1775	4	0.161	10.149	0.957
148.9736	191.0229	4	0.239	10.152	0.958
148.9736	190.8683	4	0.316	10.164	0.959
148.9736	190.7137	4	0.393	10.186	0.961
148.9736	190.5591	4	0.470	10.218	0.964
148.9736	190.4045	4	0.548	10.267	0.969
148.9736	190.2499	4	0.625	10.316	0.973
148.9736	190.0952	4	0.702	10.366	0.978
148.9736	189.9406	4	0.780	10.415	0.983
148.9736	189.786	4	0.857	10.464	0.987
148.9736	189.6314	4	0.934	10.514	0.992
148.9736	189.4768	4	1.012	10.563	0.997
148.9736	189.3222	4	1.089	10.612	1.001
148.9736	189.1676	4	1.166	10.662	1.006
148.9736	189.013	4	1.244	10.711	1.010
148.9736	188.8583	4	1.321	10.761	1.015
148.9736	188.7037	4	1.398	10.810	1.020
148.9736	188.5491	4	1.475	10.859	1.024
148.9736	188.3945	4	1.553	10.893	1.028

148.9736	188.2399	4	1.630	10.915	1.030
148.9736	188.0853	4	1.707	10.936	1.032
148.9736	187.9307	4	1.785	10.958	1.034
148.9736	187.7761	4	1.862	10.969	1.035
148.9736	187.6215	4	1.939	10.967	1.035
148.9736	187.4668	4	2.017	10.966	1.035
148.9736	187.3122	4	2.094	10.965	1.034
148.9736	187.1576	4	2.171	10.964	1.034
148.9736	187.003	4	2.248	10.962	1.034
148.9736	186.8484	4	2.326	10.961	1.034
148.9736	186.6938	4	2.403	10.960	1.034
148.9736	186.5392	4	2.480	10.959	1.034
148.9736	186.3846	4	2.558	10.957	1.034
148.9736	186.2299	4	2.635	10.956	1.034
148.9736	186.0753	4	2.712	10.955	1.033
148.9736	185.9207	4	2.790	10.954	1.033
148.9736	185.7661	4	2.867	10.952	1.033
148.9736	185.6115	4	2.944	10.967	1.035
148.9736	185.4569	4	3.022	10.989	1.037
148.9736	185.3023	4	3.099	10.984	1.036
148.9736	185.1477	4	3.176	10.966	1.035
148.9736	184.9931	4	3.253	10.964	1.034
148.9736	184.8384	4	3.331	10.972	1.035
148.9736	184.6838	4	3.408	10.980	1.036
148.9736	184.5292	4	3.485	10.988	1.037
148.9736	184.3746	4	3.563	10.995	1.037
148.9736	184.22	4	3.640	11.003	1.038
148.9736	184.0654	4	3.717	11.011	1.039
148.9736	183.9108	4	3.795	11.019	1.040
148.9736	183.7562	4	3.872	11.027	1.040
148.9736	183.6015	4	3.949	11.035	1.041
148.9736	183.4469	4	4.027	11.043	1.042
148.9736	183.2923	4	4.104	11.050	1.042
148.9736	183.1377	4	4.181	11.058	1.043
148.9736	182.9831	4	4.258	11.066	1.044
148.9736	182.8285	4	4.336	11.053	1.043
148.9736	182.6739	4	4.413	11.035	1.041
148.9736	182.5193	4	4.490	11.030	1.041
148.9736	182.3647	4	4.568	11.028	1.040
148.9736	182.21	4	4.645	11.038	1.041
148.9736	182.0554	4	4.722	11.052	1.043
148.9736	181.9008	4	4.800	11.066	1.044
148.9736	181.7462	4	4.877	11.080	1.045
148.9736	181.5916	4	4.954	11.093	1.047
148.9736	181.437	4	5.032	11.107	1.048

Table A 19 Side velocity profile for q = 44, at Y/d = 2.

X (mm)	Y (mm)	X/d	Y/d	Vel. Mag. (m/s)	Defect
152.9626	195.0053	2	-1.748	13.121	0.944
152.9626	194.8506	2	-1.670	13.088	0.942
152.9626	194.6959	2	-1.593	13.047	0.939
152.9626	194.5412	2	-1.516	12.981	0.934
152.9626	194.3866	2	-1.438	12.916	0.929
152.9626	194.2319	2	-1.361	12.851	0.925
152.9626	194.0772	2	-1.284	12.786	0.920
152.9626	193.9225	2	-1.206	12.721	0.915
152.9626	193.7678	2	-1.129	12.655	0.910
152.9626	193.6132	2	-1.052	12.590	0.906
152.9626	193.4585	2	-0.974	12.460	0.896
152.9626	193.3038	2	-0.897	12.302	0.885
152.9626	193.1491	2	-0.820	12.145	0.874
152.9626	192.9945	2	-0.742	12.070	0.868
152.9626	192.8398	2	-0.665	12.005	0.864
152.9626	192.6851	2	-0.588	11.940	0.859
152.9626	192.5304	2	-0.510	11.875	0.854
152.9626	192.3757	2	-0.433	11.810	0.850
152.9626	192.2211	2	-0.356	11.744	0.845
152.9626	192.0664	2	-0.278	11.679	0.840
152.9626	191.9117	2	-0.201	11.651	0.838
152.9626	191.757	2	-0.124	11.686	0.841
152.9626	191.6023	2	-0.046	11.721	0.843
152.9626	191.4477	2	0.031	11.756	0.846
152.9626	191.293	2	0.109	11.791	0.848
152.9626	191.1383	2	0.186	11.826	0.851
152.9626	190.9836	2	0.263	11.861	0.853
152.9626	190.8289	2	0.341	11.895	0.856
152.9626	190.6743	2	0.418	11.934	0.859
152.9626	190.5196	2	0.495	11.974	0.861
152.9626	190.3649	2	0.573	12.013	0.864
152.9626	190.2102	2	0.650	12.048	0.867
152.9626	190.0555	2	0.727	12.083	0.869
152.9626	189.9009	2	0.805	12.118	0.872
152.9626	189.7462	2	0.882	12.153	0.874
152.9626	189.5915	2	0.959	12.188	0.877
152.9626	189.4368	2	1.037	12.223	0.879
152.9626	189.2821	2	1.114	12.257	0.882
152.9626	189.1275	2	1.191	12.315	0.886
152.9626	188.9728	2	1.269	12.397	0.892
152.9626	188.8181	2	1.346	12.479	0.898

152.9626	188.6634	2	1.423	12.560	0.904
152.9626	188.5088	2	1.501	12.642	0.909
152.9626	188.3541	2	1.578	12.723	0.915
152.9626	188.1994	2	1.655	12.805	0.921
152.9626	188.0447	2	1.733	12.886	0.927
152.9626	187.89	2	1.810	12.995	0.935
152.9626	187.7354	2	1.887	13.105	0.943
152.9626	187.5807	2	1.965	13.211	0.950
152.9626	187.426	2	2.042	13.293	0.956
152.9626	187.2713	2	2.119	13.374	0.962
152.9626	187.1166	2	2.197	13.456	0.968
152.9626	186.962	2	2.274	13.537	0.974
152.9626	186.8073	2	2.351	13.619	0.980
152.9626	186.6526	2	2.429	13.700	0.986
152.9626	186.4979	2	2.506	13.782	0.991
152.9626	186.3432	2	2.583	13.831	0.995
152.9626	186.1886	2	2.661	13.860	0.997
152.9626	186.0339	2	2.738	13.890	0.999
152.9626	185.8792	2	2.815	13.920	1.001
152.9626	185.7245	2	2.893	13.949	1.004
152.9626	185.5698	2	2.970	13.979	1.006
152.9626	185.4152	2	3.047	14.008	1.008
152.9626	185.2605	2	3.125	14.040	1.010
152.9626	185.1058	2	3.202	14.095	1.014
152.9626	184.9511	2	3.279	14.149	1.018
152.9626	184.7964	2	3.357	14.197	1.021
152.9626	184.6418	2	3.434	14.227	1.023
152.9626	184.4871	2	3.511	14.256	1.026
152.9626	184.3324	2	3.589	14.286	1.028
152.9626	184.1777	2	3.666	14.315	1.030
152.9626	184.0231	2	3.743	14.345	1.032
152.9626	183.8684	2	3.821	14.374	1.034
152.9626	183.7137	2	3.898	14.404	1.036
152.9626	183.559	2	3.975	14.377	1.034
152.9626	183.4043	2	4.053	14.330	1.031
152.9626	183.2497	2	4.130	14.284	1.028
152.9626	183.095	2	4.208	14.238	1.024
152.9626	182.9403	2	4.285	14.191	1.021
152.9626	182.7856	2	4.362	14.145	1.018
152.9626	182.6309	2	4.440	14.098	1.014
152.9626	182.4763	2	4.517	14.052	1.011
152.9626	182.3216	2	4.594	14.004	1.007
152.9626	182.1669	2	4.672	13.956	1.004
152.9626	182.0122	2	4.749	13.909	1.001
152.9626	181.8575	2	4.826	13.863	0.997
152.9626	181.7029	2	4.904	13.816	0.994
152.9626	181.5482	2	4.981	13.770	0.991
152.9626	181.3935	2	5.058	13.723	0.987

Table A 20 Side velocity profile for q = 44, at Y/d = 4.

X (mm)	Y (mm)	X/d	Y/d	Vel. Mag. (m/s)	Defect
149.0289	195.0053	4	-1.748	13.344	0.960
149.0289	194.8421	4	-1.666	13.298	0.957
149.0289	194.6789	4	-1.584	13.276	0.955
149.0289	194.5157	4	-1.503	13.304	0.957
149.0289	194.3525	4	-1.421	13.331	0.959
149.0289	194.1893	4	-1.340	13.358	0.961
149.0289	194.0261	4	-1.258	13.385	0.963
149.0289	193.8629	4	-1.176	13.412	0.965
149.0289	193.6997	4	-1.095	13.438	0.967
149.0289	193.5365	4	-1.013	13.465	0.969
149.0289	193.3733	4	-0.932	13.492	0.971
149.0289	193.2102	4	-0.850	13.518	0.973
149.0289	193.047	4	-0.768	13.545	0.974
149.0289	192.8838	4	-0.687	13.572	0.976
149.0289	192.7206	4	-0.605	13.598	0.978
149.0289	192.5574	4	-0.524	13.625	0.980
149.0289	192.3942	4	-0.442	13.652	0.982
149.0289	192.231	4	-0.360	13.679	0.984
149.0289	192.0678	4	-0.279	13.707	0.986
149.0289	191.9046	4	-0.197	13.741	0.989
149.0289	191.7414	4	-0.116	13.784	0.992
149.0289	191.5782	4	-0.034	13.827	0.995
149.0289	191.415	4	0.047	13.879	0.998
149.0289	191.2518	4	0.129	13.933	1.002
149.0289	191.0886	4	0.211	13.988	1.006
149.0289	190.9254	4	0.292	14.042	1.010
149.0289	190.7622	4	0.374	14.097	1.014
149.0289	190.5991	4	0.455	14.151	1.018
149.0289	190.4359	4	0.537	14.205	1.022
149.0289	190.2727	4	0.619	14.260	1.026
149.0289	190.1095	4	0.700	14.314	1.030
149.0289	189.9463	4	0.782	14.369	1.034
149.0289	189.7831	4	0.863	14.423	1.038
149.0289	189.6199	4	0.945	14.476	1.041
149.0289	189.4567	4	1.027	14.520	1.045
149.0289	189.2935	4	1.108	14.563	1.048
149.0289	189.1303	4	1.190	14.599	1.050
149.0289	188.9671	4	1.271	14.628	1.052
149.0289	188.8039	4	1.353	14.657	1.054
149.0289	188.6407	4	1.435	14.664	1.055
149.0289	188.4775	4	1.516	14.666	1.055
149.0289	188.3143	4	1.598	14.668	1.055
149.0289	188.1511	4	1.679	14.670	1.055
149.0289	187.988	4	1.761	14.671	1.055

149.0289	187.8248	4	1.843	14.673	1.056
149.0289	187.6616	4	1.924	14.675	1.056
149.0289	187.4984	4	2.006	14.677	1.056
149.0289	187.3352	4	2.087	14.679	1.056
149.0289	187.172	4	2.169	14.681	1.056
149.0289	187.0088	4	2.251	14.682	1.056
149.0289	186.8456	4	2.332	14.688	1.057
149.0289	186.6824	4	2.414	14.717	1.059
149.0289	186.5192	4	2.495	14.746	1.061
149.0289	186.356	4	2.577	14.758	1.062
149.0289	186.1928	4	2.659	14.753	1.061
149.0289	186.0296	4	2.740	14.749	1.061
149.0289	185.8664	4	2.822	14.736	1.060
149.0289	185.7032	4	2.903	14.722	1.059
149.0289	185.54	4	2.985	14.708	1.058
149.0289	185.3769	4	3.067	14.695	1.057
149.0289	185.2137	4	3.148	14.681	1.056
149.0289	185.0505	4	3.230	14.667	1.055
149.0289	184.8873	4	3.311	14.653	1.054
149.0289	184.7241	4	3.393	14.639	1.053
149.0289	184.5609	4	3.475	14.626	1.052
149.0289	184.3977	4	3.556	14.612	1.051
149.0289	184.2345	4	3.638	14.598	1.050
149.0289	184.0713	4	3.719	14.586	1.049
149.0289	183.9081	4	3.801	14.582	1.049
149.0289	183.7449	4	3.883	14.577	1.049
149.0289	183.5817	4	3.964	14.559	1.047
149.0289	183.4185	4	4.046	14.531	1.045
149.0289	183.2553	4	4.127	14.503	1.043
149.0289	183.0921	4	4.209	14.493	1.043
149.0289	182.9289	4	4.291	14.485	1.042
149.0289	182.7657	4	4.372	14.476	1.041
149.0289	182.6026	4	4.454	14.467	1.041
149.0289	182.4394	4	4.535	14.459	1.040
149.0289	182.2762	4	4.617	14.450	1.040
149.0289	182.113	4	4.699	14.442	1.039
149.0289	181.9498	4	4.780	14.433	1.038
149.0289	181.7866	4	4.862	14.424	1.038
149.0289	181.6234	4	4.943	14.416	1.037
149.0289	181.4602	4	5.025	14.407	1.036

Table A 21 Proximal velocity profile for q = 78.

X (mm)	Y (mm)	X/d	Vel. Mag. (m/s)	Defect
153.0946	191.5105	1.953	9.454	0.892
153.0113	191.5105	1.994	9.575	0.903
152.9281	191.5105	2.036	9.697	0.915
152.8448	191.5105	2.078	9.818	0.926
152.7616	191.5105	2.119	9.939	0.938
152.6783	191.5105	2.161	10.061	0.949
152.5951	191.5105	2.202	10.176	0.960
152.5118	191.5105	2.244	10.283	0.970
152.4285	191.5105	2.286	10.391	0.980
152.3453	191.5105	2.327	10.498	0.990
152.262	191.5105	2.369	10.606	1.001
152.1788	191.5105	2.411	10.713	1.011
152.0955	191.5105	2.452	10.820	1.021
152.0123	191.5105	2.494	10.869	1.025
151.929	191.5105	2.535	10.859	1.024
151.8458	191.5105	2.577	10.849	1.024
151.7625	191.5105	2.619	10.840	1.023
151.6793	191.5105	2.660	10.830	1.022
151.596	191.5105	2.702	10.820	1.021
151.5128	191.5105	2.744	10.811	1.020
151.4295	191.5105	2.785	10.791	1.018
151.3463	191.5105	2.827	10.764	1.015
151.263	191.5105	2.868	10.737	1.013
151.1798	191.5105	2.910	10.710	1.010
151.0965	191.5105	2.952	10.683	1.008
151.0133	191.5105	2.993	10.655	1.005
150.93	191.5105	3.035	10.628	1.003
150.8468	191.5105	3.077	10.601	1.000
150.7635	191.5105	3.118	10.574	0.998
150.6802	191.5105	3.160	10.547	0.995
150.597	191.5105	3.202	10.520	0.992
150.5137	191.5105	3.243	10.493	0.990
150.4305	191.5105	3.285	10.465	0.987
150.3472	191.5105	3.326	10.438	0.985
150.264	191.5105	3.368	10.411	0.982
150.1807	191.5105	3.410	10.384	0.980
150.0975	191.5105	3.451	10.357	0.977
150.0142	191.5105	3.493	10.330	0.975
149.931	191.5105	3.535	10.303	0.972
149.8477	191.5105	3.576	10.280	0.970
149.7645	191.5105	3.618	10.270	0.969
149.6812	191.5105	3.659	10.260	0.968
149.598	191.5105	3.701	10.251	0.967
149.5147	191.5105	3.743	10.241	0.966
149.4315	191.5105	3.784	10.231	0.965

149.3482	191.5105	3.826	10.222	0.964
149.265	191.5105	3.868	10.215	0.964
149.1817	191.5105	3.909	10.214	0.964
149.0985	191.5105	3.951	10.214	0.964
149.0152	191.5105	3.992	10.214	0.964
148.9319	191.5105	4.034	10.213	0.964
148.8487	191.5105	4.076	10.213	0.963
148.7654	191.5105	4.117	10.213	0.963
148.6822	191.5105	4.159	10.220	0.964
148.5989	191.5105	4.201	10.243	0.966
148.5157	191.5105	4.242	10.266	0.968
148.4324	191.5105	4.284	10.289	0.971
148.3492	191.5105	4.325	10.312	0.973
148.2659	191.5105	4.367	10.334	0.975
148.1827	191.5105	4.409	10.357	0.977
148.0994	191.5105	4.450	10.380	0.979
148.0162	191.5105	4.492	10.403	0.981
147.9329	191.5105	4.534	10.426	0.984
147.8497	191.5105	4.575	10.448	0.986
147.7664	191.5105	4.617	10.471	0.988
147.6832	191.5105	4.658	10.494	0.990
147.5999	191.5105	4.700	10.517	0.992
147.5167	191.5105	4.742	10.540	0.994
147.4334	191.5105	4.783	10.563	0.996
147.3501	191.5105	4.825	10.585	0.999
147.2669	191.5105	4.867	10.608	1.001
147.1836	191.5105	4.908	10.631	1.003
147.1004	191.5105	4.950	10.653	1.005
147.0171	191.5105	4.991	10.653	1.005
146.9339	191.5105	5.033	10.652	1.005
146.8506	191.5105	5.075	10.652	1.005
146.7674	191.5105	5.116	10.652	1.005
146.6841	191.5105	5.158	10.651	1.005
146.6009	191.5105	5.200	10.651	1.005
146.5176	191.5105	5.241	10.650	1.005
146.4344	191.5105	5.283	10.649	1.005
146.3511	191.5105	5.324	10.647	1.004
146.2679	191.5105	5.366	10.645	1.004
146.1846	191.5105	5.408	10.644	1.004
146.1014	191.5105	5.449	10.642	1.004
146.0181	191.5105	5.491	10.640	1.004
145.9349	191.5105	5.533	10.636	1.003
145.8516	191.5105	5.574	10.618	1.002
145.7684	191.5105	5.616	10.599	1.000
145.6851	191.5105	5.657	10.580	0.998
145.6018	191.5105	5.699	10.561	0.996
145.5186	191.5105	5.741	10.542	0.995
145.4353	191.5105	5.782	10.524	0.993
145.3521	191.5105	5.824	10.505	0.991

145.2688	191.5105	5.866	10.486	0.989
145.1856	191.5105	5.907	10.467	0.987
145.1023	191.5105	5.949	10.449	0.986
145.0191	191.5105	5.990	10.430	0.984
144.9358	191.5105	6.032	10.411	0.982
144.8526	191.5105	6.074	10.392	0.980

Table A 22 Proximal velocity profile for q = 44.

X	Y	X/d	Vel. Mag. (m/s)	Defect
153.103	191.4931	1.948	11.604	0.829
153.0193	191.4931	1.990	11.688	0.835
152.9356	191.4931	2.032	11.773	0.841
152.8519	191.4931	2.074	11.857	0.847
152.7681	191.4931	2.116	11.942	0.853
152.6844	191.4931	2.158	12.027	0.859
152.6007	191.4931	2.200	12.111	0.865
152.517	191.4931	2.242	12.196	0.871
152.4332	191.4931	2.283	12.280	0.877
152.3495	191.4931	2.325	12.365	0.883
152.2658	191.4931	2.367	12.450	0.889
152.1821	191.4931	2.409	12.534	0.895
152.0983	191.4931	2.451	12.619	0.901
152.0146	191.4931	2.493	12.703	0.907
151.9309	191.4931	2.535	12.788	0.913
151.8472	191.4931	2.576	12.873	0.919
151.7634	191.4931	2.618	12.955	0.925
151.6797	191.4931	2.660	13.037	0.931
151.596	191.4931	2.702	13.119	0.937
151.5123	191.4931	2.744	13.201	0.943
151.4285	191.4931	2.786	13.283	0.949
151.3448	191.4931	2.828	13.352	0.954
151.2611	191.4931	2.869	13.375	0.955
151.1774	191.4931	2.911	13.398	0.957
151.0936	191.4931	2.953	13.420	0.959
151.0099	191.4931	2.995	13.443	0.960
150.9262	191.4931	3.037	13.465	0.962
150.8425	191.4931	3.079	13.485	0.963
150.7587	191.4931	3.121	13.502	0.964
150.675	191.4931	3.162	13.519	0.966
150.5913	191.4931	3.204	13.535	0.967
150.5076	191.4931	3.246	13.552	0.968
150.4238	191.4931	3.288	13.569	0.969
150.3401	191.4931	3.330	13.586	0.970
150.2564	191.4931	3.372	13.603	0.972

150.1727	191.4931	3.414	13.620	0.973
150.0889	191.4931	3.456	13.636	0.974
150.0052	191.4931	3.497	13.653	0.975
149.9215	191.4931	3.539	13.670	0.976
149.8377	191.4931	3.581	13.687	0.978
149.754	191.4931	3.623	13.704	0.979
149.6703	191.4931	3.665	13.721	0.980
149.5866	191.4931	3.707	13.738	0.981
149.5028	191.4931	3.749	13.754	0.982
149.4191	191.4931	3.790	13.771	0.984
149.3354	191.4931	3.832	13.788	0.985
149.2517	191.4931	3.874	13.805	0.986
149.1679	191.4931	3.916	13.822	0.987
149.0842	191.4931	3.958	13.839	0.988
149.0005	191.4931	4.000	13.861	0.990
148.9168	191.4931	4.042	13.883	0.992
148.833	191.4931	4.083	13.906	0.993
148.7493	191.4931	4.125	13.928	0.995
148.6656	191.4931	4.167	13.951	0.996
148.5819	191.4931	4.209	13.967	0.998
148.4981	191.4931	4.251	13.960	0.997
148.4144	191.4931	4.293	13.952	0.997
148.3307	191.4931	4.335	13.944	0.996
148.247	191.4931	4.377	13.936	0.995
148.1632	191.4931	4.418	13.928	0.995
148.0795	191.4931	4.460	13.937	0.996
147.9958	191.4931	4.502	13.962	0.997
147.9121	191.4931	4.544	13.987	0.999
147.8283	191.4931	4.586	14.011	1.001
147.7446	191.4931	4.628	14.036	1.003
147.6609	191.4931	4.670	14.061	1.004
147.5772	191.4931	4.711	14.085	1.006
147.4934	191.4931	4.753	14.110	1.008
147.4097	191.4931	4.795	14.135	1.010
147.326	191.4931	4.837	14.160	1.011
147.2423	191.4931	4.879	14.184	1.013
147.1585	191.4931	4.921	14.209	1.015
147.0748	191.4931	4.963	14.234	1.017
146.9911	191.4931	5.004	14.258	1.018
146.9074	191.4931	5.046	14.283	1.020
146.8236	191.4931	5.088	14.308	1.022
146.7399	191.4931	5.130	14.333	1.024
146.6562	191.4931	5.172	14.357	1.026
146.5725	191.4931	5.214	14.382	1.027
146.4887	191.4931	5.256	14.407	1.029

146.405	191.4931	5.297	14.432	1.031
146.3213	191.4931	5.339	14.456	1.033
146.2376	191.4931	5.381	14.453	1.032
146.1538	191.4931	5.423	14.445	1.032
146.0701	191.4931	5.465	14.437	1.031
145.9864	191.4931	5.507	14.429	1.031
145.9026	191.4931	5.549	14.421	1.030
145.8189	191.4931	5.591	14.418	1.030
145.7352	191.4931	5.632	14.433	1.031
145.6515	191.4931	5.674	14.449	1.032
145.5677	191.4931	5.716	14.465	1.033
145.484	191.4931	5.758	14.481	1.034
145.4003	191.4931	5.800	14.496	1.035
145.3166	191.4931	5.842	14.512	1.037
145.2328	191.4931	5.884	14.526	1.038
145.1491	191.4931	5.925	14.541	1.039
145.0654	191.4931	5.967	14.556	1.040
144.9817	191.4931	6.009	14.571	1.041
144.8979	191.4931	6.051	14.586	1.042
144.8142	191.4931	6.093	14.600	1.043

Table A 23 Spray characteristic break up matrix

For small Oh	172≥q≥70	70>q≥40	40>q≥20	20>q≥15	15>q≥10
30≥We≥25	- Nondimensional disturbance wavelength 0.8≤λ/d <0.74* -Downstream break up occurs at X/d=8* -Combined surface/column break up with multimode break up characteristics ** -Nondimensional break up height 33≤Z/d ≤53**	- Nondimensional disturbance wavelength 0.8≤λ/d <0.74* -Downstream break up occurs at X/d=8* -Column break up with multimode break up characteristics ** -Nondimensional break up height 24.3≤Z/d <33** -Droplet sizes ranging from 40-125µm 300 diameters downstream***	- Nondimensional disturbance wavelength 0.8≤λ/d <0.74* -Downstream break up occurs at X/d=8* -Column break up with multimode break up characteristics ** -Nondimensional break up height 16.8≤Z/d <24.3**	- Nondimensional disturbance wavelength 0.8≤λ/d <0.74* -Downstream break up occurs at X/d=8* -Column break up with multimode break up characteristics ** -Nondimensional break up height 14.5≤Z/d <16.8**	-Significant drag on the jet with bending -Multimode break up mechanism -High shear along sides of the jet with droplet stripping -Significant droplet deposition along wall lining - Nondimensional disturbance wavelength 0.8≤λ/d <0.74* -Downstream break up occurs at X/d=8* -Nondimensional break up height 11.7≤Z/d <14.5**
25>We≥14	- Nondimensional disturbance wavelength 1≤λ/d <0.8* -Downstream break up occurs at X/d=8* -Column break up regime with bag break up mechanism** -Nondimensional break up height 33≤Z/d ≤53**	- Nondimensional disturbance wavelength 1≤λ/d <0.8* -Downstream break up occurs at X/d=8* -Column break up regime with bag break up mechanism** -Nondimensional break up height 24.3≤Z/d <33**	- Nondimensional disturbance wavelength 1≤λ/d <0.8* -Downstream break up occurs at X/d=8* -Column break up regime with bag break up mechanism** -Nondimensional break up height 16.8≤Z/d <24.3**	-Significant drag on the jet with bending -Mostly bag break up with some multimode break up -High shear along sides of the jet with droplet stripping -Increased droplet deposition on wall lining - Nondimensional disturbance wavelength 1≤λ/d <0.8* -Downstream break up occurs at X/d=8* -Nondimensional break up height 14.5≤Z/d <16.8**	- Nondimensional disturbance wavelength 1≤λ/d <0.8* -Downstream break up occurs at X/d=8* -Significant drag on the jet with bending -Column break up regime with bag break up mechanism** -Nondimensional break up height 11.7≤Z/d <14.5** -Increasing surface break up

14>We≥7	-Nondimensional disturbance wavelength 1.4≤λ/d <1* -Downstream break up occurs at X/d=8* -Enhanced capillary break up regime, with some bag break up near We=14** -Nondimensional break up height 33≤Z/d ≤53**	-Nondimensional disturbance wavelength 1.4≤λ/d <1* -Downstream break up occurs at X/d=8* -Enhanced capillary break up regime, with some bag break up near We=14** -Nondimensional break up height 24.3≤Z/d <33**	-Increased drag on jet results in significant bending -Column break up with bag break up mechanism and large ligaments -Nondimensional disturbance wavelength 1.4≤λ/d <1* -Downstream break up occurs at X/d=8* -Nondimensional break up height 16.8≤Z/d <24.3**	-Nondimensional disturbance wavelength 1.4≤λ/d <1* -Downstream break up occurs at X/d=8* -Enhanced capillary break up regime, with some bag break up near We=14** -Nondimensional break up height 14.5≤Z/d <16.8**	-Nondimensional disturbance wavelength 1.4≤λ/d <1* -Downstream break up occurs at X/d=8* -Enhanced capillary break up regime, with some bag break up near We=14** -Nondimensional break up height 11.7≤Z/d <14.5**
7>We≥4	-Nondimensional disturbance wavelength 1.4<λ/d ≤1.8* -Downstream break up occurs at X/d=8* -Enhanced capillary break up regime** -Nondimensional break up height 33≤Z/d ≤53**	-Slight bending of the jet with penetration Z/d<250 -Column break up mechanism -Nondimensional disturbance wavelength 1.4<λ/d ≤1.8* -Significant velocity defect along the side of the jet -Downstream break up occurs at X/d=8*	-Nondimensional disturbance wavelength 1.4<λ/d ≤1.8* -Downstream break up occurs at X/d=8* -Enhanced capillary break up regime**	-Nondimensional disturbance wavelength 1.4<λ/d ≤1.8* -Downstream break up occurs at X/d=8* -Enhanced capillary break up regime**	-Nondimensional disturbance wavelength 1.4<λ/d ≤1.8* -Downstream break up occurs at X/d=8* -Enhanced capillary break up regime**
4>We≥1	-Very little jet bending with penetration Z/d>250 -column break up mechanism with very large wavelength disturbances -No apparent thinning of the liquid column before break up* -Enhanced capillary break up regime** -Nondimensional break up height 33≤Z/d ≤53**				

Table A 24 Wavelength and break up locations for q=10.

	We	q	λ (in)	Xb (in)	Zb (in)	λ/d	Xb/d	Zb/d
	29.29	10		1.082	1.388		6.9	8.82
	29.29	10	0.145			0.92		
	29.29	10	0.228	1.198	1.625	1.4	7.6	10.3
	29.29	10	0.13	1.211	1.726	0.825	7.7	11
	29.29	10	0.165	1.25	1.837	1.04	7.9	11.66
	29.29	10	0.135	1.398	1.742	0.86	8.8	11.06
	29.29	10	0.139	1.36	1.767	0.883	8.6	11.22
	29.29	10	0.13	1.219	1.706	0.82	7.74	10.83
	29.29	10	0.14	1.322	1.7	0.889	8.39	10.8
	29.29	10	0.157	1.201	1.638	0.99	7.6	10.4
	29.29	10	0.153	1.257	1.72	0.97	7.98	10.92
	29.29	10	0.136	1.215	1.75	0.86	7.72	11.11
avg.						0.950636	7.90273	10.7382
stdev						0.164448	0.53145	0.73643
					Precision	0.089844	0.29035	0.40234
					Uncert.	0.090737	0.29063	0.40254

Table A 25 Wavelength and break up locations for q=18.8.

	We	q	λ (in)	Xb (in)	Zb (in)	λ/d	Xb/d	Zb/d
	15.85	18.8	0.194	1.2	2.218	1.23	7.62	14.08
	15.85	18.8		1.35	2.242		8.5	14.23
	15.85	18.8	0.219	1.24	2.245	1.4	7.9	14.3
	15.85	18.8	0.163	1.245	2.266	1.04	7.9	14.4
	15.85	18.8	0.18	1.259	2.294	1.14	8	14.57
	15.85	18.8	0.169	1.255	2.263	1.07	7.97	14.37
	15.85	18.8	0.168	1.3	2.244	1.07	8.25	14.25
	15.85	18.8	0.229	1.214	2.24	1.45	7.71	14.22
	15.85	18.8	0.2	1.248	2.186	1.27	7.92	13.88
	15.85	18.8	0.168	1.245	2.309	1.07	7.91	14.66
	15.85	18.8		1.251	2.304		7.94	14.63
	15.85	18.8	0.159	1.265	2.308	1	8.03	14.65
	15.85	18.8	0.168	1.1	2.3	1.07	7	14.6
	15.85	18.8	0.232	1.278	2.269	1.47	8.11	14.4
avg.						1.19	7.91143	14.3743
stdev						0.169706	0.33777	0.23372
					Precision	0.087986	0.15987	0.11063
					Uncert.	0.088898	0.16038	0.11135

Table A 26 Wavelength and break up locations for q=40.

	We	q	λ (in)	Xb (in)	Zb (in)	λ/d	Xb/d	Zb/d
	7.32	40	0.3	1.286	4.2	1.9	8.16	26.7
	7.32	40		1.227	3.57		7.8	22.7
	7.32	40		1.29	4.2		8.19	26.6
	7.32	40	0.251	1.287	4.244	1.6	8.17	26.9
	7.32	40	0.258			1.6		
	7.32	40	0.304	1.184	3.58	1.9	7.52	22.73
	7.32	40	0.2574	1.316	3.89	1.74	8.4	24.7
	7.32	40	0.247	1.257	3.975	1.57	7.98	25.24
	7.32	40		1.278	4.16		8.1	26.4
	7.32	40	0.31	1.296	3.83	1.96	8.22	24.3
	7.32	40		1.284	3.892		8.15	24.7
	7.32	40	0.28	1.17	3.92	1.78	7.43	24.89
	7.32	40		1.348	3.765		8.5	23.9
	7.32	40		1.31	3.785		8.3	24.03
	7.32	40	0.244	1.281	4.157	1.54	8.13	26.3
	7.32	40	0.216			1.37		
	7.32	40	0.242			1.54		
	7.32	40	0.219			1.39		
	7.32	40	0.223	1.213	3.879	1.42	7.7	24.6
	7.32	40	0.214	1.149	3.916	1.36	7.3	24.87
	7.32	40	0.204	1.268	3.897	1.3	8.05	24.7
	7.32	40		1.114	3.859		7.07	24.5
avg.						1.598	7.95389	24.9311
stdev						0.214915	0.39803	1.24794
					Precision	0.097719	0.16324	0.51181
					Uncert.	0.098541	0.16373	0.51196

APPENDIX B

Figure B1 Calibration plot of Actual Flow Rate vs. Indicated Flow Rate.....155

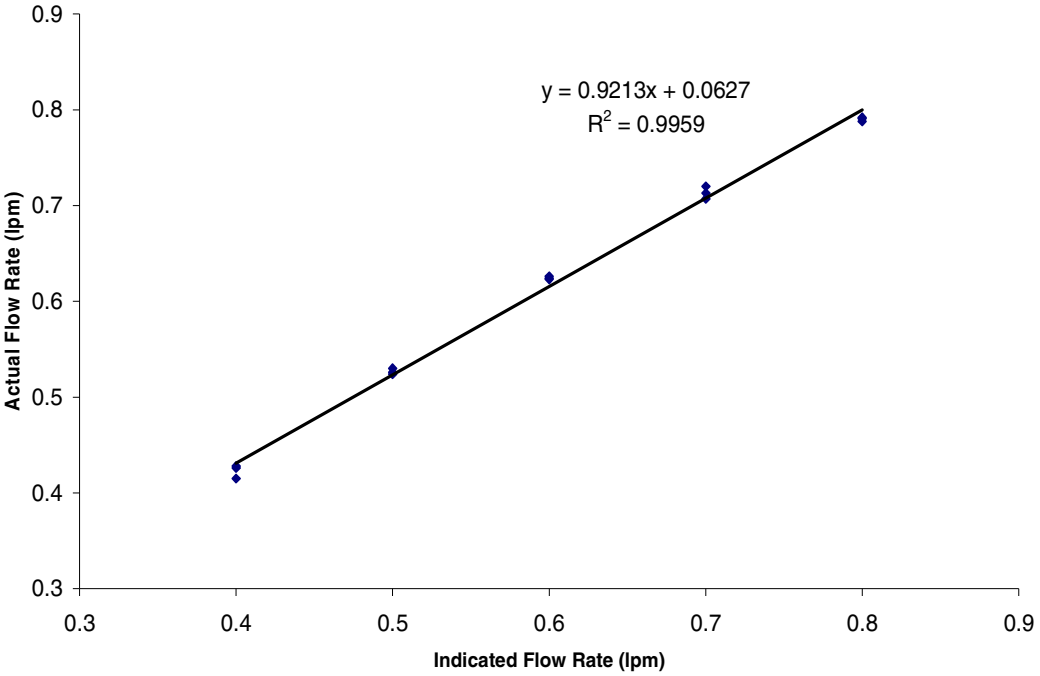


Figure B1 Calibration plot of Actual Flow Rate vs. Indicated Flow Rate

NOMENCLATURE

d = Diameter of water jet

d_p = Diameter of seed particle

d_t = Diameter of test section

f = Frequency of instability wave

F = Total body forces

Oh = Liquid Ohnesorge number $[\mu_j/(\rho_j d_j \sigma)^{0.5}]$

P = Fluid pressure

q = Ratio of cross flow momentum to jet momentum

Re_∞ = Reynolds number for the cross flow $(U_\infty d_t/\upsilon_\infty)$

Re_j = Reynolds number for the water jet $(U_j d/\upsilon_j)$

Re_{cyl} = Reynolds number for a solid cylinder of jet diameter $(U_\infty d/\upsilon_\infty)$

Str = Strouhal Number

St = Stokes Number

U_∞ = Mean Velocity of cross flow

U_j = Injectant Velocity

We = Weber Number

X = Streamwise coordinate

Y = Spanwise coordinate

Z = Vertical coordinate from wall

α = Volulme fraction of fluid

ε = Density Ratio of Continuum to Seeding Particle

λ_s = Wavelength of instability

ν_∞ = Kinematic Viscosity of air

ν_j = Kinematic Viscosity of water

ω = Rotational Frequency of Vortex

ρ_∞ = Cross flow air density

ρ_j = Density of Water from Injector

σ = Surface Tension of Water